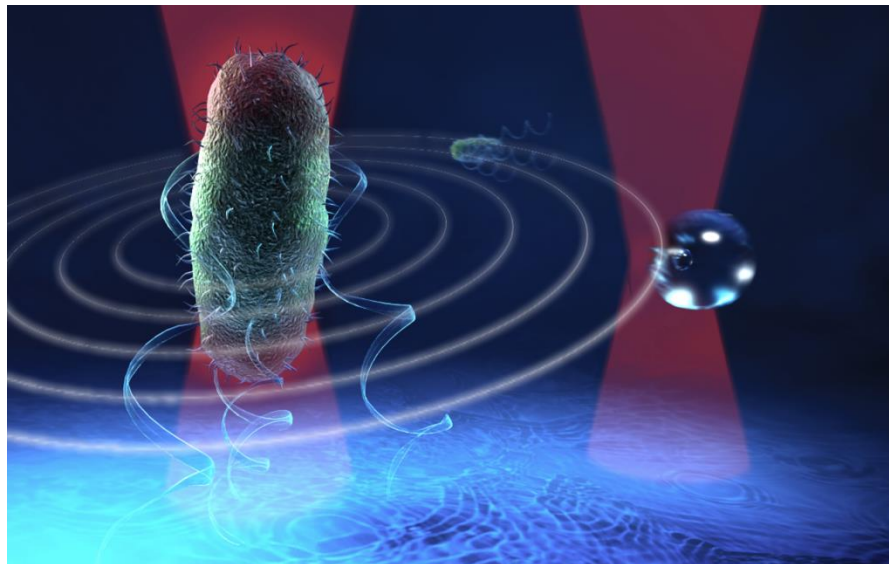


# Focused Optical Beams for Driving and Sensing Helical and Biological Microobjects

---

Silke R. Kirchner



München, 2014



# Focused Optical Beams for Driving and Sensing Helical and Biological Microobjects

---

Silke R. Kirchner



Dissertation  
an der Fakultät für Physik  
der Ludwig-Maximilians-Universität  
München

vorgelegt von  
Silke Regine Kirchner  
aus Ulm

München, 2014

Erstgutachter: Prof. Dr. Jochen Feldmann

Zweitgutachter: Prof. Dr. Joachim Rädler

Vorsitz: Prof. Dr. Erwin Frey

Weiterer Prüfer: Prof. Dr. Jan Lipfert

Ersatzprüfer: Prof. Dr. Tim Liedl

Tag der mündlichen Prüfung: ~~XX~~ 06.05.2015

*The cover picture of this thesis was designed by Dipl.-Ing. Christoph Hohmann (Nanosystems Initiative Munich). It illustrates a dual infrared laser beam system that is used for a simultaneous optical trapping of a bacterium and a silica bead next to each other.*

*Für meine Eltern, Marie und Markus*



## Abstract

A novel and interesting approach to detect microfluidic dynamics at a very small scale is given by optically trapped particles that are used as optofluidic sensors for microfluidic flows. These flows are generated by artificial as well as living microobjects, which possess their own dynamics at the nanoscale.

Optical forces acting on a small particle in a laser beam can evoke a three dimensional trapping of the particle. This phenomenon is called optical tweezing and is a consequence of the momentum transfer from incident photons to the confined object. An optically confined particle shows Brownian motion in an optical tweezer, but is prevented from long term diffusion. A careful analysis of the motion of the confined particle allows a precise detection of microfluidic flows generated by an artificial or living source in the close vicinity of the particle. Thus, the particle can be used as a sensitive optofluidic detector. For this aim, several optical tweezers at different wavelengths are integrated into a dark-field microscope, combined with a high speed camera, to achieve a precise detection of the motion of the center-of-mass of the trapped particle.

With this unique experimental system, a gold sphere is used as an optofluidic nanosensor to analyze for the first time the microfluidic oscillations generated by a biological sample. Here, a freely swimming larva of Copepods serves as the living source of flow. However, even if the trapping laser wavelength is off-resonant to the plasmon resonance of the flow detector, a finite heating of the gold nanoparticle occurs which reduces the sensitivity of detection. To increase the sensitivity of the optofluidic detection, a non-absorbing, dielectric microparticle is introduced as the optofluidic sensor for the microflows. It enables a quantitative, two dimensional mapping of the vectorial velocity field around a microscale oscillator in an aqueous environment. This paves the way for an alternative and sensitive detection approach for the microfluidic dynamics of artificial and living objects at a very small scale. To this aim and as a first step, an optically trapped microhelix serves as a model system for the mechanical and dynamical properties of a living microorganism. An optical tweezer is implemented for initiating a light-driven rotation of the chiral microobject in an aqueous environment and the optofluidic detection of its flow field is established. The method is then adopted for the measurement of the microfluidic flow generated by a biological system with similar dynamics, in this case a bacterium. The experimental approach is used to quantify the time-dependent changes of the flow generated by the flagella bundle rotation at a single cell level. This is achieved by observing the hydrodynamic interaction between a dielectric particle and a bacterium that are both trapped next to each other in a dual beam optical tweezer. This novel experimental technique allows the extraction of quantitative information on bacterial motility without the necessity of observing the bacterium directly. These findings can be of great relevance for an understanding of the response of different strains of bacteria to environmental changes and to discriminate between different states of bacterial activity.





## Kurzfassung

Eine neue und interessante Möglichkeit mikrofluidische Dynamiken auf kleinster Skala zu untersuchen bieten optisch gefangene Teilchen, welche als optofluidische Sensoren für mikrofluidische Strömungen genutzt werden. Diese Strömungen können sowohl durch künstliche als auch lebende Mikroobjekte mit ihren nanoskaligen Eigendynamiken erzeugt werden.

Optische Kräfte, die innerhalb eines Laserstrahls auf ein kleines Partikel wirken, können ein dreidimensionales Einfangen des Partikels hervorrufen. Dieses Phänomen wird optische Pinzette genannt und ist eine Folge des Impulsübertrages von einfallenden Photonen auf das gefangene Objekt. Ein optisch gefangener Partikel zeigt Brownsche Bewegung in einer optischen Pinzette, wird aber durch diese an einer weitreichenden Diffusion gehindert. Eine sorgfältige Analyse der Bewegung des eingefangenen Partikels ermöglicht eine präzise Detektion mikrofluidischer Strömungen, welche in unmittelbarer Nähe des Teilchens durch eine künstliche oder biologische Quelle erzeugt werden. Damit kann das Teilchen als sensibler optofluidischer Detektor verwendet werden. Zu diesem Zweck werden mehrere optische Pinzetten mit unterschiedlichen Wellenlängen in ein Dunkelfeldmikroskop integriert um, verbunden mit einer Hochgeschwindigkeitskamera, eine genaue Erfassung der Mittelpunktswegung des eingefangenen Partikels zu erzielen.

Mit diesem einzigartigen Versuchssystem wird zunächst eine Goldsphäre als optofluidischer Nanosensor verwendet, um erstmalig mikrofluidische Oszillationen, die durch eine biologische Probe erzeugt werden, zu erfassen. Hierbei dient eine frei schwimmende Larve der Copepoden als lebendige Strömungsquelle. Jedoch erfolgt ein endliches Heizen des Goldnanopartikels selbst wenn die Wellenlänge des Lasers nicht resonant zur Plasmonresonanz des Strömungsdetektors ist, was die Sensitivität der Detektion vermindert. Um die Empfindlichkeit der optofluidischen Detektion zu erhöhen, wird ein nicht absorbierendes, dielektrisches Mikropartikel als optofluidischer Sensor für mikrofluidische Strömungen benutzt. Dieser ermöglicht eine quantitative, zwei dimensionale Abbildung des vektoriiellen Geschwindigkeitsfeldes um einen Mikrooszillator in wässriger Umgebung. Dies ebnet den Weg für eine alternative und präzise Detektionsmethode der mikrofluidischen Dynamiken künstlicher und lebender Objekte auf kleinster Skala. Dafür und in einem ersten Schritt, dient eine optisch gefangene Mikrohelix als Modellsystem für die mechanischen und dynamischen Eigenschaften eines lebenden Mikroorganismus. Eine optische Pinzette wird verwendet um eine lichtgesteuerte Drehung des chiralen Mikroobjekts in einer wässrigen Umgebung zu initiieren. Die optofluidische Detektion mit einer optisch angetriebenen Mikrohelix als Strömungsquelle wird etabliert. Diese Methode wird dann für die Messung der mikrofluidischen Strömung, die durch ein ähnliches biologisches System, ein Bakterium, generiert wird angewandt. Die experimentelle Herangehensweise wird genutzt, um die zeitabhängige Änderung der Strömung, die von der Rotation des Flagellenbündels des Bakteriums erzeugt wird, zu quantifizieren. Dies wird durch eine Beobachtung der hydrodynamischen Wechselwirkung zwischen einem dielektrischen Partikel und einem Bakterium, welche nebeneinander in einer Zweistrahl-Pinzette eingefangen sind, erreicht. Die neuartige experimentelle Technik ermöglicht die Extraktion von quantitativen Informationen über die bakterielle Beweglichkeit ohne die Notwendigkeit das Bakterium direkt beobachten zu müssen. Diese Informationen können von hoher Bedeutung für das Verständnis der Reaktion verschiedener Bakterienstämme auf Umweltveränderungen und für die Unterscheidung zwischen verschiedenen Zuständen der bakteriellen Aktivität sein.



## List of Publications and Awards

S. R. Kirchner et al., Membrane composition of jetted lipid vesicles: a Raman spectroscopy study. *J. Biophotonics* **5**, No. 1, 40-46 (2012).

S. R. Kirchner, S. Nedev, S. Carretero-Palacios, A. Mader, M. Opitz, T. Lohmüller, and J. Feldmann, Direct optical monitoring of flow generated by bacterial flagellar rotation. *Appl. Phys. Lett.* **104**, 093701 (2014).

S. R. Kirchner, M. Fedoruk, T. Lohmüller, and J. Feldmann, Analyzing the Movement of the Nauplius 'Artemia salina' by Optical Tracking of Plasmonic Nanoparticles. *J. Vis. Exp.* **89**, e51502 (2014).

S. Nedev, S. Carretero-Palacios, S. R. Kirchner, F. Jäckel and J. Feldmann, Microscale mapping of oscillatory flows. *Appl. Phys. Lett.* **105**, 161113 (2014).

S. R. Kirchner, L. J. Anderson, D. Schamel, C. Zensen, P. Fischer, T. Lohmüller, and J. Feldmann, Focused optical beams for Microfluidic Characterization of Chiral Microobjects, in preparation.

P. Urban, S. R. Kirchner, T. Lohmüller and J. Feldmann, Switching membrane permeability by plasmonic heating of gold nanoparticles, in preparation.

### Awards:

**Erwin Schrödinger Society Poster Award**, *BioNanoMed* 2014, Erwin Schrödinger Society for Nanosciences, Poster title: Monitoring of flagellar rotation of bacterial cells with optical tweezers.

**NIM<sup>1</sup> Poster Award 2013**, Poster title: Ultrasensitive Detection of Bacteria Mobility with Optical Tweezers.

**Award for best Poster**, *NIM workshop "Young Ideas in Nanoscience"* 2013, Poster title: Ultrasensitive Detection of Bacteria Mobility with Optical Tweezers.

---

<sup>1</sup> NIM: Nanosystems Initiative Munich;



## Conference contributions

Talk “Concepts for sensing and driving helical microbiological objects” at the *Workshop on Photonics and Optoelectronics*, Hirschegg-Kleinwalsertal, Austria, September/October 2014

Talk “Novel nano-optical concepts for sensing and driving helical microbiological objects” at the *SPIE Optics + Photonics symposium 2014*, Convention Center San Diego, United States, August 2014

Poster presentation at the *NIM<sup>2</sup> Workshop: “Young Ideas in Nanoscience”*, München, Germany, November 2013 (honored with a **Poster Award**)

Invited Talk “Research at LMU on Raman Spectroscopy, Optothermal Manipulation and Optical Tweezers” at the *Chair for Chemistry and Biochemistry*, Prof. Paul Weiss, California NanoSystems Institute, University of California Los Angeles, America, October 2013

Invited talk “Monitoring Bacteria Activity with Optically Trapped Microparticles” at the *Chair for Experimental Physics: Soft Matter Physics and Biophysics*, Prof. Dr. Joachim Rädler, Ludwig-Maximilians-Universität München, Germany, April 2013

Poster presentation at the *NIM/iNano Winterschool 2013*, Kirchberg (Tyrol), Austria, March 2013 (honored with a **Poster Award**)

Poster presentation at the *NIM-Graduate Program Summer Retreat 2012*, Garmisch-Partenkirchen, Germany, June 2012

Poster presentation at the *Seoul NanoHealth 2011, 5<sup>th</sup> Annual Symposium on Nanobiotechnology*, Seoul, South Korea, November 2011

Participant of the *42nd IFF Spring School 2011, Macromolecular Systems in Soft and Living Matter*, Jülich, Germany, February 2011

Talk “Diffusion in a lipid bilayer” at the workshop *From Biophotonics to Optoelectronics*, Riezlern, Austria, September 2011

Poster presentation at the *Sonder-Forschungs-Bereich 449 International Meeting, From Protein Structure to Membrane Dynamics*, Berlin, Germany, December 2010

Talk “Microfluidic generation of phospholipid vesicles” at the *Deutsche Physikalische Gesellschaft Frühjahrstagung*, Regensburg, Germany, March 2010

---

<sup>2</sup> NIM: Nanosystems Initiative Munich;



# Contents

<b>Abstract</b>	<b>I</b>
<b>Kurzfassung</b>	<b>III</b>
<b>List of Publications and Awards</b>	<b>V</b>
<b>Conference contributions</b>	<b>VII</b>
<b>Contents</b>	<b>IX</b>
<b>1. Introduction</b>	<b>1</b>
<b>2. Fundamentals</b>	<b>5</b>
2.1 Optical forces	6
Polarizability of a homogeneous sphere	9
Lorenz Mie theory	12
Chapter summary	17
2.2 Motion of an optically trapped particle	18
Diffusion	19
Displacement of an optically trapped particle	23
Power spectrum of an optically trapped particle	25
Chapter summary	26
2.3 Hydrodynamics at low Reynolds numbers	27
Reynolds number	27
Equations of change during transport phenomena	29
Locomotion of microbiological objects at low Reynolds number	33
Chapter summary	33
2.4 Dynamics of bacterial cells	34
Bacterial cell structure and filament rotation	34
Bacterial motility: “Tumbling” and “running” states	37

Chapter summary .....	40
<b>3. Methods and Materials .....</b>	<b>41</b>
3.1 Dark-field microscopy equipped with optical tweezers .....	42
3.2 Bacterial cell preparation .....	48
3.3 UV/Vis spectrophotometer.....	50
3.4 Preparation of microscope glass slides .....	51
3.5 Microfluidic flow detectors.....	51
3.6 Single particle-tracking and data analysis.....	52
<b>4. Optical driving and sensing of helical and biological microobjects.....</b>	<b>55</b>
4.1 Application of a plasmonic nanoparticle as optofluidic sensor for oscillations generated by a living microorganism.....	56
Optical forces on a plasmonic nanoparticle .....	57
Characterization of the microbiological flow source.....	60
Analysis of the movement of a Nauplius by optical tracking of an optically confined gold nanoparticle .....	61
Chapter summary and outlook .....	65
4.2 Application of a dielectric microparticle as optofluidic sensor for oscillatory flows .....	66
Optical forces on a dielectric microparticle .....	67
Characterization of the dipolar flow source .....	71
Microscale mapping of an oscillatory flow.....	72
Chapter summary and outlook .....	76
4.3 Optical driving and sensing of helical microstructures in a fluidic environment ..	78
Characterization of an optically confined microhelix.....	79
Establishing the flow detection around an optically confined microhelix .....	88
Chapter summary and outlook .....	99



4.4	Sensing the microfluidic flow generated by a single bacterial cell .....	101
	Characterization of a trapped bacterial cell by direct observation.....	103
	Microfluidic characterization of a trapped bacterial cell .....	106
	Chapter summary and outlook .....	114
<b>5.</b>	<b>Conclusion and Outlook .....</b>	<b>117</b>
<b>Appendix</b>	<b>.....</b>	<b>123</b>
<b>Abbreviations</b>	<b>.....</b>	<b>127</b>
<b>Bibliography</b>	<b>.....</b>	<b>129</b>
<b>Acknowledgements</b>	<b>.....</b>	<b>141</b>
<b>Curriculum Vitae</b>	<b>.....</b>	<b>143</b>



# 1. Introduction

In the last few years, an ever increasing use of optical tweezers as sensitive tool for the manipulation and observation of isolated or few micro- and nanoobjects has been reported<sup>1-8</sup>. Optical tweezers have been applied to exert calibrated forces on nano- and microparticles with a variety of applications ranging from optical stamping<sup>9, 10</sup> to microfabrication<sup>11, 12</sup>. More recently, optically trapped gold nanoparticles and single molecules were shown to be sensitive detection tools for acoustic waves<sup>13, 14</sup>.

On the other hand, microfluidic flows reveal special properties and are particularly characterized by laminar flow. The occurrence of special physical phenomena in microfluidics are of high relevance for diverse scientific areas, i.e. bioanalysis, optics or information technology<sup>15</sup>. Thus, it is of great importance to use the advantages of hydrodynamics at low Reynolds numbers and to push forward the development of the detection possibilities of microfluidic flows that result from artificial and biological microobjects.

The latter reveal very complex motion behaviors at the nanoscale which cannot be detected easily since resolution difficulties and optical detection limits are encountered. Typical remedial measurements are fluorescence microscopy to investigate microbiological dynamics which in turn can influence the natural behavior of the microorganism<sup>16</sup>. An analysis of the microfluidics around an oscillating micro- or nanobiological source offers an alternative experimental approach to the commonly used optical detection methods. For the realization of this idea, fluidic sensors as existing to date need to be fine-tuned for this specific application, since an ultrasensitive detection of the hydrodynamics and their detailed understanding is eminently important for this aim. In this work, trapped particles serve as microfluidic sensors. Through the investigation of their motion within the optical trap influenced by a flow field generated in their vicinity, conclusions can be drawn on the movement of the object responsible for the flow field. This can be a living microorganism with its own dynamics at the nanoscale, or an artificial object.

---

The final goal of this work is the analysis and characterization of the microfluidic dynamics generated by a single bacterial cell by using an optofluidic sensor bead trapped in an optical tweezer. From that, information on the bacterial mobility can be obtained that cannot be extracted from a common investigation with dark-field microscopy.

In Chapter 2, the fundamental theoretical background necessary to understand this thesis is presented. In general, optically trapped particles are used as optofluidic sensors for microfluidic flows. In the first part of this Chapter, the fundamentals of optical forces acting on a small particle are explained. Optical trapping occurs due to momentum transfer from the laser beam to the confined object. In the second section, the motion of a trapped particle is described. The third part focuses on hydrodynamics at low Reynolds number, which are relevant for the regimes regarded in this work. The creeping motion equations are derived and the physical cause of microbiological swimming at low Reynolds number is discussed. Finally, the mechanical and dynamical properties of bacterial cells are explained. An introduction to different cell structures and to filament rotation as locomotion mechanism is given.

In Chapter 3, the methods and materials used in this work are defined and characterized. The first section of this Chapter describes the integration of several optical tweezers at different wavelengths into a dark-field microscope. The optical setup was constructed for this thesis and in combination with a high speed camera it was possible to achieve a very precise detection of the performed experiments. In the second part, the chemical preparation of the bacteria cells that served as living sources of flow is described. For the measurement of the optical density of the bacteria cultures an UV/Vis spectrometer was used. In the next part, the preparation of the microscope glass slides is presented briefly and the particles used as microfluidic flow detectors are characterized. The last section contains information about single particle-tracking and data analysis. Fast Fourier transformation of the time-dependent x- and y-displacement of the flow source and of the optofluidic sensor is the fundamental concept of data evaluation.

Chapter 4 contains the results that were achieved in this work and which led to the final aim to investigate the microfluidic dynamics of a single bacterial cell on the nanoscale. In section 4.1, I will show how a single gold sphere can be used as an optofluidic nanosensor to detect for the first time the dynamics of a microbiological sample. To avoid

an enhancement of thermal fluctuations in the system and thus to increase the sensitivity of optofluidic detection, part 4.2 seizes the idea to use a non-absorbing dielectric microparticle as optofluidic sensor of oscillatory flows. It allows a quantitative mapping of the vectorial velocity field in two dimensions around a microscale oscillator in water. The optofluidic method introduced in this Chapter paves the way for in-situ characterization of fast mixing microscale devices and for new detection methods able to provide location and recognition of moving sources that can be applied to both artificial and living microobjects with their own dynamics at the nanoscale. In a first step, an optically confined and rotating microhelix is used in section 4.3 to model the mechanical and dynamical properties of the living organism. The Chapter describes the use of an optical tweezer for the generation of a light-driven rotation of a chiral microobject in an aqueous environment. A rotating helical microstructure serves as a model system for the mechanical and dynamical properties of a living bacterial cell. The focus of investigation in this section is the establishment of the optofluidic detection method with an optically driven microhelix as source of flow. Finally, in part 4.4, I will report for the first time on a highly sensitive approach to measure and quantify the time-dependent changes of the flow generated by the flagella bundle rotation of a single bacterial cell. This is achieved by observing the interaction between a silica particle and a bacterium, which are both trapped next to each other in a dual beam optical tweezer.



## 2. Fundamentals

*In this Chapter, the fundamental theoretical background necessary to understand this thesis is presented. In general, optically trapped particles are used as optofluidic sensors for microfluidic flows that are inter alia generated by individual bacterial cells.*

*In the first part of this Chapter, the fundamentals of optical forces acting on a small particle are explained. Optical trapping occurs due to momentum transfer from the laser beam to the confined object. In the second section, the motion of a trapped particle is described. An optically confined particle shows Brownian motion within a harmonic trapping potential that prevents the particle from long term diffusion. The third part focuses on hydrodynamics at low Reynolds number which are relevant for the regimes regarded in this thesis. The creeping motion equations are derived and the physical cause of microbiological swimming at low Reynolds numbers is discussed. Finally, the mechanical and dynamical properties of bacterial cells are explained. An introduction to different cell structures and to filament rotation as locomotion mechanism is given.*

---

## 2.1 Optical forces

In 1970, *Arthur Ashkin* published his work on the impact of light on microparticles <sup>1</sup>. He reported about the observation that microspheres are drawn toward a laser beam axis and are then accelerated along the beam propagation direction (Figure 2.1 (a)). In the subsequent step, he implemented two counter propagating laser beams and succeeded to trap microspheres in the symmetry point of the lasers in 3D (Figure 2.2 (b)) <sup>1</sup>.

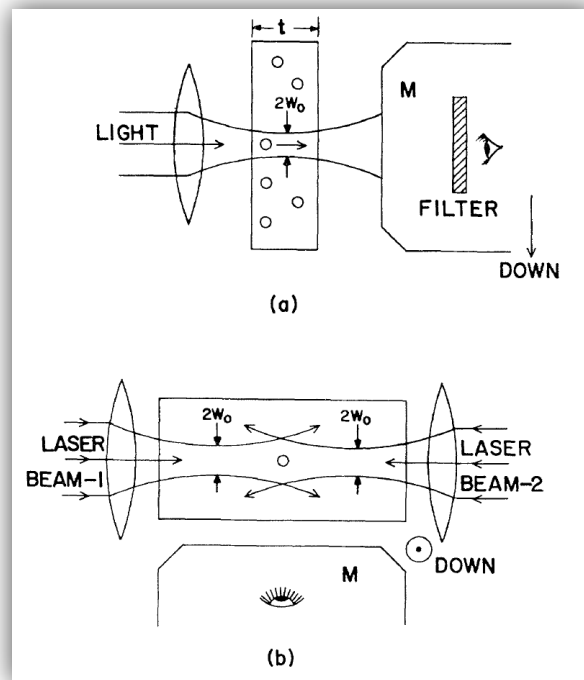


**Figure 2.1:** The pioneering work of A. Ashkin launched many optical tweezer applications. (a) microparticles are pushed along the beam propagation of a focused laser beam and are observed with a microscope M. (b) Two counter propagating laser beams rendered it possible to trap microspheres in their symmetry point in three dimensions. (Taken from 1).

Furthermore, A. Ashkin observed that even a *single* strongly focused laser beam allows a 3D trapping of microparticles <sup>2</sup>. Based on Ashkin's pioneering work <sup>17</sup>, several experimental approaches for the implementation of so called optical traps have been established: the optical trap due to two counter propagating laser beams, the single beam gradient trap, and optical tweezers that are realized by fiber optics <sup>18</sup>.



Different theories that describe the physical cause of the trapping phenomenon have been developed in literature. In general terms, optical trapping is a consequence of momentum transfer from light to an object. The applicability of a certain theory depends on the ratio between the characteristic length (radius) of the particle  $a$  and the vacuum wavelength  $\lambda$  of the trapping beam as well as on its focusing. Furthermore, the theoretical description depends on the light-matter interaction due to the material properties of the trapped object.

Three different size regimes for the ratio between the particle radius  $a$  and the trapping wavelength  $\lambda$  are considered (Figure 2.1) <sup>19,20</sup>:

- The Rayleigh regime:  
In this regime, the particle size has a sub-wavelength dimension with a radius  $a \ll \frac{\lambda}{20}$ . The 1<sup>st</sup> order dipole approximation of the Lorenz Mie theory can be used for the calculation of optical forces (Figure 2.2 (a)) <sup>19</sup>.
- The ‘Generalized Lorenz Mie theory’ (GLMT) allows for the description of forces acting on an optically trapped particle with a radius  $a$  at the order of  $\lambda$  (Figure 2.2 (b)) <sup>21</sup>.
- For objects with radii  $a \gg 10 \lambda$ , the ray or geometric optics approach can be used for the explanation of optical forces (Figure 2.2 (c)). This theory was already proposed by A. Ashkin <sup>2,38</sup>.

The forces acting on an optically trapped particle do not only depend on the ratio between the radius of the particle and the respective trapping wavelength, but also on the physical interaction between the incident electromagnetic field and the trapped object due to its material properties. The polarizability of a material gives information about this light-matter interaction. The polarizability  $\alpha$  of a particle is connected to the refractive index  $n$  by the dielectric (response) function  $\varepsilon(\omega)$ .

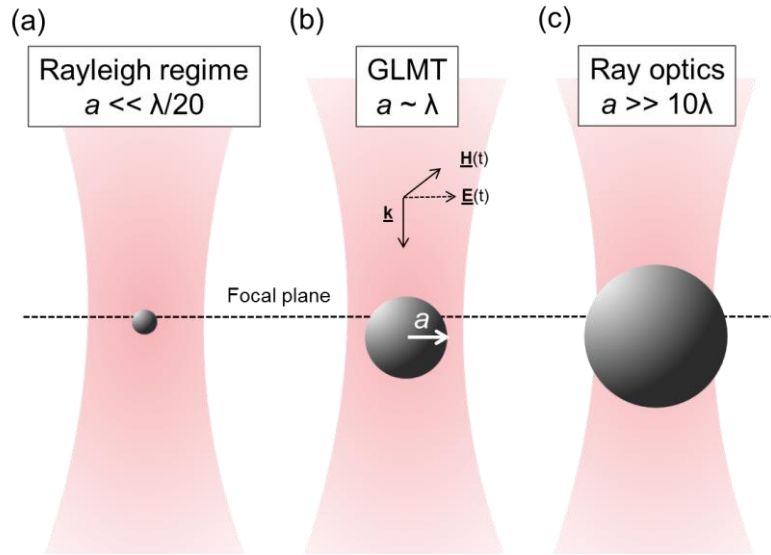


**Figure 2.2:** Schematic of three particle sizes in the electromagnetic field of a focused Gaussian laser beam with wavelength  $\lambda$ : (a) Rayleigh regime  $a \ll \lambda/20$ . Optical forces can be described by the 1<sup>st</sup> order of the Lorenz Mie theory. (b) GLMT regime  $a \sim \lambda$ . Optical forces are derived from the assumption of a focused Gaussian beam, Fresnel diffracted on the sphere. (c) Ray optics regime  $a \gg 10\lambda$ . In this regime, the geometrical optics approach is valid.

In this thesis, optically trapped dielectric microparticles as well as gold nanoparticles were used as optomechanical detectors of microfluidic flow patterns. In order to understand the light-matter interaction between trapping beam and particle, the first section of this Chapter elucidates the polarizabilities of small gold and dielectric spheres.

For the calculation of the optical forces confining a gold nanoparticle, the second part of this Chapter contains a summary of the Lorenz Mie theory with focus on the 1<sup>st</sup> order (dipole) approximation. The forces are calculated in Chapter: Optical forces on a plasmonic nanoparticle.

For the calculation of the optical forces acting on dielectric microparticles, the GLMT is needed. A summary of this theory and the calculation of the optical forces can be found in Chapter: Optical forces on a dielectric microparticle.

### Polarizability of a homogeneous sphere

The polarizability  $\alpha$  of an object describes its reaction on an incident electric wave that has a frequency  $\omega$ . The external electric field induces a polarization within the object. Its polarizability depends on:

(1) the frequency-dependent dielectric function  $\varepsilon(\omega)$  of the object, and

(2) the volume of the object. The polarizability volume of a sphere is  $V_s = \frac{4}{3}\pi a^3$  with  $a$  being the radius of the sphere.

For a homogenous, isotropic sphere in the Rayleigh regime, the polarizability  $\alpha$  can be derived from the *electrostatic dipole approximation*<sup>22, 23</sup>. In this approximation, a static and uniform external electric field  $\mathbf{E}$  induces a dipole moment  $\mathbf{p} = \alpha \varepsilon_0 \varepsilon_m \mathbf{E}$  within the particle with the dielectric function of the medium  $\varepsilon_m$  and the vacuum permittivity  $\varepsilon_0 = 8.854 \times 10^{-12}$  [F/m]<sup>23</sup>. The polarizability  $\alpha$  of the sphere is then:

$$\alpha = 4\pi a^3 \frac{\varepsilon_s(\omega) - \varepsilon_m(\omega)}{\varepsilon_s(\omega) + 2\varepsilon_m(\omega)} \quad (2.1.1)$$

with the radius of the sphere  $a$ , the dielectric function of the sphere  $\varepsilon_s(\omega)$  and the surrounding medium  $\varepsilon_m(\omega)$ <sup>22, 23</sup>. Equation 2.1.1 is of the same structure as the *Clausius-Mossotti* relation<sup>23</sup>.

The polarizability of Rayleigh spheres of certain material depends on their material specific response function. In this work, trapped gold and silicon dioxide particles were used as optofluidic detectors. Therefore the dielectric functions of these two materials will be discussed in the next two subchapters.

---

### 2.1.1.1 Response function and polarizability of a gold sphere

When a gold structure is exposed to an incident electric field, free electrons in the sp-band are excited. The collective oscillation of the free electron gas and the damping due to collisions with the metal ions can be described by the *Drude-Sommerfeld* theory<sup>24</sup>. This model derives the frequency-dependent, complex dielectric function of a gold sphere  $\varepsilon_s(\omega)$  as<sup>24, 25, 26</sup>:

$$\varepsilon_s(\omega) = \varepsilon_\infty - \frac{\omega_p^2}{\omega^2 + i\Gamma\omega} = \varepsilon' + i\varepsilon'' \quad (2.1.2)$$

with the plasma frequency  $\omega_p = \frac{Ne^2}{\varepsilon_0 m_e}$  of the resonant plasma oscillation of the free electron gas, the damping constant  $\Gamma$ , the electron density  $N$ , the electron mass  $m_e$  and a correction term for the background permittivity of the lattice ions  $\varepsilon_\infty$ . In the Drude-Sommerfeld theory, interband transitions of electrons are neglected which also contribute to the dielectric function. For the experimental configurations in this work, no interband excitations are expected<sup>26</sup>. Hence, the analytic expression given by the Drude-Sommerfeld theory was used for the calculation of the polarizability.

It is evident from equations 2.1.1 and 2.1.2 that the polarizability  $\alpha$  of a gold nanoparticle is wavelength dependent and complex:

$$\alpha = \alpha' + i\alpha'' \quad (2.1.3)$$

with the real part  $\alpha'$  and the imaginary part  $\alpha''$ .

For gold particles that do not satisfy the Rayleigh approximation, equation 2.1.1 can be expanded to:

$$\alpha = \frac{1 - \frac{1}{10}(\varepsilon_s + \varepsilon_m)x^2 + O(x^4)}{\left(\frac{1}{3} + \frac{\varepsilon_m}{\varepsilon_s - \varepsilon_m}\right) - \frac{1}{30}(\varepsilon_s + 10\varepsilon_m)x^2 - i\frac{4\pi^2\varepsilon_m^2}{3}\frac{V}{\lambda_0^3} + O(x^4)} V \quad (2.1.4)$$

with  $x = \frac{\pi a}{\lambda}$ ,  $a$  being the radius of the particle and  $\lambda$  being the vacuum wavelength of the laser beam<sup>27</sup>.

In this thesis, gold nanoparticles with a diameter of 60 nm and a trapping laser wavelength of 1064 nm were used, thus equation 2.1.1 served as a sufficient basis for the calculation of optical forces on the noble metal nanospheres (cp. Chapter: Optical forces on a plasmonic nanoparticle).

### 2.1.1.2 Response function and polarizability of a silicon dioxide sphere

In general, the polarizability  $\alpha$  is a scalar for isotropic dielectric bodies<sup>19</sup>. For a non-absorbing silicon dioxide sphere, the wavelength-dependent response function  $\varepsilon_s(\omega)$  can be estimated as:

$$\varepsilon_s(\omega) \cong \varepsilon_s = n_{silica}^2 = 2.1 \quad (2.1.5)$$

since the refractive index of silicon dioxide  $n_{silica} = 1.45$  can be taken as constant for a wavelength regime between  $1 \mu m < \lambda < 3 \mu m$  of the incident wave<sup>19, 28</sup>. The dielectric function for silicon dioxide is therefore real and frequency independent in this wavelength range. Inserting 2.1.5 in equation 2.1.1 gives the polarizability for a silicon dioxide sphere in the Rayleigh regime:

$$\alpha = 4\pi a^3 \frac{\varepsilon_s(\omega) - \varepsilon_m(\omega)}{\varepsilon_s(\omega) + 2\varepsilon_m(\omega)} = 4\pi a^3 \frac{n_{rel}^2 - 1}{n_{rel}^2 + 2} \quad (2.1.6)$$

In equation 2.1.6, the relative index of refraction  $n_{rel} = n_{silica}/n_m$  with  $n_m$  being the refractive index of the surrounding medium was used. For a silicon dioxide particle in water, the relative refractive index is  $n_{rel} = 1.45/1.33 = 1.09$  with  $n_{silica} = 1.45$  and  $n_{water} = 1.33$ .

In this work, silicon dioxide microparticles served as optofluidic sensors. Equation 2.1.6 is valid for Rayleigh particles, but can be expanded for larger dielectric particles of arbitrary shape by means of a discrete-dipole approximation<sup>29</sup>.

---

### Lorenz Mie theory

The interaction of light with a particle results in a momentum transfer from the light to the object due to absorption, scattering or emission of photons and due to the fact that electric dipoles are drawn toward the highest amplitude of the electromagnetic field <sup>19</sup>. Momentum transfer is also the physical answer to question on the cause of optical trapping.

The absorption and scattering of an incident *planar* electromagnetic wave by a homogenous and charge free sphere was already described by the theory of Gustav Mie, Ludvig Lorenz and Peter Debye finalized in 1908, the Lorenz Mie theory. In this theoretical approach, the planar incident electromagnetic wave is expanded in an infinite series of vector spherical harmonics that solve the wave equation <sup>22</sup>. The scattered electromagnetic field and the field inside the sphere are expressed by a superposition of the electromagnetic normal modes of the spherical particle, each mode contribution weighted by a coefficient <sup>22</sup>.

Taking into account the boundary conditions, the electric field inside the sphere  $\mathbf{E}_i$  and the scattered electric field  $\mathbf{E}_s$  can be written as a superposition of the electromagnetic normal modes  $\mathbf{N}_{e,ln}, \mathbf{M}_{o,ln}$  of the particle:

$$\mathbf{E}_i = \sum_{n=1}^{\infty} E_n (c_n \mathbf{M}_{o,ln} - i d_n \mathbf{N}_{e,ln}) \quad (2.1.7)$$

$$\mathbf{E}_s = \sum_{n=1}^{\infty} E_n (i a_n \mathbf{N}_{e,ln} - b_n \mathbf{M}_{o,ln}) \quad (2.1.8)$$

The indices *e* and *o* stand for even and odd modes and  $n, l \in \mathbb{N}$ .  $E_n$  can be written as  $E_n = i^n E_o (2n + 1)/n(n + 1)$  with  $E_o$  being the peak electric field strength.  $c_n$  and  $d_n$  are the coefficients for the field inside the particle.  $a_n$  and  $b_n$  are the scattering coefficients. The coefficients weight each mode in the superposition. The coefficients  $a_n$  describe the transversal magnetic (TM) modes (electric type wave) and the coefficients  $b_n$  the transversal electric (TE) modes (magnetic type wave). The corresponding internal and scattered magnetic fields can be calculated by taking the curl of equation 2.1.7 and 2.1.8 <sup>22</sup>.

The first order of the normal modes of the particle (1<sup>st</sup> order Lorenz Mie theory) is equivalent to the field radiated by an electric dipole:

$$E_s \cong E_1(ia_1N_{e11} - b_1M_{o11}) \quad (2.1.9)$$

The 1<sup>st</sup> order Lorenz Mie theory approximation is therefore also called dipole approximation<sup>22</sup>.

In the following subChapter the dipole approximation is used to calculate the optical forces acting on a Rayleigh sphere.

### 2.1.1.3 Optical forces on a small particle

In the Rayleigh scattering regime, the incident electromagnetic field of the focused Gaussian beam is considered to be planar. For the electromagnetic field scattered by a small particle, the 1<sup>st</sup> order of the Lorenz Mie theory (equation 2.1.9) is valid. The 1<sup>st</sup> order of the normal modes of the particle characterize the field of a radiating dipole<sup>22</sup>. The dipole moment can be expressed by

$$\mathbf{p}(\mathbf{r}, t) = \varepsilon_m \alpha \mathbf{E}(\mathbf{r}, t) \quad (2.1.10)$$

with the permittivity or dielectric function of the medium  $\varepsilon_m = n_m^2 \varepsilon_0$ , the polarizability of the particle  $\alpha$ , the refractive index  $n_m$  of the medium and  $\varepsilon_0 = 8.854 \times 10^{-12}$  [F/m] as the vacuum permittivity<sup>19, 30</sup>.

For the derivation of the optical forces acting on a sub-wavelength sized spherical particle, the starting point is the Lorentz force  $\mathbf{F}(\mathbf{r}, t)$  acting on a point charge  $q$  moving with a velocity  $\mathbf{v}$  in an electromagnetic field

$$\mathbf{F}(\mathbf{r}, t) = q(\mathbf{E}(\mathbf{r}, t) + \mathbf{v} \times \mathbf{B}(\mathbf{r}, t)). \quad (2.1.11)$$

$\mathbf{E}(\mathbf{r}, t)$  stands for the position- and time-dependent electric field and  $\mathbf{B}(\mathbf{r}, t)$  represents the position- and time-dependent magnetic field<sup>30</sup>.

---

A substitution of the point charge  $q$  in equation 2.1.11 with the dipole moment  $\mathbf{p}(\mathbf{r}, t)$  (equation 2.1.10) leads to an expression for the electromagnetic force:

$$\mathbf{F}(\mathbf{r}, t) = [\mathbf{p}(\mathbf{r}, t)\nabla]\mathbf{E}(\mathbf{r}, t) + \frac{\partial\mathbf{p}(\mathbf{r}, t)}{\partial t} \times \mathbf{B}(\mathbf{r}, t) \quad (2.1.12)$$

Applying the vector identity  $(\mathbf{E}\nabla)\mathbf{E} = \nabla\left(\frac{E^2}{2}\right) - \mathbf{E} \times (\nabla \times \mathbf{E})$  and the Maxwell equation  $\nabla \times \mathbf{E} = -\frac{\partial}{\partial t}\mathbf{B}$  to formula 2.1.12, it can be written as:

$$\mathbf{F}(\mathbf{r}, t) = \alpha\varepsilon_m \left(\frac{\nabla|\mathbf{E}(\mathbf{r}, t)|^2}{2}\right) + \alpha\varepsilon_m \frac{\partial}{\partial t} [\mathbf{E}(\mathbf{r}, t) \times \mathbf{B}(\mathbf{r}, t)] \quad (2.1.13)$$

Averaging equation 2.1.13 over one period  $T = \frac{1}{\omega}$  leads to a time-independent expression for the electromagnetic force acting on a particle in the Rayleigh scattering regime:

$$\langle \mathbf{F}(\mathbf{r}, t) \rangle_T = \mathbf{F}(\mathbf{r}) = \frac{\alpha n_m}{2c} \nabla I(\mathbf{r}) \quad (2.1.14)$$

In this expression, the physical relation between the time-averaged modulus of the Poynting vector  $\langle |\mathbf{S}(\mathbf{r}, t)| \rangle_T$  and the intensity  $I(\mathbf{r})$  is used:  $I(\mathbf{r}) = \langle |\mathbf{S}(\mathbf{r}, t)| \rangle_T = \frac{n_m \varepsilon_0 c^2}{2} |\mathbf{E}(\mathbf{r}) \times \mathbf{B}(\mathbf{r})| = \frac{n_m \varepsilon_0 c}{2} |\mathbf{E}(\mathbf{r})|^2$ . Furthermore it is assumed that the temporal change of the intensity vanishes<sup>3 47, 48</sup>.

The complex polarizability  $\alpha$ , e.g., for gold nanoparticles, can be written as  $\alpha = \alpha' + i\alpha''$  (equation 2.1.3) with the real part  $\alpha'$  and the complex part  $\alpha''$ . Using this expression, equation 2.1.14 reads:

$$\mathbf{F}(\mathbf{r}) = \frac{\varepsilon_m}{4} [\alpha' \nabla (\bar{\mathbf{E}}(\mathbf{r})\mathbf{E}(\mathbf{r})) + \alpha'' \text{Im}\{\sum_i \bar{\mathbf{E}}_i(\mathbf{r})\nabla E_i(\mathbf{r})\}] \quad (2.1.15)$$

---

<sup>3</sup> It should be noted that this assumption is disputed in literature and an alternative approach leads to a different definition of optical forces (see equation 2.1.19).



$\bar{E}_i$  is the complex conjugate of  $E_i$ . Equation 2.1.15 is the main result of the theoretical derivation of an optical force,  $\mathbf{F}(\mathbf{r})$  acting on a Rayleigh particle with dipolar behavior. The force can be split into two components:

$$\mathbf{F}(\mathbf{r})_{grad} = \frac{\varepsilon_m}{4} \alpha' \nabla (\bar{\mathbf{E}}(\mathbf{r}) \mathbf{E}(\mathbf{r})) \quad (2.1.16)$$

and

$$\mathbf{F}(\mathbf{r})_{scat} = \frac{\varepsilon_m}{4} \alpha'' \text{Im} \{ \sum_i \bar{E}_i(\mathbf{r}) \nabla E_i(\mathbf{r}) \} \quad (2.1.17)$$

$\mathbf{F}(\mathbf{r})_{grad}$  is called the gradient force (Figure 2.3). This force is conservative and depends on the real part of the complex polarizability  $\alpha'$ . The gradient force acts for positive  $\alpha'$  along the field intensity gradient toward the point of highest field intensity. This is the focal point of a focused laser beam. A strong gradient force is achieved by a strong focusing of the trapping beam. The force scales with the particle volume  $\alpha' \sim a^3$ <sup>31</sup>.

$\mathbf{F}(\mathbf{r})_{scat}$  is the scattering force (Figure 2.3). The force is dissipative and depends on the imaginary part of the complex polarizability  $\alpha''$ . The scattering force points along the electric field propagation. The force scales with the scattering cross section of the particle, that is  $\langle C_{scat} \rangle \sim \alpha^2 \sim a^6$ <sup>31, 22</sup>.

Stable optical trapping in 3D (Figure 2.3) is achieved in case:

$$\mathbf{F}(\mathbf{r})_{grad} > \mathbf{F}(\mathbf{r})_{scat} \quad (2.1.18)$$

Changing the ratio between the imaginary and real part of the polarizability of the particle can thus determine the final trap stiffness<sup>31</sup>. In the case of gold nanoparticles, the ratio between the gradient and the scattering force can be tuned by varying the trapping laser wavelength. Furthermore, for a stable trapping, the gradient force has to be greater than the thermal forces acting on the particle (cp. Chapter: Diffusion). For the illustration of the three dimensional confinement of a gold nanoparticle in a laser trap the optical forces acting on the sphere were numerically simulated in Chapter: Optical forces on a plasmonic nanoparticle.

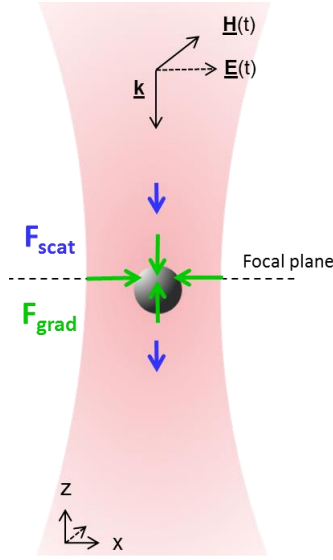


**Figure 2.3:** Sketch of an optically trapped particle. The gradient force acts along the field intensity gradient towards the point of highest field intensity. The scattering force points along the field propagation direction. A stable, 3D trapping is achieved in case  $\mathbf{F}(\mathbf{r})_{grad} > \mathbf{F}(\mathbf{r})_{scat}$ .

The approach as described so far (equations 2.1.16 and 2.1.17) is valid for optical forces acting on a gold nanoparticle, where the polarizability takes on a complex value. For the calculation of optical forces on a silicon dioxide bead with real polarizability, this description would mean that no scattering force acts on a dielectric particle which is wrong. Therefore, an alternative approach should be taken into account. Starting from equation 2.1.13 it was assumed that the temporal change of intensity is zero. This assumption is disputed for the presence of a scatterer, which is the spherical particle<sup>19</sup>. If the change of momentum density is taken into account, equation 2.1.14 becomes:

$$\mathbf{F}(\mathbf{r}) = \frac{\alpha n_m}{2c} \nabla I(\mathbf{r}) + \alpha n_m \frac{\Delta m(\mathbf{r})}{\Delta t} := \mathbf{F}(\mathbf{r})_{grad} + \mathbf{F}(\mathbf{r})_{scat} \quad (2.1.19)$$

With  $\Delta m$  being the change of momentum density per unit time  $\Delta t$ . The resulting force  $\Delta m(\mathbf{r})/\Delta t$  will accelerate the particle. The total optical force is now split into a gradient force that is proportional to the intensity gradient and a scattering force that describes the momentum transfer due to scattering processes<sup>19</sup>.

So far, the derivation of the optical forces for spherical particles in the Rayleigh regime was discussed. The presented approach for the description of optical forces fits well for optically trapped gold nanoparticles.

However, the silicon dioxide microparticles used in this work do not match into the Rayleigh regime, since their size dimensions are at the scale of the trapping beam wavelength. A more precise theoretical approach for these particles is given by the GLMT or the two-component force model by *A. Rohrbach* and *E.H.K. Stelzer*<sup>19</sup>. An explanation of the GLMT as well as a force calculation for dielectric microparticles can be found in Chapter: Optical forces on a dielectric microparticle.

### **Chapter summary**

This Chapter elucidated the material specific polarizabilities for gold and silicon dioxide particles in the Rayleigh scattering regime. The polarizability of a gold sphere is complex, whereas the polarizability of a dielectric particle takes on a real value.

The fundamentals of the Lorenz Mie theory were explained with a focus on the 1<sup>st</sup> order dipole approximation. This approximation is sufficient for the description of the optical forces acting on a gold nanoparticle. For dielectric Rayleigh particles with real polarizability, the temporal change of intensity has to be taken into account in this approach. Otherwise no scattering force would act on a dielectric sphere.

For (dielectric) particles with size dimensions at the scale of the trapping wavelength, the GLMT should be applied for the calculation of the optical forces. This approach is presented in Chapter: Optical forces on a dielectric microparticle.

---

## 2.2 Motion of an optically trapped particle

In 1827, while examining grains of pollen in water under a microscope, the botanist *Robert Brown* observed small particles that performed continuous random motion. This discovery has since then been known as *Brownian* motion<sup>32</sup>. The random walk of Brownian particles characterizes many physical phenomena like diffusion, osmosis or thermophoresis<sup>33,34</sup>.

Diffusion in turn plays an important role in lots of biological processes like cell motion or bacterial swimming. Cell motion in a channel guided system, for example, can be described by a superposition of diffusion-mediated transport and a constant drift velocity  $v_{drift}$ <sup>35</sup>. The drift velocity is the result of cellular polarization and self-propulsion. For studying biological diffusion processes fluorescence correlation spectroscopy has been used<sup>35,36,37</sup>.

The superposition of diffusion and drift is an ubiquitous physical phenomenon. The movement of an optically trapped particle can also be described as superposition of diffusive motion and constant drift velocity  $v_{drift}$ . The drift velocity arises from the external trapping force due to the optical tweezer.

For the definition of diffusion processes, either a microscopic or a macroscopic approach can be used. The mean field approach leads to Fick's equations that describe the spatial and temporal variation of inhomogeneous particle distributions<sup>38</sup>. In this Chapter, the microscopic approach is elucidated.

In the first part of this Chapter, the theoretical background of diffusion is explained. The movement of an optically trapped particle can be seen as a superposition of diffusion with directed motion. The second section focuses on the time-dependent displacement of a harmonically bound particle. Finally, in the last part the power spectrum of an optomechanical detector is described.

## Diffusion

The random and independent movement of small particles or molecules in a gas or liquid is called diffusion<sup>38</sup>. It is a consequence of the thermal energy those particles possess. In his work “Annalen der Physik”<sup>39</sup> *Albert Einstein* already postulated that the thermal energy of a small particle is  $E_{thermal} = \frac{k_B T}{2}$  with  $k_B$  being Boltzmann’s constant and  $T$  being the absolute temperature of the system. The kinetic energy of a particle with mass  $m$  averaged over time is<sup>38</sup>

$$\langle E_{kin} \rangle = \langle \frac{m v_i^2}{2} \rangle = \frac{k_B T}{2} \quad (2.2.1)$$

with  $i = x, y, z$ . In a many-particle system, collisions between the particles occur. Collisions between molecules in a gas lead to an equalization of initial inhomogeneous densities. In a liquid medium, suspended small particles undergo random movement due to the “bombardment” of the surrounding molecules. A particle receives momentum from the thermal fluctuations characterized by  $\frac{k_B T}{2}$ , but simultaneously its movement is damped due to the viscosity of the medium<sup>39,40</sup>. The mean free path length  $\bar{l}$  describes the distance a particle can travel between two collisions. The overall position of a particle after  $N$  collisions can be mathematically expressed by a three dimensional random walk with variable path length<sup>41</sup>.

### 2.2.1.1 Random walk

Three basic principles distinguish a (1D) random walk<sup>38,41</sup>:

- The single steps during a random walk are independent from each other,
- the probability of going to the right  $\Delta x = +l$  or to the left  $\Delta x = -l$  at each step is  $p$  and  $q$  respectively with  $p + q = 1$ , and
- all particles move independently from each other.

The discrete binominal distribution  $W_N(n)$  describes the probability that a particle steps  $n$  times to the right in  $N$  trials<sup>38,41</sup>:

---


$$W_N(n) = \frac{N!}{n!(N-n)!} p^n q^{N-n} \quad (2.2.2)$$

with the normalization

$$\sum_{n=0}^N W_N(n) = (p + q)^N = 1 \quad (2.2.3)$$

with  $n, N \in \mathbb{N}$  and  $p, q \in \mathbb{Q}$ . In case  $p$  is finite and  $Np \rightarrow \infty$  for  $N \rightarrow \infty$ , the asymptotic limit of the binominal distribution (2.2.2) is the Gaussian distribution<sup>38,41</sup>:

$$P(x) = \frac{1}{\sqrt{2\pi}\sigma} \exp\left(-\frac{(x-\bar{x})^2}{2\sigma^2}\right) \quad (2.2.4)$$

with  $x = nl$ ,  $\bar{x} = \bar{n}l = Npl$  and the standard deviation  $\sigma = \Delta nl = \sqrt{Npq} l$ .

The probability of finding  $x$  between  $x$  and  $dx$  is  $P(x)dx$  with

$$\int_{-\infty}^{\infty} P(x) dx = 1 \quad (2.2.5)$$

The distribution is symmetrical around the mean  $\bar{x}$ . The Gaussian function characterizes the diffusive movement of a particle. As long as no external forces act on the particle ( $F_{ext} = 0$ ), the random walk is non-biased. The probability of stepping to the right is the same as the probability of stepping to the left:  $p = q = \frac{1}{2}$ <sup>40</sup>. That means successive steps are independent from each other. The 1D spreading of a freely diffusing particle with time can be described by the mean square displacement (MSD):

$$\langle \Delta x^2(t) \rangle = 2Dt \quad (2.2.6)$$

with  $\Delta x(t) = x(t) - x_0$ , the initial position of the particle  $x_0$  and the diffusion coefficient  $D$ <sup>38, 42</sup>. Equation 2.2.6 implicates that the spreading for a freely diffusing particle increases with the square root of time<sup>38</sup>. In case of short time scales  $t \rightarrow 0$  and  $F_{ext,x} = 0$ , the motion of the particle becomes ballistic e.g.,  $\langle \Delta x^2(t) \rangle \sim t^2$ <sup>40</sup>. For a 2D or 3D system, equation 2.2.6 is  $\langle \Delta r^2(t) \rangle = 2nDt$  with  $n = 2, 3$ , respectively. An example of a 2D free diffusion can be the motion of a gold nanoparticle on a fluidic lipid bilayer<sup>43</sup>.

## 2.2.1.2 Diffusion with drift for a spherical particle

A randomly moving particle in liquid medium explores its surrounding fast and in return its environment strongly alters its trajectory<sup>40</sup>. As soon as an external, constant force  $F_{ext,i}$ ,  $i = x, y, z$  accelerates the particle ( $a_i = F_{ext,i}/m$ ), it experiences a finite drift velocity  $v_{drift,i}$  due to friction with surrounding molecules. Such an external force can be the restoring force  $F_{ext,i} = F_{rest}$  within an optical trap.

The overall motion of a diffusing particle exposed to an external force can be described by a biased random walk. With  $\tau$  being the time between two collisions, it can be shown that the drift velocity of the particle is<sup>38,41</sup>:

$$v_{drift,i} = \frac{1}{2} a_i \tau = \frac{1}{2} \frac{F_{ext,i}}{m} \tau \quad (2.2.7)$$

Due to the collisions, a frictional term is integrated into the equation of motion of a particle<sup>41</sup>:

$$m \dot{v}_{particle,i} = F_{ext,i} - \gamma v_{particle,i} \quad (2.2.8)$$

where  $\gamma$  stands for the frictional drag coefficient. With  $v_{particle,i}(\infty) = \frac{F_{ext,i}}{\gamma} = v_{drift,i}$  and equation 2.2.8 the frictional drag coefficient  $\gamma$  can be determined:

$$\gamma = \frac{2m}{\tau} \quad (2.2.9)$$

Inserting  $\gamma = \frac{2m}{\tau}$ ,  $D = \frac{l^2}{2\tau}$ ,  $v_i = \frac{l}{\tau}$  into equation 2.2.1 the fluctuation-dissipation theorem or *Einstein-Smoluchowski* relation can be derived<sup>38</sup>:

$$\gamma \cdot D = k_B \cdot T \quad (2.2.10)$$

---

This equation clearly points out that friction (dissipation) and diffusion (fluctuation) are related for the motion of a randomly moving particle in an external force field<sup>4</sup>.

A spherical particle with radius  $r$ , moving with velocity  $v_{drift}$  through viscous medium causes the medium to shear. The Stokes-equation (Chapter 2.3.1.3) yields the viscous drag on the sphere which is  $F = 6 \pi \eta r v_{drift}$  (equation 2.3.17). Here,  $\eta$  stands for the dynamic viscosity of the medium. Taking equations 2.2.7, 2.2.9 and 2.2.10 frictional drag and diffusion coefficient for an spherical object can be calculated<sup>38</sup>:

$$\gamma_{sphere} = 6 \pi \eta r \quad (2.2.11)$$

and

$$D_{sphere} = \frac{k_B T}{6 \pi \eta r} \quad (2.2.12)$$

For a particle with a radius  $r = 1 \mu m$  in water ( $\eta_{water} = 10^{-3} \text{ Ns/m}^2$ ), the drag and diffusion constant at 25 °C are<sup>38</sup>:

$$\gamma_{sphere} = 1.9 \cdot 10^{-5} \frac{\text{g}}{\text{sec}} \text{ and } D_{sphere} = 0.2 \frac{\mu\text{m}^2}{\text{sec}}.$$

With increasing temperature, the value of the diffusion constant increases and the spreading of the particle becomes broader (equation 2.2.6).

Furthermore, the gravitational sedimentation rate  $v_{sed.}$  for a spherical particle can be calculated by the Svedberg equation<sup>38</sup>

$$v_{sed.} = \frac{2r^2(\rho_s - \rho)g}{9\eta} \quad (2.2.13)$$

---

<sup>4</sup> A similar relation can be found for the mobility of charge carriers in a semiconductor.



Assuming a silica glass particle with radius  $r = 1 \mu\text{m}$  and specific gravity  $\rho_s = 2.35 \text{ g/cm}^3$  the sedimentation rate in water with density  $\rho = 1 \text{ g/cm}^3$  and viscosity  $\eta_{\text{water}} = 10^{-3} \text{ Ns/m}^2$  is:

$$v_{\text{sed.}} \cong 2.9 \frac{\mu\text{m}}{\text{sec}}$$

### Displacement of an optically trapped particle

As explained in Chapter 2.1, the total optical force acting on a particle can be split into a gradient  $\mathbf{F}(\mathbf{r})_{\text{grad}}$  and a scattering force  $\mathbf{F}(\mathbf{r})_{\text{scat}}$ . The gradient force points along the gradient of field intensity, toward the focal point of the objective. The trapped particle can be seen as harmonically bound within the trap, due to the gradient force distribution (Figure 2.2.1 (a)). For each dimension, the harmonicity of the potential can be written as  $U(x) = x^2 \kappa/2$  with  $\kappa$  being the trap stiffness<sup>13</sup>. Due to the scattering force which points along the beam propagation direction, the minimum of the harmonic potential is slightly below the focal point. A particle, optically confined by an optical tweezer, explores the harmonic trapping potential by Brownian motion but is hindered from long-term diffusion (Figure 2.2.1 (b))<sup>44</sup>.

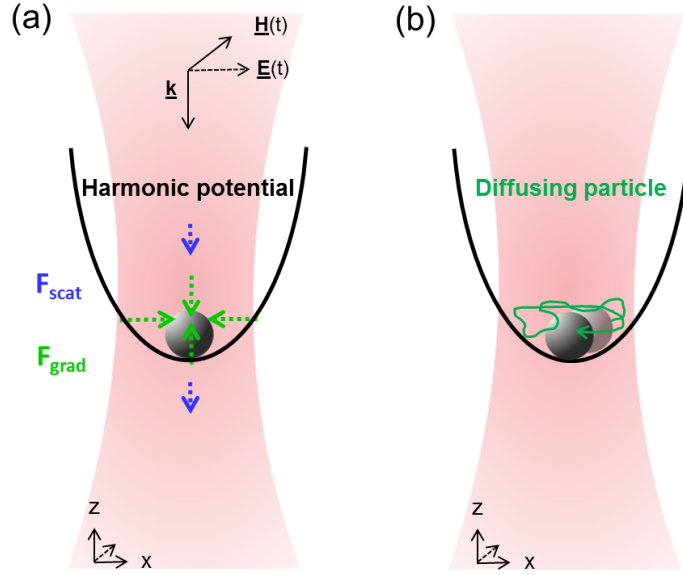


**Figure 2.2.1:** (a) a trapped particle can be seen as harmonically bonded within the tweezer, due to the gradient force distribution. Furthermore, the particle explores the harmonic trapping potential by Brownian motion but is hindered from long-term diffusion (b).

Within the harmonic potential, a linear restoring force  $\mathbf{F}_{rest}$  pulls the particle toward the trap center<sup>44, 45</sup>. This means, on the one hand, the particle is subjected to Brownian motion with the MSD  $\langle \Delta r^2(t) \rangle = 6Dt$  (in case of a sphere  $D_{sphere} = \frac{k_B T}{6\pi\eta r}$ ) but on the other hand, the particle feels the external restoring trapping force<sup>46</sup>. In one dimension, the restoring force can be written as  $F_{rest} = \kappa x_{particle}(t)$  with  $x_{particle}(t)$  being the displacement of the particle with respect to the trap center. The displacement  $x_{particle}(t)$  of the particle within the trap depends therefore on the temperature  $T$  as well as on the trap strength  $\kappa$ . The distribution of the particle position shows a Gaussian behavior with a standard deviation

$$\sigma_x^2 = \frac{k_B T}{\kappa} \quad (2.2.14)$$

around the trap center. For room temperature  $k_B T \cong 4 \text{ zJ}$ . Equation 2.2.14 is true for a “strong trap”. For a “soft trap”, the motion pattern of the trapped particle is similar to that of a freely diffusing particle<sup>44, 40</sup>. In this thesis only “strong traps” with laser powers at the order of  $P = 30 \text{ mW}$  after the objective are considered.

### Power spectrum of an optically trapped particle

The Langevin equation for an optically confined particle can be written as <sup>40, 45</sup>

$$\gamma v_{particle,x} + \kappa x_{particle}(t) = F(t)_{thermal} \quad (2.2.15)$$

Equation 2.2.15 reveals the balance of forces between the frictional drag force ( $\gamma v_{particle,x}$ ) plus the restoring spring force ( $\kappa x_{particle}(t)$ ) and the thermal force ( $F(t)_{thermal}$ ). Since the thermal force is randomly distributed, its average over time is zero and its Fourier transformation  $FFT(F(t)_{thermal})$  is constant (thermal noise) <sup>45, 46</sup>:

$$FFT(F(t)_{thermal}) = F(f) = \sqrt{4 \gamma k_B T} \quad (2.2.16)$$

Fourier transformation of both sides of equation 2.2.15 results in

$$2\pi\gamma (f_c - if) X(f) = F(f) \quad (2.2.17)$$

with  $X(f)$  being the Fourier transform of  $x_{particle}(t)$  and the characteristic frequency of the trap

$$f_c = \kappa/2\pi\gamma \quad (2.2.18)$$

With equation 2.2.16 it follows that

$$|X(f)|^2 = S_x(f) = \frac{k_B T}{\gamma \pi^2 (f_c^2 + f^2)} \quad (2.2.19)$$

$S_x(f)$  is the power spectrum of the time-dependent displacement of an optically trapped particle <sup>45, 46</sup>.  $S_x(f)$  denotes the distribution of thermal fluctuations over different frequencies  $f$ . For  $f \ll f_c$ :  $S_x(f) \cong \frac{4 \gamma k_B T}{\kappa^2}$  and for  $f \gg f_c$ :  $S_x(f) \sim 1/f^2$ . For the latter case, at very small time scales, the particle can be considered as freely diffusing and the restoring force of the harmonic potential does not have any influence on the power spectrum <sup>45</sup>.

---

### Chapter summary

In this Chapter, the motion of a spherical particle trapped in an optical tweezer was explained. The particle shows a short ranged diffusive behavior within the trapping potential that prevents the particle from long term diffusion.

The trap stiffness as well as the temperature determines the displacement of the particle with respect to the trap center. For a strong trap, the mean square displacement of the particle position is proportional to the invers of the trap stiffness.

The equation of motion for a harmonically bound particle describes the force balance between the frictional drag force plus the restoring spring force and the thermal force.

The power spectrum  $S_x(f)$  of a Brownian particle in an optical tweezer reveals a cut off frequency  $f_c$ . For frequencies  $f \ll f_c$  the power spectrum is proportional to  $\frac{1}{\kappa^2}$ . For  $f \gg f_c$ , the particle behaves as if it was freely diffusing.

### 2.3 Hydrodynamics at low Reynolds numbers

Optomechanical methods have been used to investigate flow conditions in microfluidic systems<sup>47,48</sup>. A novel optical concept to read out acoustic and microfluidic oscillations on the nanoscale was developed by A. Ohlinger et al.<sup>13</sup>. In this thesis, for the first time, the “nanoeear” concept is extended and transferred to read out unknown microfluidic flow fields around living organisms. Even though the dynamics of a microorganism are on the nanoscale and exhibit high frequencies, the microfluidic oscillations could be detected. This Chapter describes the theoretical background needed to understand microfluidic flow. The first part focusses on the definition of the Reynolds number and its relevance for flow conditions. In the second sections, the equations of change during transport phenomena are derived. Since in this work also bacteria motility was studied, the last part of this Chapter explains locomotion strategies of microorganisms at low Reynolds numbers.

#### Reynolds number

For the experiments performed in this work, mainly water was used as a fluid. Water can be treated as incompressible. The density of water for example increases by only 0.5 % at a pressure increase from 1 to 100 atmospheres<sup>49</sup>. Furthermore, water (and most gases under normal conditions) belongs to the group of Newtonian fluids. In Newtonian fluids, the magnitude of the shearing stress  $T$  is *proportional* to the rate of shear  $\frac{dv_x}{dy}$ <sup>49</sup>:

$$T = \eta \frac{dv_x}{dy} = \eta \frac{v_x}{Y} \quad (2.3.1)$$

with the shear viscosity  $\eta$  as the constant of proportionality (Figure 2.3.1).

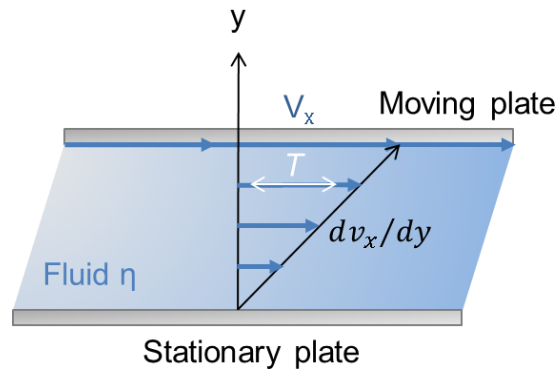


**Figure 2.3.1:** Sketch of a Newtonian fluid between a stationary and a moving plate. The upper plate moves with a velocity  $V_x$  which causes the medium to shear. The shear stress  $T$  is proportional to the rate of shear  $dv_x/dy$  and the viscosity  $\eta$ .

One of the major characteristics of a microfluidic system is the occurrence of laminar flow<sup>15, 50</sup>. In all real flows small disturbances are present. To achieve a stable flow, those disturbances have to decay over time. Otherwise a steady laminar flow will convert into a turbulent flow. A measure for stable laminar flow is the Reynolds number ( $Re$ )<sup>51</sup>. In 1883, Osborne Reynolds found that the transition from laminar to turbulent flow depends on the dimensionless number:

$$Re = \frac{\rho \mathbf{V} L}{\eta} = \frac{\mathbf{V} L}{\nu} \quad (2.3.2)$$

where  $\mathbf{V}$  is the mean flow velocity,  $L$  the characteristic length in the system,  $\eta$  the shear viscosity, and  $\nu = \rho/\eta$  the kinematic viscosity of the medium<sup>52</sup>. For  $Re \ll 1$ , laminar flow occurs<sup>53</sup>.

Furthermore, the Reynolds number describes the ratio between inertial forces per unit area and viscous forces per unit area in a hydrodynamic system<sup>49</sup>. The smaller the Reynolds number the less important are inertial forces that are needed to accelerate mass. At the same time, forces due to viscous shear dominate<sup>54, 38</sup>.

### Equations of change during transport phenomena

Between two laminar fluid streams, transport phenomena can occur. Thereby mass, energy and momentum are exchanged until an equilibrium condition between the fluids is reached. The exchange mechanisms are diffusion for mass, conduction for energy and viscous friction for momentum exchange<sup>49</sup>. In case of isothermal flows of homogenous media, the laws of conservation of mass and momentum are sufficient to describe the equations of change<sup>51</sup>.

#### 2.3.1.1 Equation of continuity (Conservation of mass)

The law of conservation of mass postulates that for an incompressible fluid, the quantity of fluid entering a certain volume has to be balanced by the fluid quantity leaving the volume<sup>49</sup>:

$$\int_S (\rho \mathbf{v}) \cdot \mathbf{n} dS + \frac{\delta}{\delta t} \int_V \rho dV = 0 \quad (2.3.3)$$

where  $\frac{\delta}{\delta t} \int_V \rho dV$  is the time rate of mass increase in a volume  $V$ , and  $\int_S (\rho \mathbf{v}) \cdot \mathbf{n} dS$  is the total outward convection of mass through the volume surface  $S$ . By applying Gauss' theorem to the surface integral, and taking into account that equation 2.3.3 is true for all kinds of volumes, the general continuity equation for nonhomogeneous fluids is<sup>49</sup>:

$$\frac{D\rho}{Dt} + \rho \nabla \cdot \mathbf{v} = 0 \quad (2.3.4)$$

with the Eulerian derivative

$$\frac{D\rho}{Dt} = \frac{\delta\rho}{\delta t} + \mathbf{v} \cdot \nabla \rho \quad (2.3.5)$$

For steady motion  $\frac{\delta\rho}{\delta t} = 0$  and a homogenous fluid the continuity relation is:

$$\nabla \cdot \mathbf{v} = 0 \quad (2.3.6)$$

---

### 2.3.1.2 Equation of linear momentum (Conservation of momentum)

Newton's law of motion postulates that the sum of external forces acting on a stationary fluid element is balanced by the creation of momentum within the fluid particle<sup>51</sup>. On a fluid element, two kinds of external forces can act:

- A long-range *body force*  $\mathbf{F}_{body}$  that is proportional to the size of the fluid element (e.g. gravity force or centrifugal force).
- A short-range *surface force*  $\mathbf{F}_{surface}$ . This force comes into account when distances are on the order of the intermolecular distance (e.g. at the contact area between two fluidic media)<sup>49</sup>.

The total body force acting on a continuous fluid can be written as:

$$\mathbf{F}_{body} = \int \mathbf{B} \rho dV \quad (2.3.7)$$

with the body force per unit mass  $\mathbf{B}$  and the body force on a fluidic particle  $\mathbf{B} \rho dV$ .

The surface force acting on the fluid can be mathematically expressed by

$$\mathbf{F}_{surface} = \mathbf{e}_x \int \int \int \nabla \mathbf{F}_x dV + \mathbf{e}_y \int \int \int \nabla \mathbf{F}_y dV + \mathbf{e}_z \int \int \int \nabla \mathbf{F}_z dV \quad (2.3.8)$$

with  $\mathbf{F}_x, \mathbf{F}_y, \mathbf{F}_z$  being the stresses acting on a fluid element. They can be expressed by the stress tensor  $\boldsymbol{\sigma}$

$$\mathbf{F}_x = \mathbf{e}_x \sigma_{xx} + \mathbf{e}_y \sigma_{xy} + \mathbf{e}_z \sigma_{xz} \quad (2.3.9)$$

$$\mathbf{F}_y = \mathbf{e}_x \sigma_{yx} + \mathbf{e}_y \sigma_{yy} + \mathbf{e}_z \sigma_{yz} \quad (2.3.10)$$

$$\mathbf{F}_z = \mathbf{e}_x \sigma_{zx} + \mathbf{e}_y \sigma_{zy} + \mathbf{e}_z \sigma_{zz} \quad (2.3.11)$$

Due to momentum conservation, the external forces  $\mathbf{F}_{body}$  and  $\mathbf{F}_{surface}$  must be equal to the inertial force  $\mathbf{F}_{inertial}$  acting on the fluid. In an isotropic and homogenous medium, the inertial force acting on a fluidic particle with volume  $\delta V$  and density  $\rho$  is given by



$$\mathbf{F}_{inertial} = -\rho \delta V \frac{D\mathbf{v}}{Dt} \quad (2.3.12)$$

with  $\frac{D}{Dt} = \frac{\delta}{\delta t} + \mathbf{v} \nabla$  being the Stokes operator <sup>51</sup>. The inertial force on the entire continuous fluid is then given by the volume integral

$$\mathbf{F}_{inertial} = - \int \int \int \frac{D\mathbf{v}}{Dt} \rho \delta V \quad (2.3.13)$$

which is true for all volumes.

Considering that  $\mathbf{F}_{inertial} = \mathbf{F}_{body} + \mathbf{F}_{surface}$ , the general equations of fluid motion for a Newtonian fluid are obtained <sup>49</sup>:

$$\rho \frac{D\mathbf{v}}{Dt} = \rho \left( \frac{\delta \mathbf{v}}{\delta t} + \mathbf{v} \nabla \mathbf{v} \right) = \rho \mathbf{B} + \mathbf{e}_x [\nabla F_x] + \mathbf{e}_y [\nabla F_y] + \mathbf{e}_z [\nabla F_z] \quad (2.3.14)$$

They are the Navier-Stokes equations and were derived by Claude Louis Marie Henri Navier in 1827. The non-linear differential equations are nontrivial and simplifications for specific systems are made.

### 2.3.1.3 Simplifications of the Navier-Stokes equations

In the case of a liquid with constant viscosity and constant density, the Navier-Stokes equations can be written as:

$$\rho \left( \frac{\delta \mathbf{v}}{\delta t} + \mathbf{v} \nabla \mathbf{v} \right) = \mathbf{B} - \frac{\nabla \mathbf{p}}{\rho} + \nu \nabla^2 \mathbf{v} \quad (2.3.15)$$

with  $\nu$  being the kinematic viscosity and  $\nabla \mathbf{p}$  being the pressure gradient <sup>49</sup>.

For very small Reynolds numbers, e.g. laminar flow, the transport terms  $\mathbf{v} \frac{\delta \mathbf{v}}{\delta x_i}$  in the Navier-Stokes equations are much smaller than the diffusion terms  $\nu \frac{\delta^2 \mathbf{v}}{\delta x_i^2}$  <sup>49</sup>.

An omission of the inertial terms and conservative external volume forces gives the Stokes equations for steady laminar flow <sup>51</sup>:

---

$$\nabla \mathbf{p} = \eta \nabla^2 \mathbf{v} \quad (2.3.16)$$

Due to the linearity of the Stokes equations, the superposition principle can be applied and many hydrodynamic problems can be solved <sup>49</sup>. Due to the linearity and time-independency of the Stokes equations, laminar flow shows kinematic reversibility. A mixture of masses between two different kind of liquid media is then solely due to diffusion.

Equations 2.3.6 and 2.3.16 are the creeping motion equations. In this context, the viscous drag  $F$  on a sphere with radius  $r$ , moving steadily with velocity  $v$  through a liquid, is

$$F = 6 \pi \eta r v \quad (2.3.17)$$

To solve the fluid motion equations, “no-slip” boundary conditions are applied. They implicate that the fluid velocity on the surface of a moving object is zero <sup>51</sup>. The fluid at the surface of the object moves with the object. The creeping motion equations as well as the no-slip boundary conditions were used to calculate the microfluidic flow field around a trapped bacterial cell.

### Locomotion of microbiological objects at low Reynolds number

The Reynolds number of a bacterium with a characteristic length  $a$  on the micron scale swimming with velocity  $v = 30 \mu\text{m/s}$  through water (viscosity  $\eta = 10^{-3} \text{Ns/m}^2$ ) is about  $10^{-4}$  to  $10^{-5}$  (Figure 2.3.2).

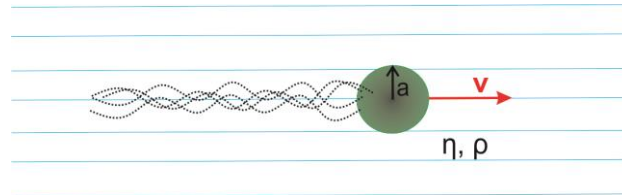


**Figure 2.3.2:** Sketch of a swimming bacterial cell. The cell body is estimated to be spherical with radius  $a$ . By rotating its helical appendages, the bacterium swims with velocity  $\mathbf{v}$  through water with viscosity  $\eta$  and density  $\rho$ .

By rotating helical filaments, a bacterial cell can propel itself through liquid at low Reynolds numbers<sup>55</sup>. In the low Reynolds number regime, inertial forces are negligible and viscous forces dominate<sup>56, 57</sup>. As a consequence, the bacterium immediately stops coasting as soon as it stops rotating its filaments<sup>58</sup>. The forward directed swimming - the drift of the cell - immediately ends and the bacterium undergoes Brownian motion<sup>38</sup>. Furthermore, no reciprocal swimming motion leads to a propelling of an object at low Reynolds numbers. This is exemplified in the “scallop theorem”<sup>54, 59</sup>. The rotation of helical filaments (in case of a bacterial cell) or flexible, oar-like filament motions (in case of a spermatozoa) is therefore a very ingenious locomotion strategy that allows microorganisms to swim<sup>59-61</sup>.

### Chapter summary

The preceding Chapter described the physical properties of low Reynolds number hydrodynamics. At small Reynolds numbers, flow fields are laminar and inertial forces are negligible, whereas viscous forces dominate. For isothermal and homogenous laminar flows, the equation of continuity and the equation of linear momentum are sufficient to characterize transport phenomena. The Navier-Stokes equations can be simplified to the linear Stokes equations for steady laminar flows. The superposition principle facilitates the solution of many hydrodynamic problems. Finally, physical properties of microbiological swimming at low Reynolds number were discussed.

---

## 2.4 Dynamics of bacterial cells

In 1838, locomotion mechanisms of microorganisms were described by the naturalist Christian Gottfried Ehrenberg for the first time<sup>62</sup>. This triggered scientific interest in the nature of bacterial cell movement has steadily increased and new experimental approaches allow scientists to investigate the phenomenon closely. Dark-field microscopes equipped with strong illumination sources and high numerical apertures rendered it possible to optically investigate single bacterial cells<sup>63, 64</sup>. Also fluorescence microscopy has been applied to detect bacteria movement<sup>65, 66</sup>. Optical traps have been used, to spatially confine and manipulate microorganisms like cells or viruses<sup>67</sup>.

In this work, bacterial cell mobility is investigated. Therefore, the dynamics of living microorganisms in the case of peritrichous bacteria are described in this Chapter. In the first part, general bacterial cell structures are explained and an elucidation of filament rotation as bacterial locomotion mechanism is given. In the second part of this Chapter, the bidirectional filament rotation is related to the overall cell movement.

### Bacterial cell structure and filament rotation

Cell organisms can be divided into two major groups, prokaryotes and eukaryotes<sup>58</sup>. Bacterial cells lack intercellular compartments like a membrane enclosed nucleus or mitochondria and belong to the prokaryotes. The body of a bacterium is about 1  $\mu\text{m}$  in diameter and 2  $\mu\text{m}$  in length (Figure 2.4.1)<sup>68</sup>. For locomotion through liquids at low Reynolds number, bacteria rotate thin, helical filaments that are attached to their body<sup>58, 69-71, 89-91</sup>. A bacterial cell can have one propelling filament (monotrichous) or it can have multiple filaments (peritrichous) that bundle and rotate in unison<sup>58, 72-74</sup>.

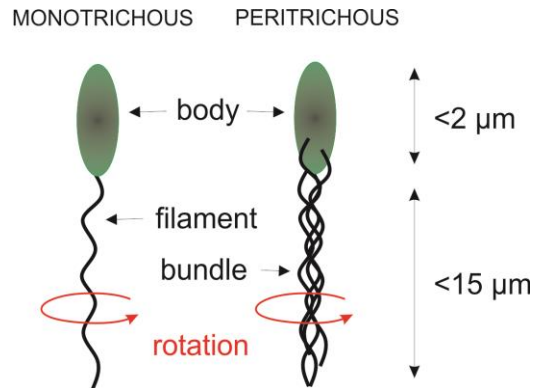


**Figure 2.4.1:** Bacterial cell structures: left: a monotrichous bacterium and right: a peritrichous cell. The monotrichous bacterium has only one propelling filament, whereas a peritrichous bacterial cell has multiple filaments that are synchronized and rotate in a bundle. The body length is about  $2 \mu\text{m}$  and the filaments can reach a length of  $15 \mu\text{m}$ .

One filament is about  $13\text{-}20 \text{ nm}$  in diameter and can reach a length of  $10\text{-}15 \mu\text{m}$ <sup>58, 68</sup>. It consists of the protein flagellin that has a high flexural and torsional stiffness<sup>68, 75</sup>. In case no external forces are present, a filament has the shape of a left-handed helix with a pitch of ca.  $2.5 \mu\text{m}$ <sup>59</sup>. The filament is connected to a flexible rotating hook. The hook in turn is attached to the basal body of the cell. The whole complex of filament, proximal hook and basal body is called flagellum (Figure 2.4.2). The flagellum undergoes rigid rotation with a certain frequency  $\omega$  around its long axis<sup>58, 68</sup>.

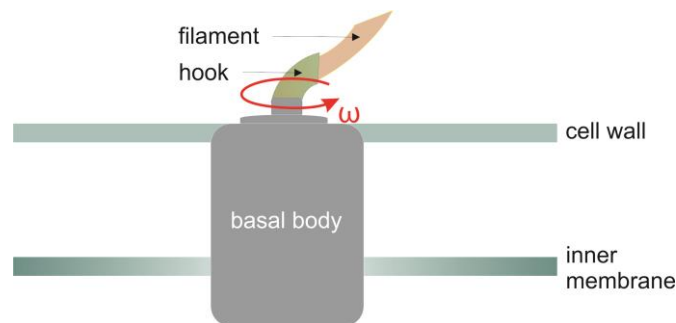


**Figure 2.4.2:** Schematic sketch of a flagellum anchored in the cell body membrane and rotating at frequency  $\omega$ . A flagellum consists of a filament and a flexible hook that is connected to the basal body.

The basal body (Figure 2.4.3) serves as the motor of the flagellum and has a diameter of around  $45\text{-}50 \text{ nm}$ <sup>68</sup>. It consists of five rings and a rod. It can furthermore be divided into a rotor (Figure 2.4.3, red fringe) and a stator complex (Figure 2.4.3, green fringe)<sup>58, 76</sup>.

A proton gradient across the inner membrane allows the rotor to use the proton motive force  $\Delta p$  as its power source<sup>58, 68</sup>.

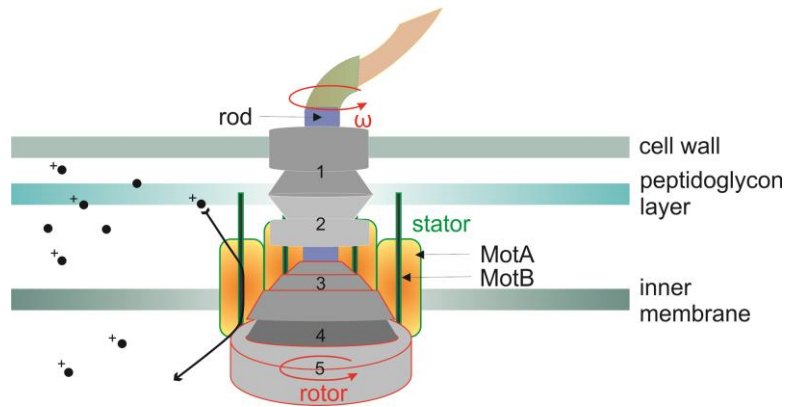


**Figure 2.4.3:** Detailed sketch of the basal body. It consists of a rod and five rings (1-5). The stator uses the proton gradient over the inner membrane to convert chemical into mechanical energy by conformational changes of the MotA and MotB complexes. The latter anchors the stator to the peptidoglycon layer. The rotor rotates at the frequency  $\omega$ .

The stator complex consists of up to eleven single stator units<sup>76</sup>. Each stator unit consists of MotA proteins with two integrated MotB proteins. The MotB proteins anchor the stator unit to the peptidoglycon layer<sup>76</sup>. Each MotB protein contains one aspartic acid. As soon as a proton binds to the aspartic acid, the acid undergoes a conformational change. This conformational change causes a movement of the neighboring MotA proteins. As soon as the proton leaves the aspartic acid in the MotB complex and is transferred to the cytoplasm, the MotA proteins relax into their original states again. The two conformational changes of the whole stator unit provide two power strokes per transferred proton to the rotor system<sup>76</sup>. The proton motive force  $\Delta p$  is determined by the transmembrane electrical difference,  $\Delta \Psi$ , and the transmembrane pH difference,  $\Delta \text{pH}$ . At a temperature of 24 °C and for cells grown at  $\text{pH} = 7$ ,  $\Delta p \cong -170 \text{ mV}$ <sup>68</sup>. The rotation frequency  $\omega$  of the motor is assumed to be proportional to  $\Delta p$ <sup>68</sup>. Instead of protons, some marine bacteria specimens also use sodium ions as a power source for the rotor system<sup>68</sup>.

**Bacterial motility: “Tumbling” and “running” states**

The movement of a particular bacterial specimen depends on the size and shape of the body as well as on the distribution of the flagella over the cell<sup>58, 77, 60</sup>. In the case of a peritrichous flagellated bacterium, the cell body has several appendages and bidirectional motors drive the filaments. This implicates that the filaments can rotate either clockwise (CW) or counter-clockwise (CCW) with the same frequency  $\omega$  (around 100 Hz)<sup>58, 68, 76</sup>.

When the motors rotate in their default CCW direction, the bacterial cell is in its “running” state (Figure 2.4.4 (left)). In this state, all filaments of the cell are synchronized in a helical bundle that rotates CCW to push the bacterium in a certain direction<sup>72, 78</sup>. Bacterial cells like *Escherichia coli* swim with a velocity at the order of 30  $\mu\text{m/s}$ <sup>54, 60</sup>. The bundle rotation  $\omega$  creates a strong torque that needs to be outbalanced by viscous drag due to counter rotation of the cell body  $\Omega$ <sup>38</sup>. For *E. coli* the bundle rotation frequency  $\omega$  is at the order 100 Hz and the cell body rotation frequency  $\Omega$  is at the order of 10 Hz<sup>66</sup>. The thrust generated by flagella rotation to push the bacterium forward is outbalanced by viscous drag due to the translation of the body. The net force on a bacterium, swimming with constant velocity, is therefore zero<sup>38</sup>.

For the bundle formation in the running state, two physical scenarios come into consideration<sup>59</sup>: First, the attraction between single filaments due to hydrodynamic interaction and the swimming of the bacterial cell leave the appendages behind the body<sup>79, 80, 81</sup>. The cell body rotation leads then to a passive bundle formation of the filaments<sup>82</sup>. And second, a hydrodynamic synchronization of nearby flagella leads to a phase locking of their rotational motion<sup>83</sup>.

PERITRICHOUS  
RUNNING STATE    TUMBLING STATE

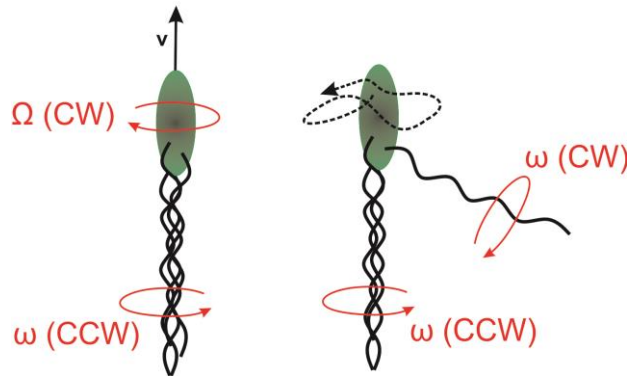


**Figure 2.4.4:** A peritrichous flagellated bacterial cell can be in two distinguished states, the so called running state (left) and the tumbling state (right). In the running state, all flagella are in a bundle, which rotates CCW at the frequency  $\omega$ . The bundle rotation is outbalanced by a counter body rotation  $\Omega$  (CW). In the tumbling state one or more flagella start to rotate CW and leave the bundle. No net torque is transferred to the body anymore and the bacterial cell tumbles in place.

As soon as one or multiple flagella propels reversibly (CW), it leaves the bundle and undergoes a polymorphic transformation from a left- to a right-handed helical shape<sup>59</sup>. The bacterium starts to “tumble” (Figure 2.4.4 (right))<sup>68, 76</sup>. A tumbling of a bacterial cell can be caused by the directional change of a single or several flagella<sup>65</sup>. Under that circumstance, all filaments still rotate, but no net torque is created that would lead to a counter-rotation of the cell body. Furthermore tumbling can be caused when all flagella stop rotating. In both cases, the cell body performs a random movement. Tumbling events of bacterial cells are observed at a broad time scale - starting from several hundred milliseconds, to the point when cells are exclusively tumbling<sup>54, 66</sup>. The running and tumbling behavior can be different for swarm cells<sup>84</sup>. The switch between the running and tumbling state is a consequence of the bacterium’s reaction to environmental chemical stimuli, which is called chemotaxis.

Chemotaxis is essential for every living microorganism to be able to sense and respond to changes in its environment, for example variations in temperature, chemical concentrations, oxygen content or light intensity. Bacterial cells can sense changes in the chemical attractant concentration and respond with a certain movement. This process is called chemotaxis<sup>63, 85, 86</sup>. A bacterial cell has two possibilities to adapt its movement to chemical stimuli: it can switch from the running state (CCW flagella rotation) to the



tumbling state (CW flagella rotation) or vice versa. That means the bacterium can switch from a forward directed movement to a state in which it tumbles in place.

The switch between CCW and CW rotation of the flagella is elicited by the binding of the phosphorylated protein CheY (CheY-P) to the flagellar switch protein FliM. As soon as the chemotactic signaling protein CheY-P binds, the motor will run in CW direction. The bacterium is in a tumbling state<sup>68, 76</sup>. The cell body performs a Brownian movement which allows the bacterium to reorient and change the swimming direction. CheY is phosphorylated at the chemo receptors of the bacterium near the surface. Chemical attractants (e.g., sugars or amino acids) in the surrounding medium also bind to those sensory receptors<sup>68</sup>. If the bacterial cell finds itself in a region with a higher chemo attractant concentration, the phosphorylation of CheY is depressed and the bacterium likely stay in its running state<sup>68, 76</sup>. Accordingly, the bacterial cell swims into the direction of highest attractant concentration<sup>66</sup>. In general, bacteria move upwards a spatial gradient of chemo attractants or downwards repellent gradients<sup>76, 86, 76</sup>.

The switch between the running and tumbling state leads to an overall random movement of the bacterial cell (Figure 2.4.5). At low Reynolds numbers, diffusion is the dominant transport mechanism of nutrients in the liquid<sup>54</sup>. To be able to find places with higher local chemo attractant concentration and to be able to “sample” the medium, the swimming bacterial cell has to outrun diffusion. This distance can be estimated with the diffusion coefficient divided by the swimming velocity and is at the order of 30  $\mu\text{m}$  (Figure 2.4.5)<sup>54</sup>. In the runs, the bacterium is subjected to rotational diffusion that arises from thermal energy (analogous to the translational diffusion, explained in Chapter 2.2.1.1). Rotational diffusion influences the straight movement of the bacterial cell<sup>38</sup>. Assuming that the bacterium body is a sphere, the 2D mean square angular deviation in time  $t$  is

$$\langle \theta^2 \rangle = 4 D_r t \quad (2.4.1)$$

with the rotational diffusion coefficient

$$D_r = \frac{kT}{8\pi\eta a^3} \quad (2.4.2)$$

---

$a$  represents the cell body radius,  $\eta$  the viscosity,  $k$  the Boltzmann constant and  $T$  the temperature. Typical deviations during straight swimming are  $30^\circ$  in  $1\text{ s}$  <sup>38</sup>.

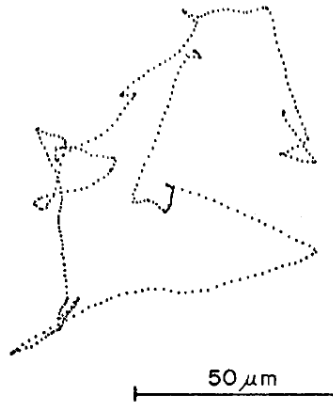


**Figure 2.4.5:** Track of randomized bacterial motility for *E. coli* as a consequence of chemotaxis. Two dots are 0.1 s apart from each other. The running and tumbling states can be clearly distinguished. (Taken from 54).

### Chapter summary

The dynamic behavior of peritrichous bacterial cells was described. Therefore, a detailed description of bacterial flagella and their rotation mechanism was given. The bidirectional rotation possibility of single filaments was related to flagella bundling and the overall cell body movement. It can be either “running” or “tumbling”. Tumbling events of bacterial cells are observed at a broad time scale -starting from several hundred milliseconds, to the point when cells are exclusively tumbling. Environmental chemical stimuli are the reason for the motility behavior of a bacterial cell.

### **3. Methods and Materials**

*This Chapter describes the experimental techniques used in this work and lists the materials that were needed to perform the experiments. The aim of all experiments is the measurement of the microfluidic flow generated by an artificial or living microobject with very high resolution. This is realized by an optically confined particle which is used as optofluidic sensor. The first section of this Chapter describes the integration of several optical tweezers at different wavelengths into a dark-field microscope. The optical setup was constructed for this thesis and in combination with a high speed camera it was possible to achieve a very precise detection of the performed experiments. In the second part, the chemical preparation of the bacteria cells that served as living sources of flow is described. For the measurement of the optical density of the bacteria cultures an UV/Vis spectrometer was used. In the next part, the preparation of the microscope glass slides is presented briefly and the particles used as microfluidic flow detectors are characterized. The last section contains information about single particle-tracking and data analysis. Fast Fourier transformation of the time-dependent  $x$ - and  $y$ -displacement of the flow source and of the optofluidic sensor is the fundamental concept of data evaluation.*

---

### 3.1 Dark-field microscopy equipped with optical tweezers

One of the unique advantages of dark-field microscopy is that it allows for a visualization of noble metal nanoparticles with size dimensions below the optical diffraction limit. This is possible, because these particles possess scattering cross sections that exceed their geometric cross sections multiple times<sup>87, 88</sup>. With dark-field microscopy it is also possible to achieve a contrast-rich, high resolution imaging of small living microorganisms<sup>64</sup>. Dark-field microscopy equipped with optical tweezers provides therefore numerous experimental possibilities: Controlled plasmonic heating of gold nanoparticles in an optical trap, for example, has been used to fine tune the kinetics of DNA hybridization<sup>89</sup>. Rayleigh scattering of silver nanoparticles in an optical tweezer was investigated to explain the correlation between plasmonic coupling in an optical trap and trapping stability<sup>90</sup>. Furthermore, spatiotemporal tracking of an optically trapped gold nanoparticle allowed for a ultrasensitive detection of microfluidic and acoustic waves in water<sup>13</sup>.

#### 3.1.1.1 Dark-field microscopy

For dark-field microscopy, the illumination light has to enter a special condenser (Figure 3.1.1). In the dark-field condenser, the light passes an annular light stop and is then focused by an integrated lens system under a certain angle to the substrate. The angle under which the light is focused with respect to the substrate is determined by the numerical aperture (NA) of the lens system:

$$NA = n_m \sin(\alpha) \quad (3.1.1)$$

$n_m$  is the refractive index of the surrounding medium and  $\alpha$  represents the half-angle of the focused cone of light. For dark-field illumination, it is necessary that the NA of the used condenser is greater than the NA of the objective used for observation:

$$NA_{condenser} > NA_{objective} \quad (3.1.2)$$

This condition ensures that only light scattered by the observed specimen is collected by the objective. If this requirement is fulfilled, a bright, contrast-rich image of the specimen on a dark background appears.

In this work, an up-right microscope (Zeiss Axio Scope.A1) was used for the optical detection of the measurements (Figure 3.3.1). A 100 W halogen lamp covering the visible spectrum served as illumination source. An oil immersion condenser with high NA (NA=1.2, Zeiss) was used. An oil droplet on top of the condenser lens was brought into contact with the bottom of the microscope slide. Since the refractive index of oil  $n_{oil} = 1.518$  matches the refractive index of glass, two refractive surfaces are eliminated. The microscopy slide was mounted onto a micrometer stage that allowed a precise positioning of the sample. For the optical magnification of the observed specimen, a 10x/NA=0.2 (Zeiss) air objective as well as water dipping objectives with 63x/NA=1.0 and 100x/NA=1.0 (Zeiss) were used. Beside the direct observation through the ocular of the microscope, the scattered light could be detected by a digital camera (Canon EOS 550D SLR) or a high speed 12 bit CMOS camera (PCO.dimax). The high speed camera provided a frame rate of 4502 fps with a 1008x1000 pixel resolution and a frame rate of 2470 fps with a 1920x1080 pixel resolution (full HD). Furthermore, a diffraction grating spectrometer (Acton SP2500, Princeton Instruments) connected to a liquid nitrogen cooled CCD camera (PyLoN, Princeton Instruments) could be used for scattered light spectroscopy. The spectrometer was equipped with three different gratings (150 l/mm BLZ<sup>5</sup>=800 nm, 300 l/mm BLZ=500 nm and 1200 l/mm BLZ=750 nm) to be able to perform broad spectral range measurements as well as high resolution measurements.

---

<sup>5</sup> BLZ: blaze wavelength of the grating;

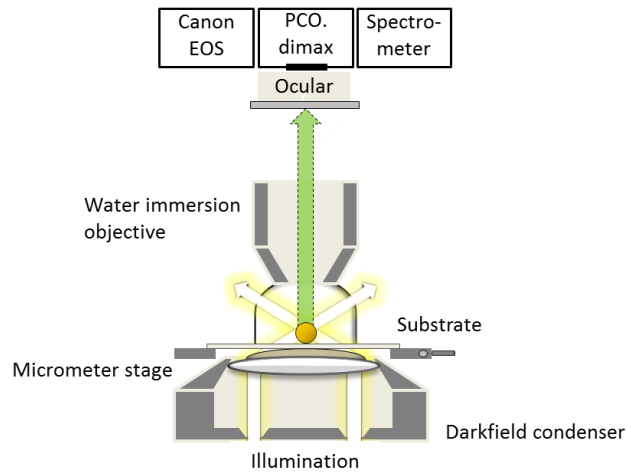


**Figure 3.1.1:** Sketch of a dark-field microscope. Due to the dark-field condenser, the direct illumination light does not enter the objective. Only light scattered by the sample is collected and can be detected by the cameras or the spectrometer. A micrometer stage allowed a very precise positioning of the substrate.

The combination of a dark-field configuration with an optical tweezer has some challenge: A strongly focused laser beam is required for a stable 3D optical trap, since the physical cause of such a trap lies in the gradient of the optical field intensity. Tight focusing of a laser beam is usually achieved by high NA objectives with  $NA=1.3-1.4$ <sup>90</sup>. The highest NA of commercially available dark-field oil condensers is 1.2 though. Since  $NA_{condenser} > NA_{objective}$ , an approach to overcome this hindrance has to be found. By using a beam expander, a sufficient laser focusing for a stable, 3D trap was achieved with a water dipping objective ( $NA=1.0$ ). The especially for this thesis constructed setup allowed an integration of several optical tweezers at different wavelengths.

### 3.1.1.2 Optical tweezers at 1064 nm wavelength

A continuous wave, diode-pumped solid-state laser from Cobolt Rumba with a wavelength  $\lambda = 1064$  nm (TEM<sub>00</sub>) and maximal output power of 2 W was used to set up an infrared optical tweezer. The laser provides a high level of stability and is therefore suitable for a stable optical trap. To slightly overfill the back aperture of the used objective (water dipping, 100x/NA=1 or 63x/NA=1), the initial beam was expanded by a beam-expander (2-8x, Edmund Optics) (Figure 3.1.2 (a)). A beam splitter in the microscope was used to focus the trapping beam to the stage of the dark-field microscope. To compensate the chromatic aberration of the 1064 nm beam when focused by the objective, a lens (plano convex, focal length  $f = 997$  mm) was built in the beam path in front of the microscope (Figure 3.1.2 (a)). The trapping beam could be coupled into the microscope either from the left or the right side. Alternatively to a single optical tweezer, a dual beam trap configuration could be used (Figure 3.1.2 (b)). Therefore, the expanded initial laser beam was split into two beams, using a polarizing beam splitter on which a lambda-half plate (PBS 1) was mounted. The power ratio between the beams was defined as 1 to 1. Both beams were recombined using a second polarizing beam splitter (PBS 2). Two mirrors (M3 and M4) allowed a precise steering of one of the two beams with respect to the other. Finally, the beams were focused through the objective. Two optical traps separated at a predefined distance could be used in the experiment. A notch filter blocking light at 1064 nm (StopLine 532/1064, Semrock) was implemented to avoid a detection of the laser beam.

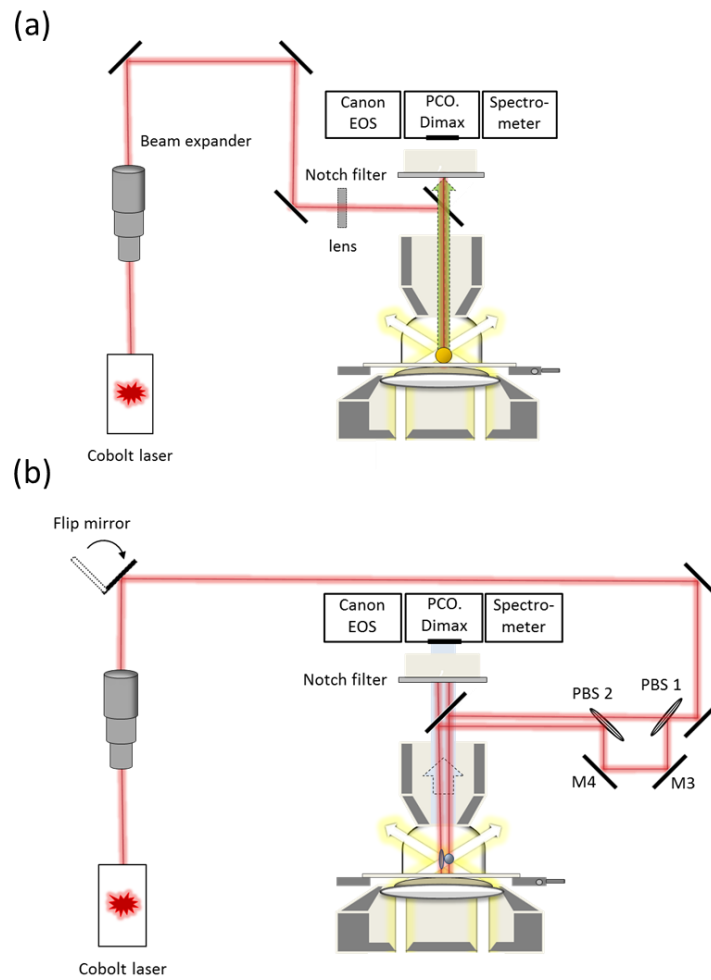


**Figure 3.1.2:** A 1064 nm laser beam could be coupled into the microscope from the left side (a) or from the right side (b). In the second case, the expanded initial laser beam was split into two beams using polarizing beam splitters (PB 1 and PB 2). Two mirrors (M3 and M4) allowed a precise steering of one of the two beams with respect to the other.



## 3.1.1.3 Optical tweezers at 532 nm wavelength

The beam of a continuous-wave laser operating at 532 nm ( $TEM_{00}$ , Opus 532, purchased from Laser Quantum) with a maximal output power of 3 W was first expanded by a home-built Keplerian telescope (Figure 3.1.3). For the telescope, two plano convex lenses (L1 = objective lens and L2 = image lens) purchased from Thorlabs were set up with a distance matching the focal lengths. The objective lens had a focal length of  $f = 49.8$  mm, the focal length of the image lens was  $f = 149.5$  mm. The expanded beam was split into two beams of equal power by a non-polarizing cube beam splitter (BS1) (Thorlabs). The beams were recombined by a second cube beam splitter (BS2) and had then a defined distance from each other. An optical chopper system (consisting of chopper wheel and controller) was used to block one of the trapping beams and let the other pass with a certain frequency. A notch filter blocking light at 532 nm (StopLine 532/1064, Semrock) was mounted into the microscope to prevent a detection of the laser beams. Additionally to the two optical traps at 532 nm, a 1064 nm laser beam could be coupled simultaneously into the microscope (cp. Chapter 3.1.1.2)

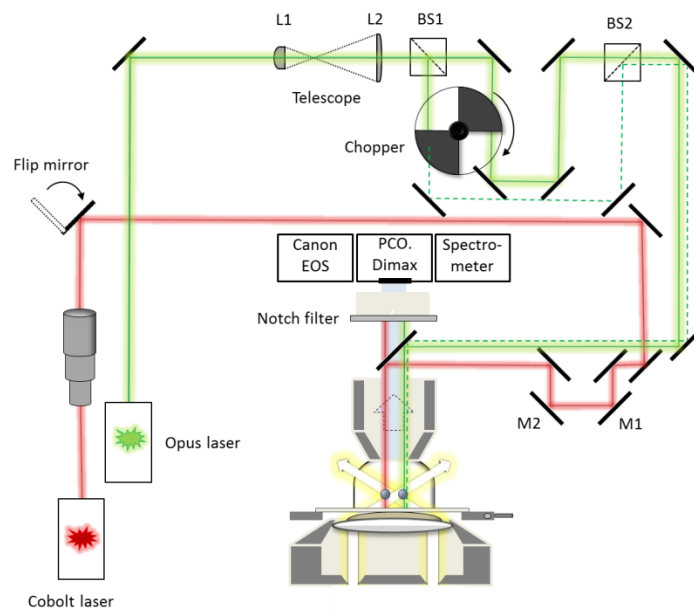


**Figure 3.1.3:** The expanded 532 nm beam was split into two beams by two cube beam splitters (BS1 and BS2). A chopper system allowed a blocking of one beam and let the other pass at a certain frequency. Furthermore, a 1064 nm laser beam could be coupled simultaneously into the microscope.

---

### 3.2 Bacterial cell preparation

As microbiological samples, two different strains of *Bacillus subtilis* were used. The first strain was *BM77*, a flagellated bacterium<sup>91</sup>. The second strain was *BD3458*, a non-flagellated bacterium<sup>92</sup>. Both *B. subtilis* strains are derivatives from the *BD630* strain which has the genotype *his leu met*<sup>6</sup><sup>91</sup>. *BM77* was created by transforming *pUB110::T7T3::ComS*<sup>7</sup><sup>93</sup> into *BD2711*<sup>91, 94, 95</sup>. The genotype of *BM77* is *his leu met comK*<sup>8</sup>-*gfp* (*CBL*, *cat*<sup>9</sup>), *multicopy comS* (*kan*<sup>10</sup>)<sup>91</sup>. The second strain *BD3458* is also a derivative of *BD630*<sup>92</sup> with the genotype *his leu met rok*<sup>11</sup>- (*spc*<sup>12</sup>), *hag*<sup>13</sup>- (*erm*<sup>14</sup>).

The viability of *B. subtilis* depends on its environmental conditions. A high motility of the bacillus is essential for the experiments performed in this work. The protocol for bacterial cell preparation that was used in this work is based on a publication of Ordal et al.<sup>96, 97</sup>:

Both bacteria strains (*BM77* and *BD3458*) were grown in lysogenize broth (LB) medium overnight. In case of the *hag* strain (*BD3458*), the macrolide antibiotic erythromycin was added to the LB medium with an end mass concentration  $\rho_{end} = 5 \frac{\mu g}{ml}$ . The next day, the bacterial solutions were diluted 1:50 with a mineral-salt-solution consisting of 50 mM potassium-phosphate-buffer (pH 7.0), 0.12 mM  $MgCl_2$ , 1 mM  $(NH_4)_2SO_4$ , 0.14 mM  $CaCl_2$ , 0.01 mM  $MnCl_2$ , 20 mM D-sorbitol, 0.3 mM methionine, 0.3 mM leucine and 0.3 mM histidine. For the potassium-phosphate-buffer (pH 7.0), 122 ml of 0.1 M  $K_2HPO_4$  in  $ddH_2O$  were mixed with 78 ml of 0.1 M  $KH_2PO_4$  in  $ddH_2O$ . Afterwards, the bacterial solutions were incubated at 37 °C and 300 rpm until they reached an optical density of  $OD_{600}=0.3$ . At this value of the optical density, the exponential phase of bacterial growth begins which is the optimal phase for harvesting the cells. To determine the optical density, the absorbance ( $\lambda = 600 \text{ nm}$ ) of 100  $\mu l$  bacterial solution was measured with a

---

<sup>6</sup> *his leu met*: histidine, leucine and methionine resistance respectively;

<sup>7</sup> *comS*: releases *comK* for autostimulation;

<sup>8</sup> *comK*: competence transcription factor of *B. subtilis*;

<sup>9</sup> *cat*: chloramphenicol resistance;

<sup>10</sup> *kan*: kanamycin resistance;

<sup>11</sup> *rok*: repressor protein;

<sup>12</sup> *spc*: spectinomycin resistance;

<sup>13</sup> *hag*: flagellin protein, ~20,000 subunits create one flagellum;

<sup>14</sup> *erm*: erythromycin resistance;

spectrophotometer every hour for each bacterial strain (see Chapter: 3.3). Averagely, the optical density  $OD_{600}=0.3$  was reached after three hours for the BM77 strain and after two hours for the BD3458 strain. As soon as the optical density was reached, 5 mM (end concentration) potassium-phosphate-buffer (pH 7.0) and 0.05% (end concentration) glycerin were added to the bacterial solutions, and the bacteria were again incubated at 37 °C and 300 rpm for 15 min. In the next step, the cells were washed with chemotaxis medium<sup>96,97</sup> consisting of 10mM potassium-phosphate-buffer (pH 7.0), 0.14 mM  $CaCl_2$ , 0.3 mM  $(NH_4)_2SO_4$ , 0.1 mM EDTA (pH ca. 5.0), 5 mM sodium lactate, 0.05% glycerol and ddH<sub>2</sub>O. Afterwards they were subsequently separated into 90 aliquots. After adding 10% (end concentration) glycerin to each aliquot, they were frozen in liquid nitrogen (T = -196 °C) and stored in the freezer at -80 °C. At this temperature, the bacterial strains can be preserved for several months.

For each measurement, one aliquot was defrosted at room temperature. The bacterial solution was diluted with chemotaxis medium in a way that just one or two bacteria could be seen simultaneously in the field of view of a water dipping 100x/NA=1.0 dark-field objective.

---

### 3.3 UV/Vis spectrophotometer

The OD of each bacterial culture was measured with a double-beam UV/Vis spectrophotometer (Lambda EZ201, Perkin Elmer). As excitation source, it combines the spectrum of a deuterium and tungsten halogen light source and provides therefore a spectral range from 190 nm to 1,100 nm. By a Czerny-Turner monochromator, a selective excitation wavelength is chosen. A beam splitter after the monochromator splits the incoming light into two parts to simultaneously measure a test and a reference sample (baseline). After the beams passed through the media they are detected by photodiodes, and their light intensity is measured.

The optical density or absorbance ( $A$ ) of a medium in the beam path can be expressed by the Beer–Lambert–Bouguer law

$$A(\lambda) = -\lg T(\lambda) = -\lg \frac{I(\lambda)}{I_0(\lambda)} = e^{-\sigma l N} \quad (3.3.1)$$

with  $T$  being the transmittance of the tested medium,  $I$  the light intensity after the test sample, and  $I_0$  the light intensity after the reference sample. The absorbance can also be expressed by the exponential function of the negative product of the absorption cross section  $\sigma$  of a single absorber, the light path length  $l$  and the density of absorbers  $N$  in the test sample.

To measure the absorbance of a bacterial cell solution, the excitation wavelength was set to  $\lambda = 600 \text{ nm}$ . A baseline with solely LB medium was taken. Therefore 100  $\mu\text{l}$  of LB medium were pipetted into a quartz glass cuvette with a light path length of  $l=10 \text{ mm}$  (Hellma Analytics) and its OD was measured. Likewise, the absorbance of 100  $\mu\text{l}$  bacterial cell solution was measured afterwards. Finally, the baseline of the LB medium was subtracted from the OD of the bacterial cell solution.

### **3.4 Preparation of microscope glass slides**

Square microscopical cover glasses (24x24 mm<sup>2</sup>, thickness: 0.19-0.23 mm) were purchased from Rudibert Ernst Böll e.k. Before the measurement, they were successively sonicated in isopropyl alcohol and ddH<sub>2</sub>O (Milli-Q water) for 15 min each. To wipe out liquid residues on the cover slips, they were dried with a nitrogen gun after the cleaning. Finally, the cover glasses were stored in wafer holders.

### **3.5 Microfluidic flow detectors**

As microfluidic flow detectors, either gold nanoparticles or silicon dioxide microparticles were used. The citrate stabilized gold particles had a diameter of 60 nm. The stock solution was purchased from BBInternational Solutions. For the experiment, the initial gold particle solution ( $2.60 \times 10^{10}$  particles/ml) was diluted with ddH<sub>2</sub>O in a way that just one or two particles could simultaneously be seen in the field of view of a 100x/NA=1.0 water dipping objective. The silicon dioxide spheres had a diameter of 1.76 or 1.3  $\mu\text{m}$  and were purchased from micro particles GmbH, Forschungs- und Entwicklungslaboratorien. They possess a hydrophilic anionic surface and their refractive index is  $n = 1.45$ . Depending on the performed experiment, the initial silicon dioxide particle concentration was either diluted with ddH<sub>2</sub>O or with chemotaxis medium. A final concentration was chosen that just one or two silica particles could be seen simultaneously in the field of view of the 100x water dipping objective.

---

### 3.6 Single particle-tracking and data analysis

For data analysis, video files of the performed experiments were recorded. Therefore, two different cameras were available: either a color camera (Canon EOS 550D SLR) or a high speed camera (PCO.dimax). The Nyquist–Shannon sampling theorem describes the inevitable correlation between video sampling rate  $f_s$  and bandlimit frequency  $f_{max}$  :

$$f_{max} \leq \frac{f_s}{2} \quad (3.6.1)$$

The minimum sampling frequency is  $f_{Nyquist} = \frac{f_s}{2}$  and called the Nyquist frequency<sup>45, 98, 99</sup>. Table 3.6.1 contains the frame rates that were chosen in the recorded videos:

	Sampling rate	Band limit
Canon EOS	$f_s = 60 \text{ Hz}$	$f_{max} = 30 \text{ Hz}$
PCO.dimax	$f_s = 500 \text{ Hz}$	$f_{max} = 250 \text{ Hz}$
	$f_s = 1000 \text{ Hz}$	$f_{max} = 500 \text{ Hz}$

Table 3.6.1: Sampling rate and band limit frequency for the two different cameras: Canon EOS and PCO.dimax.

In the captured video files, the spatiotemporal displacement of an optically trapped particle was analyzed. This was done with the particle-tracking software “video spot tracker” (freeware provided by CISMM: Computer Integrated Systems for Microscopy and Manipulation). While operating the program, the “symmetric” tracker was chosen which guaranties a proper tracking of the particle center, even if the particle intensity profile is slightly changing over time. As described by CISMM, this tracker operates by locating the minimum variance in concentric rings around the bead center. It sums the variance in circles of radius 1, 2, 3, ... up to the radius setting and divides each circle’s radius by its circumference to provide even weights for each ring. Furthermore, the program allows single and multiple particle-tracking in a captured video file.

The program identifies the position-coordinates of the detector center in each frame of the video file in two dimensions. It reads out  $x(t_n)$  and  $y(t_n)$  for the particle position with  $n = 1 \dots N_0$  and  $N_0$  being the total amount of frames in the video. The program uses the particle center position in the first frame  $x(t_1), y(t_1)$  as reference point for the spatiotemporal development.

The time series of the detector position  $x(t_n)$  and  $y(t_n)$  were analyzed separately. For both dimensions, the time series was projected from real to Fourier space by a one-sided fast Fourier analysis ( $FFT_x$  and  $FFT_y$ ). The FFT operation is a special form of discrete Fourier transformation (DFT) and reduces the amount of necessary computations by an order of magnitude<sup>98, 100</sup>. The discrete FFT is mathematically described by:

$$F_n = \sum_{k=1}^{N_0} f_k e^{-in\Omega_0(k-1)} \quad (3.6.2)$$

with  $\Omega_0 = \frac{2\pi}{N_0}$  and  $N_0$  being the amount of discrete sample values<sup>98</sup>. The scaling of the conjugate units after FFT has a step distance of

$$\Delta f_{FFT} = \frac{1}{N_0 \cdot \Delta t_{input}} \quad (3.6.3)$$

with  $\Delta t_{input}$  being the step distance of the input signal, for example,  $\Delta t_{input} = 1 \text{ ms}$  for a video sampling rate  $f_s = 1000 \text{ Hz}$ . In the frequency spectra, the Fourier amplitudes  $A(FFT_x)$  and  $A(FFT_y)$  were observed. To achieve the best signal to noise ratio in Fourier space, the total amplitude  $A(FFT)$  was calculated as:

$$A(FFT) = \sqrt{A(FFT_x)^2 + A(FFT_y)^2} \quad \text{with} \quad (3.6.4)$$

$$A(FFT_i) = 2 \sqrt{\text{Re}_i^2 + \text{Im}_i^2} / N_0 \quad (3.6.5)$$

and  $i$  being the x- or y-direction,  $N_0$  being the amount of frames, and  $Re$  and  $Im$  being the real and imaginary part of the FFT.





## 4. Optical driving and sensing of helical and biological microobjects

*The dynamic behavior of bacterial cells is of great interest for microbiology and nanomedicine. Research on the physical properties as well as locomotion strategies of living microorganisms to investigate their physical properties as well as their locomotion strategies began already more than one hundred years ago. However, a single filament has a diameter of just 20 nm and the flagella bundle is hard to resolve under dark-field illumination. This hampers a detailed and direct investigation of the dynamic behavior of bacterial appendages<sup>64, 63</sup>. Experimental remedial measures for this problem have been established. For example, reducing the speed of motion of the investigated bacterium<sup>101</sup> or labeling of the filaments with fluorescent dyes<sup>65, 66, 84</sup> or nanoparticles<sup>102</sup>. The main goal of this work is to find an alternative approach to the direct observation of a bacterial cell for the analysis of its motility. This overcomes the hindrance of fluorescent labeling or any other kind of cell modulation. The underlying idea is the measurement of the microfluidic flow generated by an optically confined bacterium by means of a sensor particle that is trapped in a second tweezer in the close vicinity. In this work, for the first time, it is demonstrated how the “nanoeear” approach can be extended and applied to study the microflow generated by a bacterium that possesses its own dynamics at the nanoscale. To this aim, intermediate targets had to be understood first. Among them are the application of dielectric microparticles instead of plasmonic nanoparticles as optofluidic sensors for oscillatory flows and sensing the flow of an optically driven microhelix that was used to model the mechanical and dynamical properties of a bacterial cell.*

---

#### **4.1 Application of a plasmonic nanoparticle as optofluidic sensor for oscillations generated by a living microorganism**

Optical tweezers to spatially confine noble metal nanoparticles have been established for the first time in 1994 by Svoboda and Block<sup>103</sup>. Since then their field of application has expanded considerably. As an example, their high sensitivity is eminently suitable to measure or apply tiny forces between molecules down to the piconewton range<sup>2, 7, 103</sup>. The development of optical traps with single nanoparticles, ten years later, rendered it possible to investigate their single particle optical properties closely, leading to the development of a precise understanding of the trapping mechanism, the forces acting on the particles and its motion within the trap<sup>6</sup>. Moreover, the wavelength range for a successful optical trapping of metallic nanoparticles has been investigated and expanded<sup>7</sup>. The idea to use a single gold nanoparticle in an optical trap as a microfluidic flow sensor was realized by Ohlinger et al. in 2012<sup>13</sup>: Here, an optically confined gold nanoparticle was used to readout microfluidic and acoustic oscillations in the surrounding. It has been observed that the Brownian motion of the trapped particle is disturbed, depending on the frequency, distance and intensity of the applied oscillations. While in this primary work the oscillations were artificially generated in the surrounding medium, in this Chapter, the extension to real biological samples is demonstrated. I will show how a single gold sphere is used as an optofluidic nanosensor to detect for the first time the microfluidic oscillations generated by a microbiological sample. To realize this task a freely swimming larva of Copepods, called Nauplius, served as living source of flow generated through the rhythmic strokes of its antennae. The thus created microfluidic flow was detected by optically tracking of a gold nanoparticle confined in the potential of an optical tweezer. The extracted frequencies from the motion of the gold nanoparticle in the optical trap were in good agreement with those obtained through a direct observation of their motion. Thus, our approach delivers a tool to detect the microfluidic oscillations produced by living animals in the vicinity of the optical trap and enables a non-invasive analysis of their motion.

In the first part of this Chapter, the theoretical background of the optical forces acting on a plasmonic nanosensor is described. In the second part, the microbiological source of fluidic oscillations is characterized by its direct observation. In the main part, the

movement of the living organism is analyzed by optical tracking of the plasmonic flow detector. Finally, the Chapter is concluded and future perspectives as well as applications are discussed. This Chapter is based on my work published in *J. Vis. Exp.*<sup>104</sup>.

### Optical forces on a plasmonic nanoparticle

Small particles that are immersed in aqueous solution are subjected to Brownian motion (cp. Chapter: Diffusion). Once trapped in an optical tweezer, the particle is prevented from long-term diffusion and its movement is dominated by directed diffusion within the harmonic trapping potential (cp. Chapter: Diffusion with drift for a spherical particle). The harmonic potential is a consequence of the optical force distribution within the tweezer (cp. Chapter: Optical forces on a small particle). The total electromagnetic force acting on a gold nanoparticle in an optical trap can be split into two components: The gradient force  $\mathbf{F}(\mathbf{r})_{grad}$  (equation 2.1.16) and the scattering force  $\mathbf{F}(\mathbf{r})_{scat}$  (equation 2.1.17). The gradient force is conservative and depends on the real part of the complex polarizability of the gold nanoparticle. It acts for a positive real part of the polarizability along the field intensity gradient toward the focal point of the focused trapping beam. A strong gradient force is achieved by a highly focused trapping beam. The scattering force is dissipative and depends on the imaginary part of the complex polarizability. The scattering force points along the electromagnetic wave propagation. Changing the ratio between the real and imaginary part of the polarizability of the gold nanoparticle (e.g., the ratio between the gradient and the scattering force) can thus determine the final trap stiffness  $\kappa$ <sup>31</sup> (cp. Chapter: 2.1.1.3). The ratio can be tuned by varying the trapping laser wavelength. A stable trapping of a gold nanoparticle is thus strongly dependent on the wavelength of the trapping laser<sup>2, 7, 103</sup>. For a stable 3D trapping, the gradient force has to be greater than the scattering force plus thermal forces acting on the particle (see Chapter: Diffusion).

In the experiments presented in this Chapter, a trapping wavelength of  $\lambda = 1064$  nm was chosen. And a gold nanoparticles with a diameter of  $D = 60$  nm. The trapping wavelength was far red-shifted from the plasmon resonance of the gold sphere at  $\lambda \sim 530$  nm. This implicated that the optical gradient force was dominant and the scattering force which originates from momentum transfer of scattered and absorbed photons was

---

minimal. At a wavelength close to the particle resonance, the scattering of becomes strong and the scattering force dominant. The gold nanoparticle is pushed beyond the focal plane and not trapped in 3D<sup>10, 105</sup>.

For an illustration of the 3D confinement of the gold nanoparticle in the optical trap, the optical forces acting on the sphere suspended in water were simulated numerically (Figure 4.1.1). The numerical aperture of the objective was NA = 1.0 and the power of the trapping laser  $P = 100$  mW. Since the particle is within the Rayleigh regime, the condition for the electrostatic dipole approximation for the polarization of the particle (equation 2.1.1) is sufficiently fulfilled and retardation effects could be neglected. Instead of considering a planar incident wave, a paraxial Gaussian beam focused by a lens as proposed by Agayan et al.<sup>31</sup> was considered. The expressions for the gradient and scattering force in cylindrical coordinates are<sup>31, 106</sup>:

$$\langle \mathbf{F}_{grad} \rangle_z = -\frac{\varepsilon_0}{\pi} \alpha' |\mathbf{E}_0|^2 z \frac{w_0^4}{z_0^2} \left[ \frac{1}{w^4(z)} - \frac{2r^2}{w^6(z)} \right] \exp\left(-\frac{2r^2}{w^2(z)}\right) \quad (4.1.1)$$

$$\langle \mathbf{F}_{grad} \rangle_r = -\frac{2\varepsilon_0}{\pi} \alpha' |\mathbf{E}_0|^2 r \frac{w_0^2}{w^4(z)} \exp\left(-\frac{2r^2}{w^2(z)}\right) \quad (4.1.2)$$

$$\langle \mathbf{F}_{scat} \rangle_z = \frac{\varepsilon_0}{\pi} \alpha'' |\mathbf{E}_0|^2 \frac{w_0^2}{w^2(z)} \left\{ k_m \left[ 1 - \frac{r^2(z^2 - z_0^2)}{2(z^2 + z_0^2)^2} \right] - \frac{w_0^2}{z_0 w^2(z)} \right\} \exp\left(-\frac{2r^2}{w^2(z)}\right) \quad (4.1.3)$$

$$\langle \mathbf{F}_{scat} \rangle_r = \frac{\varepsilon_0}{\pi} \alpha'' |\mathbf{E}_0|^2 \frac{w_0^2}{w^2(z)} \frac{k_m r}{R(z)} \exp\left(-\frac{2r^2}{w^2(z)}\right) \quad (4.1.4)$$

with  $w^2(z) = w_0^2 \left[ 1 + \left(\frac{z}{z_0}\right)^2 \right]$ ,  $R(z) = z \left[ 1 + \frac{z_0^2}{z^2} \right]$ ,  $w_0$  being the beam radius in the focal plane and  $z_0$  being the focus position in z-direction along the beam axis.

The calculated distribution of the gradient and scattering force as well as the total optical force that keeps the particle confined in the trap is shown in Figure 4.1.1. It is important to mention that for a tightly focused beam and a high numerical aperture of the objective (as it is the case here) the simulation model reveals some uncertainties since it is based on a loosely focused Gaussian beam. Nevertheless, the simulation clearly demonstrates that

under the chosen conditions the total force (Figure 4.1.1) favors a particle trapping close to the focal point.

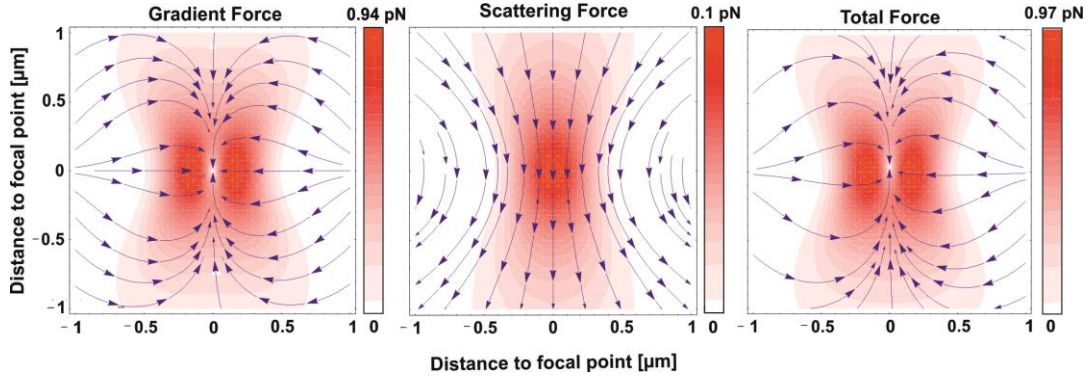


**Figure 4.1.1:** Simulation of the optical forces acting on a 60 nm gold nanoparticle in an optical trap with a wavelength of  $\lambda = 1064$  nm and a power of  $P = 100$  mW. The gradient force points into the direction of highest field intensity, whereas the scattering force points toward the beam propagation direction. Since the gradient force exceeds the scattering force, a stable optical confinement in 3D is achieved. The maximum total force is 0.97 pN.

A nanoparticle captured in an optical trap is prone to directed Brownian motion (cp. Chapter: Displacement of an optically trapped particle). The time-dependent x- and y-displacement of the gold nanoparticle inside the trap can be measured by tracking the center-of-mass of the optofluidic sensor in each frame of a video file and reveals the time series for the x- and y-direction. FFT of the time series gives the amplitude-frequency plots for the respective directions (cp. Chapter: 3.6). While the unperturbed trapped nanoparticle shows Brownian motion, and thus no signal in the FFT, the addition of a source leads to a displacement of the sensor that can be extracted through FFT analysis.

To detect any small external microfluidic disturbance and to achieve an enhanced signal to noise ratio in the frequency spectrum of the sensor particle a very stable trapping of the particle is required. A higher laser power implicates higher trap stiffness  $\kappa$  but also leads to heating of the nanoparticle which induces an unwanted increase of thermal fluctuations in the system. Although the trapping laser wavelength was chosen to be off-resonance with respect to the plasmon resonance of the sensor particle ( $\lambda \sim 530$  nm) it still possesses a finite absorption cross-section at this wavelength ( $\lambda = 1064$  nm). The absorption cross-section at  $\lambda = 1064$  nm was calculated with *MQMie* to be  $C_{abs}(1064 \text{ nm}) \cong 3 \cdot 10^{-8} \mu\text{m}^2$ . For comparison, at the plasmon resonance the

---

computed absorption cross-section was  $C_{abs}(530\text{ nm}) \cong 9.8 \cdot 10^{-6} \mu\text{m}^2$ . Thus, the laser power (in this case  $P = 100\text{ mW}$ ) had to be optimized in such a way that heating effects were minimized but a sufficiently stable trapping was achieved.

### Characterization of the microbiological flow source

A larva of Copepods was used as a biological source of microfluidic oscillations. The larvae of Copepods are called Nauplii and use rhythmic strokes of their antennae (each larva has three pairs of appendages at their head region) to swim in water<sup>107</sup> (see Figure 4.1.2). These rhythmic strokes shall in the following serve as source of microfluidic flow. Any investigations on the movement of the animal so far were based on microscopy studies by observing and counting the antenna strokes of the Nauplius directly during the measurement. Due to its size ( $\sim 100 - 500\ \mu\text{m}$ )<sup>108</sup> this often required measurements either one by one or the fixation of a single Nauplius to a substrate.

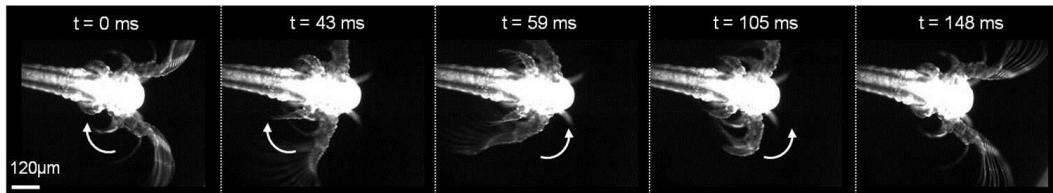


**Figure 4.1.2:** The movements of several Nauplii were analyzed independently by monitoring their swimming behavior under dark-field illumination with a high speed camera. In this example, one full oscillation of the periodic motion of the main arm of the large antennae took 148 ms which corresponds to a frequency of around  $f = 7\text{ Hz}$ .

Similarly, and for reference, we analyzed the movements of several Nauplii independently by monitoring their swimming behavior directly with a high speed camera (PCO.dimax) under dark-field illumination with a 10x air objective. An example is shown in Figure 4.1.2. One full oscillation of the periodic motion of the main arm of the large antennae took 148 ms, which corresponds to a frequency of around  $f = 7\text{ Hz}$ . The same Nauplius was observed over a longer time period of some seconds and also different Nauplii of the same sample were investigated. The frequencies for the swimming oscillation obtained from the direct observation were between  $f_{min} = 4.1\text{ Hz}$  and  $f_{max} = 7.2\text{ Hz}$ . The frequency and intensity of the strokes are indicators of the age, fitness, and environmental conditions of the animal<sup>109, 110</sup>. In particular, the latter point makes a non-invasive investigation of such animals interesting as it allows conclusions on the

overall conditions of an ecosystem. An attractive way to overcome the microscopic approach of direct observation is to observe the activity of a Copepod larva by using an optically trapped gold nanoparticle as an optofluidic nanodetector, as will be described in the following section.

### **Analysis of the movement of a Nauplius by optical tracking of an optically confined gold nanoparticle**

A schematic illustration of the experimental setup is shown in Figure 4.1.3. A Nauplius was swimming in water solution surrounding the optically trapped gold nanoparticle. The Nauplius uses rhythmic strokes of its antennae to swim in water. The fluidic oscillations that were generated by the animal propagated through the liquid medium and interacted with the optically trapped sensor. The generated microfluidic flow was measured by means of the displacement of an optically trapped gold nanoparticle. Trapping was achieved by setting up an optical tweezer at a wavelength of  $\lambda = 1064$  nm in a dark-field microscope. The wavelength of  $\lambda = 1064$  nm for the trapping laser was chosen to guarantee a stable confinement of the plasmonic nanodetector in the potential of the optical trap, as explained above<sup>2, 7</sup>. The beam was focused by a 100x/NA=1.0 water immersion objective and the trapping power was  $P = 100$  mW. Video files were captured with a color camera (Canon EOS 550D SLR) at a frame rate of 60 Hz for ca. 15 s in a dark-field configuration<sup>13</sup> (cp. Chapter 3.1.1.2).

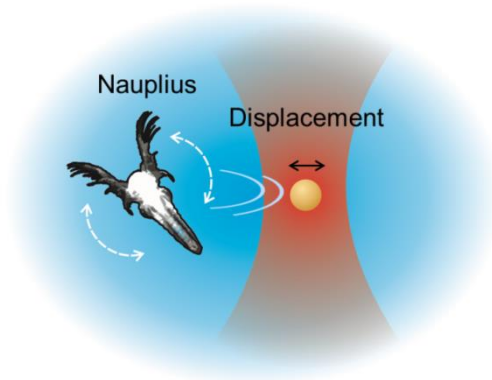


**Figure 4.1.3:** Sketch of the experimental setup. A gold nanoparticle is trapped in an optical tweezer at a wavelength of  $\lambda = 1064$  nm and detects the microfluidic oscillations of one Nauplius that swims in the water.

Figure 4.1.4 (a) shows a dark-field image of a gold nanoparticle that was trapped by the laser beam. The greenish color under dark-field illumination indicated the light scattering frequency of a single particle. Observing the trapped particle with a color camera ensured that just one plasmonic nanoparticle was confined by the focused laser.

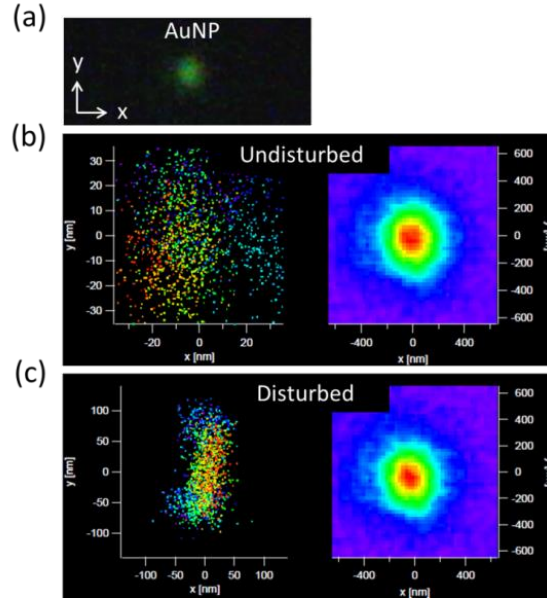


**Figure 4.1.4:** Optical trapping of a gold nanoparticle. (a) Dark-field image of a single trapped gold particle. (b) x-y-displacement of a gold nanoparticle that undergoes Brownian motion in the optical tweezer and is not disturbed by an external flow field. (c) x-y-displacement of the plasmonic nanosensor within the harmonic potential, after one Nauplius is added to the surrounding liquid. The microfluidic oscillations generated by the animal caused a distortion of the gold nanoparticle displacement in y-direction (please note the different scale bar).

Within the harmonic trapping potential, a linear restoring force  $F_{rest}$  pulled the plasmonic nanoparticle toward the trap center<sup>44, 45</sup>. This means on the one hand, the particle was subjected to Brownian motion with a MSD of  $\langle \Delta r^2(t) \rangle = 6Dt$  with  $t$  being the time and  $D$  being the temperature-dependent diffusion coefficient of a sphere (equation 2.2.12). On the other hand, the particle felt the external restoring trapping force<sup>46</sup>. It can be written (in 1D) as  $F_{rest} = \kappa x_{particle}(t)$  with  $x_{particle}(t)$  being the displacement of the particle with respect to the trap center and  $\kappa$  being the trap stiffness. The displacement of the particle within the trap depends therefore on the temperature  $T$  as well as on the trap strength  $\kappa$ . Therefore, as described above, the laser power has been carefully adjusted to ensure an optimal trapping. Without any external microfluidic source, the distribution of the particle position in x- and y-direction showed a Gaussian



behavior with a standard deviation  $\sigma_i^2 \cong \frac{k_B T}{\kappa}$ ,  $i = x, y$  (equation 2.2.14) around the trap center. Figure 4.1.4 (b) shows the measured x-y-displacement of a gold nanoparticle that undergoes Brownian motion in the optical tweezer and is not disturbed by an external flow field.

As soon as a Nauplius was added to the surrounding medium, the time-dependent, periodic movement of its antennae generated a flow field that interacted with the sensor particle. The nanoparticle in the optical trap started to oscillate in the direction of the hydrodynamic interaction (in this case y-direction) up to an amplitude of  $A_y = 100$  nm (Figure 4.1.4 (c)).

Figure 4.1.5 (a) and Figure 4.1.5 (b) show the amplitude-frequency spectra of a trapped gold nanoparticle, as a result of the FFT analysis of the x-y-displacement maps in Figure 4.1.4, without (black curve) and with (red curve) a Nauplius present in the surrounding medium. The amplitude frequency analysis in x- and y-direction reveals zero amplitude when no Nauplius is present (black curves in Figure 4.1.5). Similarly, only weak amplitudes were obtained in the x-direction of the Fourier spectrum when the Nauplius was present (Figure 4.1.5 (a)). In contrast, the y-direction of the frequency spectrum of the sensor showed a range of frequencies with strong amplitudes (Figure 4.1.5 (b)). This can be explained by the relative position of the Nauplius with respect to the flow sensor. High amplitudes in y-direction of the frequency spectrum indicate that the hydrodynamic interaction between animal and detector happened mainly in this direction (cp. Figure 4.1.4 (c)). The broad frequency range in the y-direction can be explained by the fact that not only the two main antennas of the Nauplius contributed to the signal, but also the smaller antenna pair and other body protrusions.

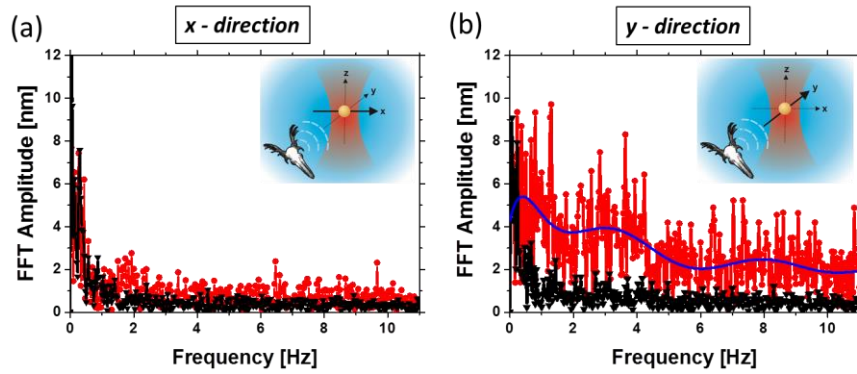


**Figure 4.1.5:** Amplitude-frequency spectra of a gold nanoparticle trapped next to a swimming Nauplius. (a) Black curve: x-direction of the frequency spectrum of an undisturbed nanoparticle in the optical trap as reference (cp. Figure 4.1.4 (b)). Red curve: x-direction of the frequency spectrum of the gold particle trapped next to a swimming Nauplius (cp. Figure 4.1.4 (c)). Inset: The microfluidic oscillations generated by the Nauplius pointed mainly in y-direction. This explains that the Fourier transformation of the time-dependent nanoparticle position in x-direction did not show any strong amplitude. (b) Black curve: Frequency spectrum of the undisturbed reference gold particle and of the gold particle trapped next to the swimming Nauplius (red curve, cp. Figure 4.1.4 (c)) in y-direction. Since the microfluidic waves of the organism pointed mainly in y-direction (inset), increased amplitudes with local maxima over the range of 0 to 11 Hz can be seen in the spectrum.

For all flow field measurements, frequency maxima at around  $f_{min} = 3.0$  Hz and  $f_{max} = 7.2$  Hz for the Nauplius movement were found (blue curve in Figure 4.1.5 (b)). This is in good accordance to the directly observed frequencies of the biological microorganism and also fits well to the expected frequency range for Nauplii of an age of approximately two weeks<sup>107, 110</sup>.

### Chapter summary and outlook

In this Chapter, the approach to read out microfluidic oscillations with a single gold sphere as an optomechanical nanosensor was extended and applied for the first time to a living microorganism as source of flow. The trapping conditions e.g., trapping wavelength and power have been optimized to achieve ideal trapping conditions. For this, numerical simulations have been performed to calculate the optical forces acting on the nanoparticle. A larva of Copepods was used as a biological source of microfluidic oscillations. The flow generated by a Nauplius was measured by means of an optically trapped gold nanoparticle. Without any external microfluidic source, the distribution of the time-dependent particle position in x- and y-direction showed a Gaussian profile. In the amplitude-frequency plots of the optofluidic detector almost no signal could be seen in x-direction when the Nauplius was present. In contrast, the y-direction of the frequency spectrum showed a range of frequencies with strong amplitudes. This can be explained by the relative position of the Nauplius with respect to the flow sensor. For all flow field measurements, frequency maxima between  $f_{min} = 3.0$  Hz and  $f_{max} = 7.2$  Hz for the Nauplius movement were found. This is in good accordance to the directly observed frequencies of the biological microorganism.

Overall, the method to detect the motion of a Nauplius by a single gold nanoparticle in an optical tweezer represents a non-invasive way to analyze the activity of the aquatic specimen without the requirement to disturb or even see the Nauplius during the measurement. Additionally, the direction of the microfluidic oscillations can be determined by analyzing the direction-dependent Fourier spectra of the time-dependent displacement of the nanoparticle. The optical tweezer configuration rendered it possible to detect even small fluidic oscillations in an aqueous solution with high sensitivity.

Copepods are typical examples for bio indicators, because they can be found in nearly any water habitat<sup>111, 112</sup>. Observing the activity and viability of these species from a water sample can thus be used to obtain information on the overall conditions of an ecosystem<sup>111</sup>. This experimental approach could expand the current methodology for water analysis and could be applied to gain information about the health and the integrity of aquatic ecosystems.

---

## 4.2 Application of a dielectric microparticle as optofluidic sensor for oscillatory flows

As discussed in the previous Chapter, an optically confined gold nanoparticle can be used for the detection of a microfluidic flow generated by a living microorganism. Even if the trapping laser wavelength is off-resonant to the plasmon resonance of the particle a finite heating of the nanoparticle occurs. This can induce an unwanted enhancement of thermal fluctuations in the system. To increase the sensitivity of detection, this Chapter seizes the idea to use a non-absorbing dielectric microparticle as optofluidic sensor of oscillatory flows. It allows a quantitative mapping of the vectorial velocity field in two dimensions around a microscale oscillator in water. The optofluidic method introduced in this Chapter paves the way for in-situ characterization of fast mixing microscale devices and for new detection methods able to provide location and recognition of moving sources that can be applied to both artificial and living microobjects with their own dynamics at the nanoscale (cp. Chapters: 4.3 Optical driving and sensing of helical microstructures in a fluidic environment; 4.4 Sensing the microfluidic flow generated by a single bacterial cell).

In the following work, the applied laser power  $P$  to confine a dielectric detector particle with a diameter of  $D = 1.76 \mu\text{m}$  in water at a wavelength of  $\lambda = 1064 \text{ nm}$  optically was  $P = 26 \text{ mW}$ ,  $P = 30 \text{ mW}$ ,  $P = 110 \text{ mW}$  and  $P = 127 \text{ mW}$ . The trapping beam was focused by a (100x or 63x)/NA = 1.0 water immersion objective. To characterize the detector trap, the total electromagnetic force acting on the sensor was computed for these laser beam powers. The challenge of the calculation is that neither the Rayleigh approach nor the ray optics approach is a good approximation for the mathematical description of the optical force (cp. Chapter: 1). For a particle with a diameter at the same scale as the wavelength of the strongly focused trapping beam (as it is the case here), the extended Generalized Lorenz Mie theory (GLMT) has to be applied. A brief summary of the GLMT as well as the numerical simulation of the electromagnetic force acting on the detector particle can be found in the first part of this Chapter. In the second part, the source of the analyzed flow is described. An oscillatory microflow was generated by an optically confined microparticle moving in a dipole-like pattern. For this aim, the optofluidic technique was extended by implementing a multiple tweezers configuration at different wavelengths under a dark-field microscope. Two alternately chopped traps in close vicinity induce an

oscillation of the trapped bead between both tweezers, in the following termed as source of flow. In the main part of this Chapter, the vectorial velocity pattern around the dipolar flow source is analyzed. This is done by optical tracking of the dielectric sensor in a third trap that could be positioned at different points in space around the source. The experimentally measured results are compared to numerical simulations of the flow field distribution. The comparison between numerical simulations and the measured data show a good agreement of the field pattern around the oscillating microsource when the detecting particle was located along the dipole axis, and at intermediate positions far from the source. Finally, the Chapter is concluded and possible applications of the presented technique are discussed.

### Optical forces on a dielectric microparticle

In the following work, optically confined silicon dioxide ( $\text{SiO}_2$ ) microspheres with diameters at the same scale as the wavelength of the (strongly focused) trapping beam were used as optofluidic sensors. A generalization of the Lorenz Mie theory (cp. Chapter: Lorenz Mie theory) provides the possibility to calculate the electromagnetic force acting on a microsphere with a size dimension at the same order as the trapping wavelength ( $a \sim \lambda$ ). The Generalized Lorenz Mie theory (GLMT) implicates an analytical description of an arbitrarily shaped incident electromagnetic wave and is not restricted to the size of the trapped sphere. For the description of a single beam optical trap, following assumption is made: The incident electromagnetic field is not considered to be planar any more (as it is the case in the Lorenz Mie theory). It has the shape of a focused Gaussian  $\text{TEM}_{00}$  (transversely localized) beam that is Fresnel diffracted on a homogenous sphere<sup>113, 21</sup>. Solving Maxwell's equations with necessary boundary conditions, the transversal electric ( $TE$ ) and transversal magnetic ( $TM$ ) Bromwich potential<sup>114</sup> in polar coordinates for a transversely localized incident beam can be written as infinite superposition according to:

$$U_{TE}^{inc} = \sum_{n=1}^{\infty} \sum_{m=-n}^n \frac{E_0}{k} i^n C_n^{pw} g_{n,TE}^m \psi_n(kr) P_n^{|m|}(\cos\theta) \exp(im\varphi) \quad (4.2.1)$$

$$U_{TM}^{inc} = \sum_{n=1}^{\infty} \sum_{m=-n}^n \frac{E_0}{k} i^n C_n^{pw} g_{n,TM}^m \psi_n(kr) P_n^{|m|}(\cos\theta) \exp(im\varphi) \quad (4.2.2)$$

---

With  $n, l, p \in \mathbb{N}$ ,  $C_n^{pw} = (2n + 1)/2n(n + 1)$ ,  $\psi_n$  being the Riccati-Bessel functions,  $P_n^{|m|}$  being the associated Legendre functions and  $g_{n,TE}^m$  and  $g_{n,TM}^m$  being the beam shape coefficients<sup>113</sup>. The scattered transversal electric (*TE*) and transversal magnetic (*TM*) Bromwich potentials are then:

$$U_{TE}^{scat} = - \sum_{n=1}^{\infty} \sum_{m=-n}^n \frac{E_0}{k} i^n C_n^{pw} B_n^m \xi_n(kr) P_n^{|m|}(\cos\theta) \exp(im\varphi) \quad (4.2.3)$$

$$U_{TM}^{scat} = - \sum_{n=1}^{\infty} \sum_{m=-n}^n \frac{E_0}{k} i^n C_n^{pw} A_n^m \xi_n(kr) P_n^{|m|}(\cos\theta) \exp(im\varphi) \quad (4.2.4)$$

With  $n, l, p \in \mathbb{N}$ ,  $\xi_n$  being the spherical Riccati-Hankel functions,  $P_n^{|m|}$  being the associated Legendre functions,  $A_n^m$  and  $B_n^m$  being the wave scattering amplitudes,  $E_0$  being the peak electric field strength and  $C_n^{pw} = (2n + 1)/2n(n + 1)$ <sup>113</sup>.

The general scattering amplitudes  $A_n^m$  and  $B_n^m$  can be expressed by:

$$A_n^m = a_n g_{n,TM}^m \quad (4.2.5)$$

$$B_n^m = b_n g_{n,TE}^m \quad (4.2.6)$$

where  $g_n^m$  are the beam shape coefficients<sup>115, 116, 117</sup>. In the plane wave limit, as it is the case for the Lorenz Mie theory, the shape coefficients  $g_n^m$  become one and the general scattering amplitudes  $A_n^m$  and  $B_n^m$  are identical with the scattering amplitudes when a planar incident wave is assumed:  $A_n^m = a_n$  and  $B_n^m = b_n$  (cp. Chapter: Lorenz Mie theory)<sup>113, 114</sup>. The scattered fields described by the GLMT can be calculated by taking multiple vector derivatives of the scattered Bromwich potentials described in equation 4.2.2 and 4.2.3<sup>20, 118</sup>. For the calculation of the total optical force acting on a SiO<sub>2</sub> microparticle, the *T-matrix* method was applied<sup>119, 120</sup>. The *T-matrix* is a transition matrix and describes the transformation of the beam shape coefficients of the incident wave to the beam shape coefficients of the scattered wave. From equations 4.2.5 and 4.2.6 the *T-matrix* can be defined as:

$$\mathbf{T} = \begin{pmatrix} a_m & 0 \\ 0 & b_m \end{pmatrix} \quad (4.2.7)$$

In the GLMT the  $T$ -matrix is diagonal, for non-spherical particles it is not <sup>120</sup>.

The radiation pressure transferred from the beam to the spherical particle is proportional to the net momentum subtracted from the incident beam <sup>114</sup>. In the GLMT, the radiation pressure force  $\mathbf{F}(\mathbf{r})$  can be split into a longitudinal component (along the beam propagation,  $z$ -direction) and two transverse components ( $x$ -,  $y$ -direction) <sup>114, 20</sup>:

$$\mathbf{F}(\mathbf{r}) = \frac{n_m}{c} I_0 (C_{pr,x}(\mathbf{r}) + C_{pr,y}(\mathbf{r}) + C_{pr,z}(\mathbf{r})) \quad (4.2.8)$$

with  $C_{pr,i}$  ( $i = x, y, z$ ) being the radiation pressure cross sections in the three dimensions,  $n_m$  being the refractive index of the surrounding medium,  $I_0$  being the intensity at the beam center, and  $c$  being the speed of light. The radiation pressure cross sections  $C_{pr,i}$  ( $i = x, y, z$ ) in turn can be expressed by the  $T$ -matrix elements (equation 4.2.7) and the beam shape coefficients  $g_n^m$  (further reading on the exact expressions for the cross sections can be found here: 114, 121). With this, the total electromagnetic force acting on a spherical SiO<sub>2</sub> microparticle can be calculated. To this goal, a computational toolbox implemented in Matlab and provided by Nieminen et al. was used <sup>120</sup>. In the calculation, the field is not expanded by means of the Bromwich potentials but by means of a more general set of basis-functions (vector spherical wave functions) <sup>120</sup>. However, the formalism itself does not change.

In this work, the applied laser power  $P$  to trap optically a SiO<sub>2</sub> detector particle with refractive index  $n = 1.45$  and diameter  $D = 1.76 \mu\text{m}$  in water at a wavelength of  $\lambda = 1064 \text{ nm}$  optically was  $P = 26 \text{ mW}$ ,  $P = 30 \text{ mW}$ ,  $P = 110 \text{ mW}$  and  $P = 127 \text{ mW}$ . The trapping beam was focused by a (100x or 63x)/NA = 1.0 water dipping objective. The total electromagnetic force that kept the particle in the optical trap was computed for the four different powers and can be seen in Figure 4.2.1. This delivered a precise determination of the trapping conditions for non-metallic microparticles.

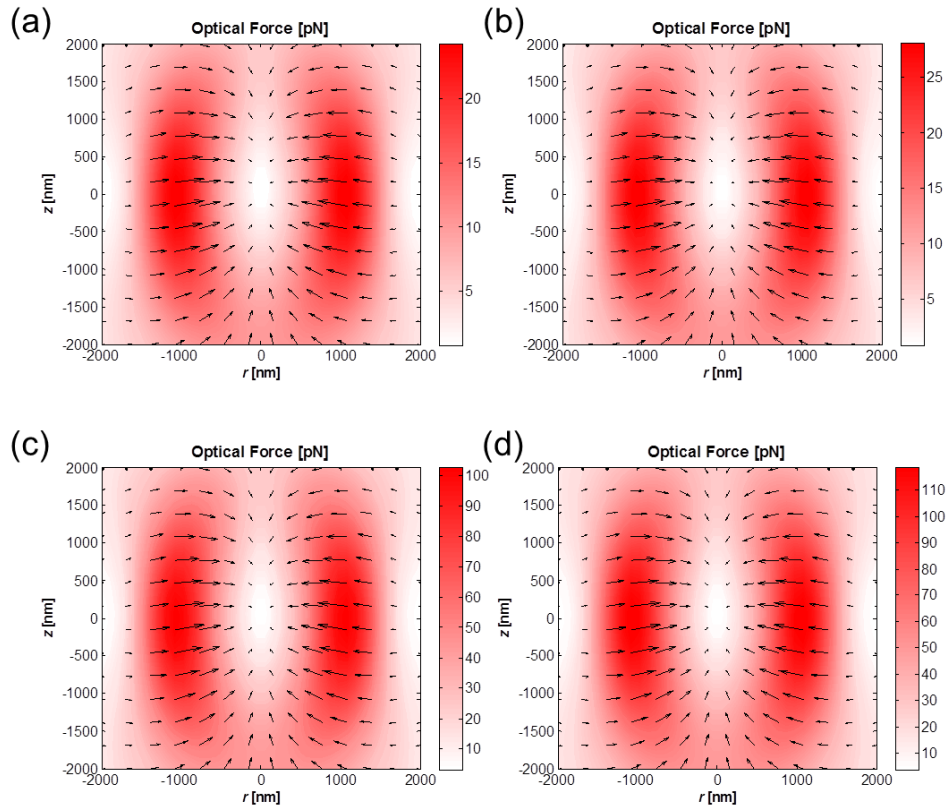


**Figure 4.2.1:** Numerical simulation of the total electromagnetic force acting on a  $\text{SiO}_2$  sphere with a diameter of  $D = 1.76 \mu\text{m}$  and trapped with a strongly focused laser beam at a wavelength of  $\lambda = 1064 \text{ nm}$ . The beam is focused by a water dipping objective with numerical aperture  $\text{NA} = 1.0$ . The optical trap has a laser power of (a)  $P = 26 \text{ mW}$ , (b)  $P = 30 \text{ mW}$ , (c)  $P = 110 \text{ mW}$  and (d)  $P = 127 \text{ mW}$ .



### Characterization of the dipolar flow source

This Chapter is based on my co-author paper published in *Appl. Phys. Lett.*<sup>122</sup>. As source of an oscillatory microflow served a SiO<sub>2</sub> sphere with a diameter of  $D = 1.76 \mu\text{m}$  that oscillated periodically in a dipole-like mode. To realize this, the beam of a continuous-wave laser at a wavelength of  $\lambda = 532 \text{ nm}$  was first expanded by a home-built telescope to slightly overfill the back aperture of a water dipping microscope objective 63x/NA = 1.0 (cp. Chapter: 3.1.1.3). The beam was then split into two beams of equal power  $P = 60 \text{ mW}$  and guided into the objective at a distance of 910 nm to each other. A chopper was used to block one of the beams and let the other pass at a time creating two alternating, closely spaced optical traps (Figure 4.2.2).

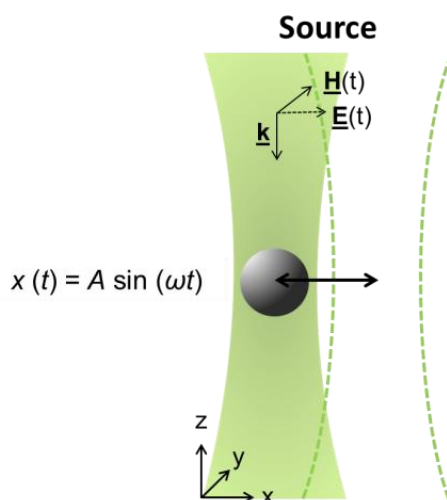


**Figure 4.2.2:** Sketch of the source generating an oscillatory flow. A SiO<sub>2</sub> microparticle with a diameter of  $D = 1.76 \mu\text{m}$  oscillated periodically in a dipole-like mode between two optical traps. For that the trapping beam ( $\lambda = 532 \text{ nm}$ ) was split into two beams of equal power  $P = 60 \text{ mW}$ . A chopper was used to block one of the beams and simultaneously let the other pass creating two alternating, closely spaced optical traps. The oscillatory motion of the source bead could be described by a harmonic function of the form  $x = A \sin(\omega t)$ , with  $\omega = 2 \pi f$  and amplitude  $A$ .

The source bead was driven to oscillate between the two traps along the x-axis at a frequency  $f = 197 \text{ Hz}$  as defined by the chopper creating an oscillatory flow around it. The driving frequency was chosen since it is not a multiple of 50 Hz. At the set frequency the oscillatory motion of the source bead, detected through the dark-field microscope, resembled a harmonic function of the form  $x = A \sin(\omega t)$ , with  $\omega = 2 \pi f$  and the amplitude  $A = (405 \pm 6) \text{ nm}$  defined as half the separation between the two beams. The experiments were conducted in ddH<sub>2</sub>O water. This experimental configuration allowed a generation of

a 2D oscillating flow field with the dipolar oscillating SiO<sub>2</sub> sphere acting as the flow source. In the following Chapter, the detector unit of the dark-field configuration will be introduced which is based on the optical tracking of a dielectric sensor (trapped SiO<sub>2</sub> sphere) in a third trap. The arrangement is designed such that the dielectric sensor can be positioned at different points in space around the source, thus, facilitating to create a 2D field map.

### Microscale mapping of an oscillatory flow

This Chapter is based on the work of S. Nedev et al. published in *Appl. Phys. Lett.*<sup>122</sup>. The main part of this Chapter describes the idea to use a dielectric microparticle as optofluidic sensor to quantitatively map the 2D oscillating flow with microscale resolution. For the detection of the oscillatory flow pattern, an optically trapped SiO<sub>2</sub> microparticle with a diameter of  $D = 1.76 \mu\text{m}$  was used and could be positioned at different points in space around the source (Figure 4.2.3).

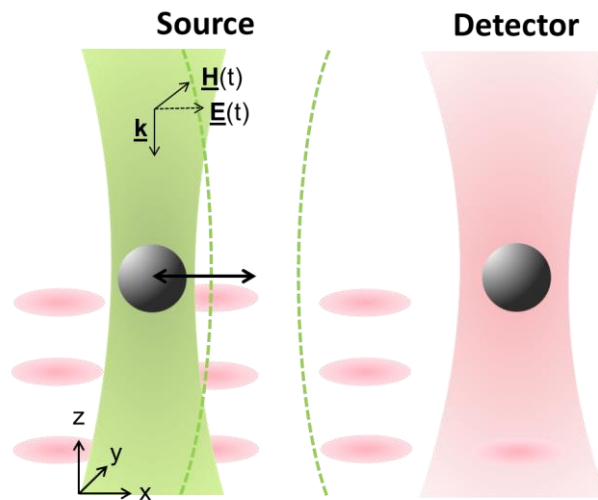


**Figure 4.2.3:** Schematic of the experimental setup to map the oscillatory flow around the source with a dielectric microparticle. For the flow field detection a SiO<sub>2</sub> twin microparticle was trapped at  $\lambda = 1064 \text{ nm}$  and positioned at different points in space around the source.

Therefore, the beam of a second laser at a wavelength of  $\lambda = 1064 \text{ nm}$  was set to a power of  $P = 110 \text{ mW}$ , and was used to optically confine the sensor bead (cp. Chapter: 3.1.1.3).

Before the trapping beam entered the microscope, it was expanded by a beam expander and two mirrors in front of the microscope were used to place the sensor particle in different x- and y-positions around the source. Both, the source and the detector beads were focused by a water dipping microscope objective 63x/NA = 1.0 and illuminated by a dark-field condenser. The beams were focused on the same plane. Their individual motion was recorded via their white light Rayleigh scattering by a high-speed camera (PCO.dimax) at a frame rate of 1000 Hz. Analyzing the time-dependent x- and y-position of the sensor particle inside the detector trap rendered it possible to detect a 2D map of the velocity field around the oscillating source. FFT of the detector time series resulted in amplitude-frequency plots in x- and y-direction for each position of the detector bead (cp. Chapter: 3.6). The amplitude  $A(FFT_i)$  was calculated as (equation 3.6.5):

$$A(FFT_i) = 2 \sqrt{\text{Re}_i^2 + \text{Im}_i^2} / N_0$$

with  $i$  being the x- or y-direction,  $N_0$  being the number of frames, and  $Re$  and  $Im$  being the real and imaginary part of the FFT.

Figure 4.2.4 shows a snapshot of a typical experimental video of the upper right quadrant with respect to the source (S) that is located at the origin. The detector bead (D) was placed at 60 different positions around it covering more than  $16 \times 16 \mu\text{m}^2$ .

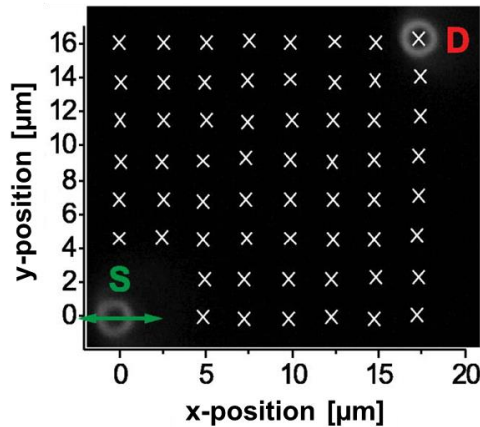


**Figure 4.2.4:** Snapshot of a typical experimental video of the upper right quadrant with respect to the oscillating source bead (S) that is located at the origin. The source oscillated permanently, while the detector bead (D) was placed at 60 different positions around it covering more than  $16 \times 16 \mu\text{m}^2$ . (Taken from 122).

In the experiment, the source was oscillating permanently. 1 s after locating the detector at each position, 5 s frame sequences were recorded and processed with a tracking-software (cp. Chapter: 3.6). This provided the time series of the x- and y-displacements of both source and sensor particle.

The amplitude-frequency plots of the detector in x- and y-direction showed sharp peaks at the driving frequency for the oscillating source  $f=197$  Hz for both directions (Figure 4.2.5). The spectra shown in Figure 4.2.5 were obtained with the detecting particle positioned at the maximum distance from the source (as shown in Figure 4.2.4). The displacement of the source was  $\sim 400$  nm along the x-direction and  $\sim 50$  nm along the y-direction. Even at the maximum distance, clear peaks of similar amplitude at  $f=197$  Hz in both directions were observed. Since the oscillation of the source is not strictly harmonic, the contribution of other harmonics contained in the source appeared as additional peaks in the spectra. Analysis of different time ranges of the same measurement provided the same amplitude response, meaning that a steady state of the combined source and detector system was reached within 1 s.

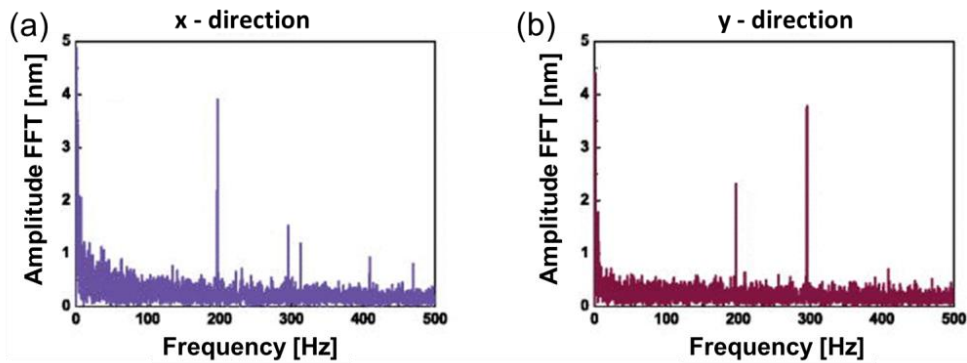


**Figure 4.2.5:** Amplitude-frequency plots of the detector particle in x- and y- direction. They show sharp peaks at the oscillating frequency of the source at  $f=197$  Hz. The spectra were obtained with the detecting particle positioned at the maximum distance from the source (as shown in Figure 4.2.3). Since the oscillation of the source is not strictly harmonic, the contribution of other harmonics contained in the source appears as additional peaks in the spectra. (Taken from 122).

From the height of the peak at  $f=197$  Hz in the x- and y-direction (cp. Figure 4.2.5), the amplitude of the displacement of the detector particle was obtained for this frequency. The experimentally measured amplitude  $A_i$  ( $f=197$  Hz),  $i=x,y$  of the displacement of the detector bead inside the trap is directly related to the velocity of the surrounding

water molecules  $v_i$ : The frictional drag coefficient  $\gamma$  for a spherical object is given by  $\gamma_{sphere} = 6 \pi \eta r$  (equation 2.2.11) with  $\eta$  being the dynamic viscosity of the medium and  $r$  being the particle radius. An insertion of this expression into the equation of motion for a particle confined in a trapping potential with trap stiffness  $\kappa$ :  $v_{particle,i} \gamma_{sphere} + \kappa A_i(f) = F(f)_{thermal}$ ,  $i = x, y$  (equations 2.2.15 and 2.2.16) reveals the relation between flow velocity and maximal detector displacement at the frequency  $f = 197$  Hz:

$$\kappa A_i = 6 \pi r \eta v_i \quad (4.2.9)$$

A  $\text{SiO}_2$  microparticle is non-absorbing and thus heating effects due to absorption that can lead to changes of the viscosity were neglected, which delivers a great advantage over the use of metallic nanoparticles, as described in the previous Chapter. Direct heating of the water by the trapping laser beam is on the order of 10 K per W at the focus<sup>123</sup>. The applied laser power to trap the detector bead was set to be  $P = 110$  mW. Thus, a viscosity change due to direct heating was also neglected. The dynamic viscosity of water was therefore considered to be constant with a value  $\eta_{water} = 9.3 \cdot 10^{-4} \text{ Pa} \cdot \text{s} \cong 0,001 \text{ Pa} \cdot \text{s}$  at 23 °C.

To obtain the associated velocity field of the oscillatory flow from equation 4.2.9, the optical tweezer holding the detector was calibrated by the power spectral density procedure<sup>124, 125</sup>. From that, the corner frequencies and the trap stiffness in x- and y-direction were determined (cp. Chapters: Displacement of an optically trapped particle, Power spectrum of an optically trapped particle). The velocity of the measured signal with magnitude  $\|\mathbf{v}_{exp}\| = \sqrt{v_x^2 + v_y^2}$  and the direction defined by the angle  $\tan(\theta_{exp}) = A_y / A_x$  was evaluated for each position of the detector bead. A more detailed description of these measurements can be found in the work of S. Nedev et al.<sup>122</sup> or in the Appendix of this thesis. There, also the simulations of the oscillatory flow field are shown which are in an excellent agreement with the measured data, demonstrating the feasibility of the given device for the detection of flow fields. Moreover, deviations between theory and experiment in particular in close distances between the detector and the source delivered an understanding to the effect that not only incompressible flow, but also sound could contribute to the measured flow in the near-field. This is a very important finding

---

for optofluidic location and recognition experiments and might trigger further investigations in this direction, as conditions are reached which in normal circumstances are difficult to achieve.

### **Chapter summary and outlook**

In this Chapter, an optofluidic method to quantitatively map a 2D oscillating flow with microscale resolution was demonstrated. A prerequisite for the given experimental configuration is that heating effects need to be avoided for an undisturbed measurement of the flow field. It was shown that a trapped SiO<sub>2</sub> microparticle can be used as a highly precise flow field sensor.

To characterize the detector trap, a brief summary of the GLMT was given and the optical force acting on the optically confined detector particle with a size dimension at the scale of the trapping wavelength was computed. This delivered a precise determination of the trapping conditions for non-metallic particles.

The vectorial velocity field around a micro-size SiO<sub>2</sub> particle oscillating in a dipole-like mode in a home built, chopper based dual tweezers configuration was mapped by optical tracking of a confined twin detector particle positioned at different points around the source. This sophisticated experimental setup was realized by setting up a multiple tweezers configuration at different wavelengths allowing position-dependent measurements.

The experimental technique presented in this Chapter can serve as reference for an understanding of the fundamentals of oscillatory microflows as well as their detection by an optomechanical sensor particle. At small scales and low Reynolds numbers, laminar flow is dominant. Viscous forces that arise from shearing between velocity-isosurfaces dominate inertial forces. The main transport mechanism for mass is diffusion and a mixing in the low Reynolds number regime is not easy to realize. An oscillatory microflow could be very useful to mix liquids in laminar systems.

Furthermore, the optofluidic method introduced in this Chapter paves the way for new detection methods able to provide location and recognition of moving sources that can be applied to both, artificial and living microobjects with their own dynamics at the nanoscale. The latter point will be discussed in the following Chapters, where a similar detection method is implemented to understand the fluidic dynamics around helical microobjects as well as living bacteria at the nanoscale (cp. Chapters: 4.3 Optical driving and sensing of helical microstructures in a fluidic environment; 4.4 Sensing the microfluidic flow generated by a single bacterial cell).

---

### 4.3 Optical driving and sensing of helical microstructures in a fluidic environment

One of the current efforts in engineering these days is the fabrication of “micro-bots” that can mimic the motile behavior of biological microorganisms e.g., bacterial cells <sup>126</sup>. Besides a highly precise shape at a very small scale, an accurate control mechanism is needed for the movement of these artificial microswimmers, both of which the following Chapter will focus on. Regarding the motion in the low Reynolds number regime, Brownian motion dominates inertial motion (see Chapters: 2.2 and 2.3) <sup>127</sup>. Therefore, a time-reversible swimming motion does not lead to any directed movement (see Chapter: Locomotion of microbiological objects at low Reynolds number). Considering these restrictions, external magnetic fields have been used to rotate and propel ferromagnetic, screw-like “micro-bots” through aqueous media <sup>126, 128-134</sup>. On the other hand, a light-driven rotation of trapped microstructures can be realized in various ways. First, the use of Laguerre-Gaussian beams that possess on-axis phase singularity and helical phase fronts. In this case, the Poynting vector follows a corkscrew-like motion and orbital angular momentum is transferred to a trapped particle <sup>135, 136</sup>. Next, spin angular momentum of circularly (elliptically) polarized light can be used to rotate birefringent particles in an optical trap <sup>135, 137, 138</sup>. Furthermore, it is possible to align and rotate plasmonic nanorods with linearly polarized laser beams <sup>139, 140</sup>. Finally, a conventional, non-polarized laser beam allows a simultaneous trapping and rotation of objects with shape anisotropy <sup>141</sup>.

The endeavor of this work is to detect the microfluidic flow field generated by a trapped bacterial cell in its surrounding medium by means of optomechanical sensor. Therefore, as a first step, an optically confined and rotating microhelix was used to model the mechanical and dynamical properties of the living organism. This Chapter describes the use of an optical tweezer for initiating a light-driven rotation of chiral microobjects in an aqueous environment. A rotating helical microstructure serves as a model system for the cork-screw motion of a living bacterial cell (see Chapter: Bacterial motility: “Tumbling” and “running” states). The focus of investigation is the establishment of an optofluidic detection method with an optically driven microhelix as source of flow. From that, conclusions can be drawn about what conditions have to be fulfilled for an



optomechanical detection of the microfluidic flow generated by a similar biological system e.g., a bacterium.

In the first part of this Chapter, the microscrews used in this work are described and their dynamic behavior in an optical trap is characterized by direct observation. In the main part, the optomechanical detection method for the flow generated by an optically driven microhelix is established. Conclusions are drawn about the conditions that have to be fulfilled for a successful optofluidic sensing of the flow field around such a source. Finally, the Chapter is summarized and future perspectives as well as applications are discussed.

#### Characterization of an optically confined microhelix

Colloidal, screw-like microstructures, serving as the microscrews in this work, with length scales down to 1  $\mu\text{m}$  can be fabricated with the evaporation method termed *glancing angle deposition* (GLAD)<sup>126, 128</sup>. Sub-micron seeds are deposited on a wafer-substrate. The substrate in turn is positioned in an incident vapor flux with a certain angle between wafer and vapor beam<sup>126</sup>. A constant, azimuthal rotation of the substrate leads to a formation of chiral microstructures (Figure 4.3.1 (a) and (b)).

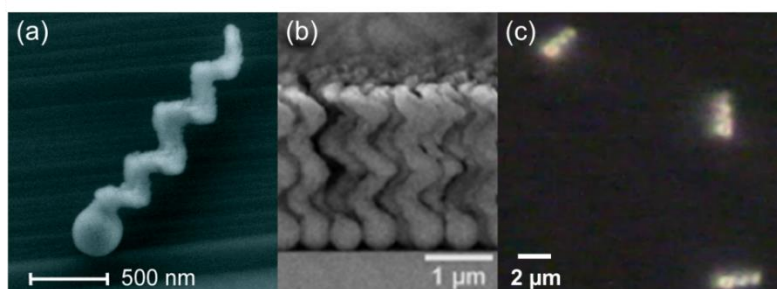


**Figure 4.3.1:** (a) SEM image of a single silicon dioxide screw (Taken from 128). A large number of screws can be fabricated by physical vapor deposition GLAD (b) (Taken from 128). The micropropellers are detached from the wafer-substrate by sonication and individual screws can be seen clearly under a dark-field microscope (c).

For the micropropellers used in this work, silicon dioxide ( $\text{SiO}_2$ ) beads were taken as seed material on the wafer. A  $\text{SiO}_2$  vapor beam was incident at ca.  $85^\circ$ <sup>128</sup>. The shape of the

---

helical structures depends on the angular speed of the wafer ( $\sim 0.1$  rpm) as well as on the deposition rate (e.g., few Ångströms per second)<sup>126</sup>. The SiO<sub>2</sub> screws used here were fabricated by our collaborators from the Peer Fischer Group (Max-Planck-Institut für Intelligente Systeme, Stuttgart) and had a diameter of 530 nm and a length of 2.35  $\mu\text{m}$ . The helical propellers were detached from the substrate by sonication and could be seen clearly when they were imaged by a 100x/NA=1.0 water immersion dark-field objective (Figure 4.3.1 (c)). It was possible to distinguish the head and the thread of the SiO<sub>2</sub> screw by eye.

The chiral microobjects were confined optically at a wavelength of  $\lambda = 1064$  nm. The beam was focused by the same 100x/NA=1.0 water immersion objective used for imaging as mentioned above (see Chapter: 3.1). The linearly polarized laser beam did not carry angular momentum. In this configuration, stable trapping of a screw was achieved in 3D in water (ddH<sub>2</sub>O) with a parallel alignment of the screw to the beam propagation direction. Once trapped in the optical tweezer with a power of  $P \geq 50$  mW, rotation of the screw could be seen by eye in about half of the experiments. By eye, the screw orientation always looked vertical in the trap. To investigate, the motion of a trapped screw was analyzed closely along with out-of-plane images of its intensity profile.

The white light Rayleigh scattering of a vertically trapped screw under dark-field illumination is shown in Figure 4.3.2 (a). For direct analysis of the screw rotation, a video file of the optically confined microhelix was captured with a color camera (Canon EOS 550D SLR) at a frame rate of 60 Hz for 15 s (cp. Chapter: 3.1). The center of the intense spot was tracked to reveal the time-dependent displacement in x- and y-direction (Figure 4.3.2 (b), cp. Chapter: 3.6). In case of a rotating screw, the time series showed a periodic oscillation for both directions with a phase shift of  $\pi/4$  between x and y, indicating an azimuthal circular motion of the trapped body. This motion behavior was only seen in about half of the experiments.

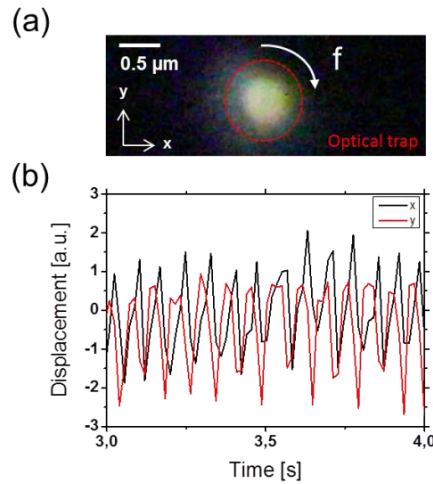


**Figure 4.3.2:** (a) Dark-field image of the backscattered light of a vertically trapped screw rotating at a certain frequency  $f$ . (b) Center-of-mass-tracking of the screw cross section revealed its time-dependent displacement in x- and y-direction. In case of a rotating screw, the time series showed a periodic oscillation for the x- and y-direction with a phase shift of  $\pi/4$ , indicating an azimuthal circular motion of the trapped body.

In order to investigate the dependence of screw rotation on orientation, the measured time series shown above were compared to out-of-plane images of the screw intensity profile. Under dark-field illumination, two distinct radial intensity profiles were distinguished when the image plane was slightly above the focal plane of the objective, showing the two possible vertical orientations of the screw in the trap (Figure 4.3.3 (a)).

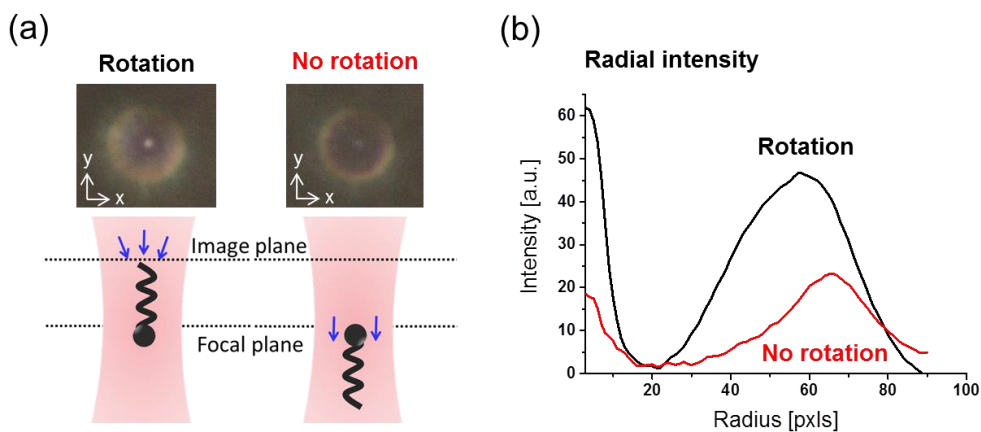


**Figure 4.3.3:** (a) Out-of-plane images of a screw under dark-field illumination for its two vertical orientation possibilities in the optical trap. (b) Radial intensity plots of the two distinguishable out-of-plane intensity profiles of a screw. When the screw showed an intensity profile as the black curve, it rotated in the trap. When the screw showed an intensity profile as the red curve, it did not rotate in the optical tweezer.

---

In the first case, the radial intensity profile revealed a high intensity at the origin (left panel in Figure 4.3.3 (a) and black curve in Figure 4.3.3 (b)). This was followed by a strong intensity decrease with increasing distance from the center of the spot. After an intensity minimum at a radius of 20 pixels, the intensity increased steadily again until it reached a second maximum at around 58 pixels. We interpreted the high intensity at the origin as a result of the thread of the screw which is in the focal plane of the objective (left panel in Figure 4.3.3 (a)). Instead, the broad outer intensity ring originates from the backscattered light off the head which is trapped slightly below the focal point of the objective. Taken together, these observations indicate that in the trap, the screw is aligned with the thread on the top and the head pointing downwards, as sketched in the left panel of Figure 4.3.3. Screws showing this intensity profile were observed to rotate in the optical trap.

In the second case, the radial intensity profile of the trapped screw is given in the right panel of Figure 4.3.3 (a) and the red curve in Figure 4.3.3 (b). The overall intensity was diminished compared to the first case (black curve), and the valley between the inner and outer maxima broader and less pronounced. These results indicate that both, the head and the thread of the screw are trapped below the focal plane, thus, less backscattered light could be collected by the objective, resulting in an overall lower intensity profile. Screws oriented in the tweezer with the thread pointing downwards “below” the head tended to not show rotation in the optical trap.

A screw is trapped in a similar way as the harmonically bound spherical particle, described in Chapter 2. The gradient force pulls the screw toward the highest point of field intensity, while the scattering force pushes it slightly below the focal plane. Thus, the helical thread can align either above or below the head (Figure 4.3.4).

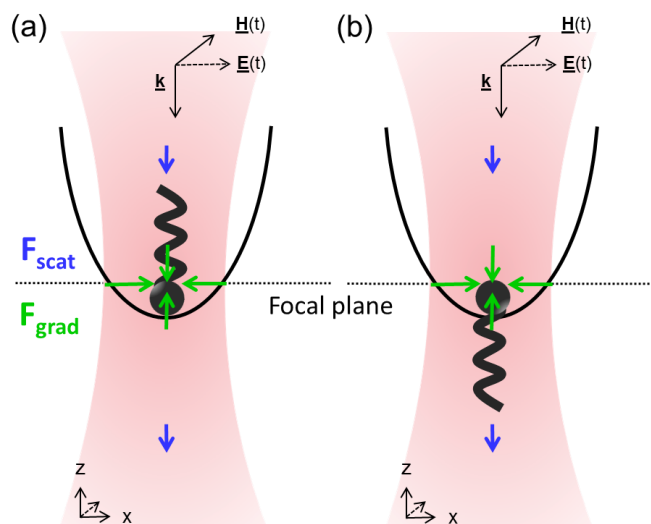


**Figure 4.3.4:** Sketch of a microhelix optically confined in a focused laser beam. The gradient force as well as the scattering force act on the microstructure within the harmonic potential. The gradient force pulls the object toward the highest point of field intensity. (a) The helical thread can either align above the head or (b) below the head.

As mentioned before, once trapped in an optical tweezer, a rotation of the screw was observed in about half of the experiments. This phenomenon occurred, when the image of the intensity profile of the screw (as described above) indicated an alignment of the screw with the head pointing downwards, i.e. the thread ‘above’ the head. The reason for the rotation in this particular case can be understood from the radiation pressure exerted from the light on the helical structure (Figure 4.3.5 (a)). Non-isotropic azimuthal scattering of the photons at the chiral thread creates a torque on the body. The driving force of rotation is thus a change of momentum of the photons when the incident radiation is reflected at the helical object - analogous to the rotation of a windmill. This implies that the rotation direction goes with the chirality of the microscrew. For a constant rotation, the optically induced torque must be in equilibrium with the viscous drag on the microhelix.

In the other half of the experiments, no rotation was observed e.g., when the thread was aligned pointing downwards (Figure 4.3.5 (b)). The standstill of the screw is explained by the incident photons that are isotropically deflected off the spherical head of the screw. The spherical head then blocks the radiation, preventing pushing on the helix. However, as discussed before, this is the prerequisite for a momentum transfer to the thread.

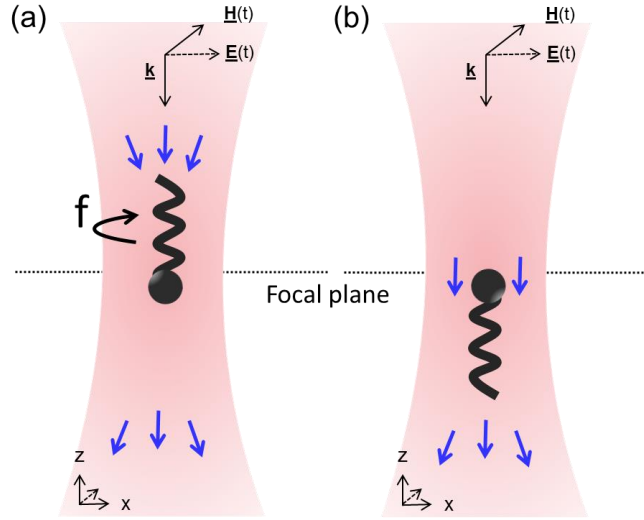


**Figure 4.3.5:** Schematic of the two possible screw orientations in the optical tweezer. (a) When the thread of the screw aligns above the head, non-isotropic azimuthal scattering of the photons at the helix leads to a torque acting on the body. The screw starts to rotate at a certain frequency  $f$ . (b) The thread is aligned below the head. Incident photons are isotropically deflected on the sphere. The spherical head blocks the radiation, preventing a pushing of the helix. Furthermore, the direction of the scattering force changes below the focal plane from an inward to an outward direction.

The frequency of rotation of the screw in the optical tweezer was obtained by recording a video file in the dark-field microscope and analyzing the time-dependent displacement of the center-of-mass of the screw. Taking the FFT thereof resulted in amplitude-frequency plots in  $x$ - and  $y$ -direction (cp. Chapter: 3.6). The amplitude  $A(FFT_i)$  was calculated as (equation 3.6.5):

$$A(FFT_i) = 2 \sqrt{\text{Re}_i^2 + \text{Im}_i^2} / N_0$$

with  $i$  being the  $x$ - or  $y$ -direction,  $N_0$  being the amount of frames, and  $Re$  and  $Im$  being the real and imaginary part of the FFT. The total amplitude  $A(FFT)$  was calculated as (equation 3.6.4):

$$A(FFT) = \sqrt{A(FFT_x)^2 + A(FFT_y)^2}$$

An example of an amplitude-frequency spectrum of a rotating microhelix is shown in Figure 4.3.6 (a). The screw was trapped with a laser power of  $P = 130$  mW and a

pronounced rotation frequency of 7 Hz was observed. Since the radiation pressure (as described above) is the driving mechanism of the screw rotation, the rotation frequency will increase linearly with the trapping laser power<sup>142</sup>. Thus, the next investigated aspect was the dependence of the rotation frequency of an optically confined microhelix on the power of the trapping laser beam.

Therefore, the power was increased gradually and a linear dependence of the microhelix rotation frequency and the laser power was observed (Figure 4.3.6 (b)). Notably, polarization-dependent measurements did not show any influence on the screw rotation frequency or direction. In case of 3D trapping, neither a right- nor a left-handed circularly polarized laser beam had a noticeable impact on the right-handed helix motion compared to a linearly polarized laser beam. This is in agreement with previously-reported observations<sup>142</sup>. These findings underline and confirm the theoretical description of the physical cause of screw rotation in case of our experimental condition.

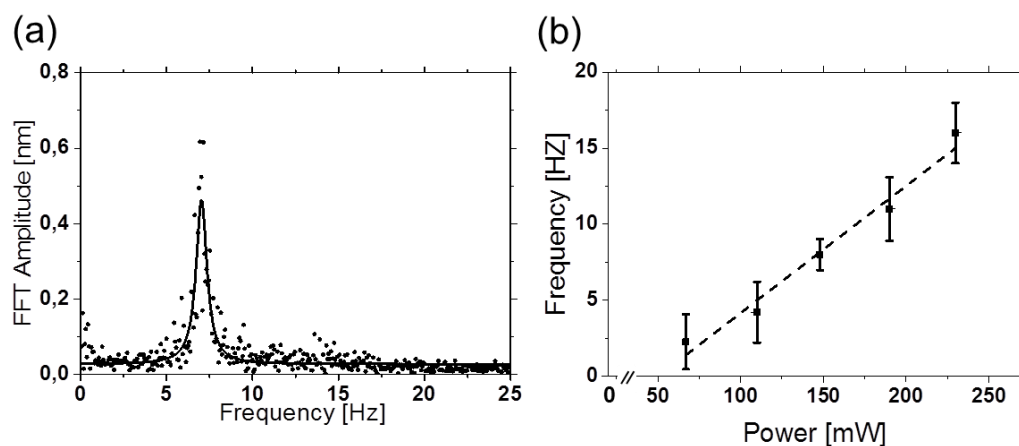


**Figure 4.3.6:** (a) Amplitude-frequency plot of a rotating screw. The mean value of the rotation frequency (obtained from the Gaussian fit) was  $f = 7$  Hz at a trapping laser power of  $P = 130$  mW. The trapping laser power was increased gradually and a linear dependence of the screw rotation frequency  $f$  on the power  $P$  was observed (b).

Optically controlled motion of the microhelices was also performed in media with higher viscosity than water (ddH<sub>2</sub>O). For these experiments, an aqueous D-Sorbitol (molecular weight: 182.17) solution with an end concentration of 2.7 mM was used. A power dependent series was analyzed and the results can be seen in Figure 4.3.7.

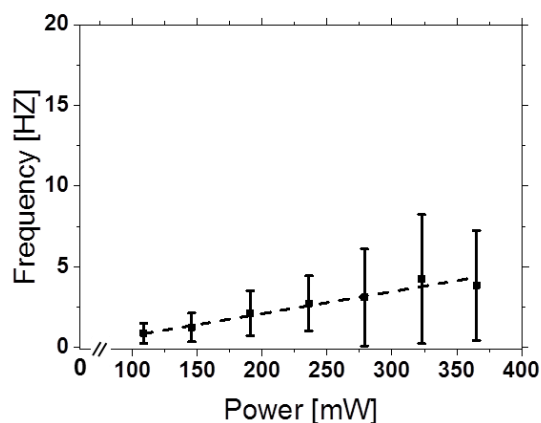


**Figure 4.3.7:** Frequency of screw rotation versus trapping laser power for a D-sorbitol solution with an end concentration of 2.7 mM. Due to the higher viscous drag, the rotation frequency for a certain power is smaller than in water (cp. Figure 4.3.6 (b)). The same holds for the slope of the linear dependence between rotation frequency and power.

Due to the higher viscous drag in the D-Sorbitol solution, the rotation frequency of a micropropeller for a certain trapping laser power was smaller than in water (cp. Figure 4.3.6 (b)). Furthermore, the slope of the linear dependence between rotation frequency and power was smaller when the experiments were conducted in the D-Sorbitol solution. This demonstrates that the torque depends not only on the laser power, but also on the viscosity of the medium, influencing the amplitude but also the frequency of the rotation. Those findings are very important for the implementation of the investigated technique for biological samples and imply that a careful choice and understanding of the medium is indispensable for a precise experimental design.

Finally, it should be mentioned that the rotation frequency of a screw is also highly sensitive to its individual shape. The GLAD method produces very homogenous microhelices, but small damages of the single screws due to the sonication process and long term storage are unavoidable. Nevertheless, the given results so far reveal a light-driven rotation of the microscrews, which allowed for the characterization of their motion behavior in an optical trap.

In summary, screw rotation depends on the vertical orientation of the helix in the optical tweezer, on the applied trapping power, the viscosity of the surrounding medium and on the individual shape of the microhelix.



Next, the Reynolds number of the flow around a rotating microscrew as well as the torque that is optically induced on the microhelix are estimated.

The Reynolds number can be calculated using equation 2.3.2. The tangential velocity of a screw with a radius  $r = 0.265 \mu m$  rotating with a frequency  $f = 5 Hz$  is  $V_t = 8.3 \mu m/s$ . The kinematic viscosity of water is  $\nu_{water} = 1.0 \cdot 10^{-6} m^2/s$  at  $20 \text{ }^\circ C$ . This gives a Reynolds number for the flow field of  $Re \cong 2 \cdot 10^{-6}$ . For a faster rotating microhelix e.g.,  $60 Hz$ , the Reynolds number of the surrounding flow pattern is  $Re \cong 1 \cdot 10^{-4}$ . At those low Reynolds numbers, the inertial forces are zero and a continuous torque must be transferred to the object to maintain its rotation (cp. Chapter: 2.3)<sup>143, 138, 142</sup>.

It is also possible to estimate the optically induced torque on the chiral structure<sup>142</sup>: The cause of rotation is the non-isotropic, azimuthal scattering of photons at the helical structure. The momentum of a single photon is:

$$p = \frac{h\nu}{c_{water}} \quad (4.3.1)$$

with Planck's constant  $h = 6.6 \cdot 10^{-34} Js$ , the frequency  $\nu$  and the speed of light in water  $c_{water} \cong 3/4 \cdot c_{vacuum}$ . For a trapping wavelength  $\lambda = 1064 nm$  the momentum of a single photon is:

$$p \cong 4.7 \cdot 10^{-28} Ns \quad (4.3.2)$$

The average radiation flux in the optical tweezer is given by<sup>144</sup>:

$$\Phi = \frac{P}{h\nu} \quad (4.3.3)$$

where  $P$  is the power of the trapping laser beam and assumed to be  $P = 100 mW$ . It follows that the average rate of photons is given as:

$$\Phi = \frac{0.1 W}{6.6 \cdot 10^{-34} Js \cdot (3/4 \cdot 2.998 \cdot 10^8 m/s) / (1064 \cdot 10^{-9} m)} \cong 7 \cdot 10^{17} s^{-1} \quad (4.3.4)$$

With 4.3.2 and 4.3.4, the optical force of the photons can be estimated:

---


$$F \cong 3 \cdot 10^{-10} N \quad (4.3.5)$$

The angular torque  $\tau_z$  acting on a body can be written as:

$$\tau_z = r_x \cdot F_y \quad (4.3.6)$$

where  $\tau_z$  is the angular torque in z-direction,  $r_x$  is the distance in x-direction from the rotation axis  $\mathbf{e}_z$  and  $F_y$  is the force acting perpendicular to  $r_x$  (pointing in y-direction). An estimation of the angle between the force of the photons  $\mathbf{F}$  and the rotation axis  $\mathbf{e}_z$  gives an angle of  $\alpha = 10^\circ$ . A projection of the force  $\mathbf{F}$  in y-direction is then given by  $F_y = F \cos(80^\circ)$ . With  $r_x = 0.265 \mu m$  and  $|\mathbf{F}| = F = 3 \cdot 10^{-10} N$  (equation 4.4.5), the optical torque on a microscrew trapped with  $P = 100 mW$  at  $\lambda = 1064 nm$  is at the order of

$$\tau_z \cong 1 \cdot 10^{-17} Nm \quad (4.3.7)$$

The torque on the chiral body due to momentum exchange of the deflected incident photons is in equilibrium with the viscous drag torque acting on the rotating helix.

### **Establishing the flow detection around an optically confined microhelix**

The focus of investigation in this Chapter is the establishment of a tool for flow detection around a light-driven microhelix. The flow field around a rotating microscrew was measured by means of a SiO<sub>2</sub> particle (detector) with a diameter of  $D = 1.76 \mu m$  that was optically trapped in the close vicinity of a light-driven screw (source) (Figure 4.3.8). This was achieved by setting up a dual optical tweezers configuration, both at a wavelength of  $\lambda = 1064 nm$  (cp. Chapter: 3.1.1.2). The two beams were focused by a 100x/NA=1.0 water immersion objective and their separation distance could be adjusted at the microscale. Under dark-field illumination, the white light Rayleigh scattering of the vertically trapped screw and the detector bead allowed for the precise optical tracking of both elements.

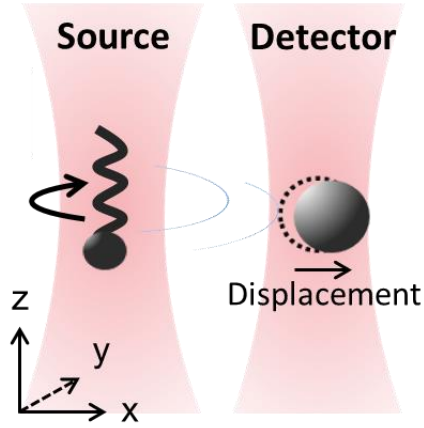


**Figure 4.3.8:** Sketch of the experimental configuration for the flow field measurement around a rotating microhelix. The microfluidic flow was detected by a  $\text{SiO}_2$  particle that was optically trapped in the close vicinity of a rotating screw. The distance between the two optical traps at  $\lambda = 1064 \text{ nm}$  could be adjusted at the microscale.

The individual motion of both, the microhelix and the detector particle was recorded at a frame rate of 60 Hz for ca. 15 s (Canon EOS 550D SLR). The time-dependent x- and y-position of both, the sensor and the rotating screw were analyzed (cp. Chapter: 3.6). After performing a FFT of the time series, amplitude-frequency plots in x- and y-direction were obtained for each. The Fourier amplitude  $A(FFT_i)$  was calculated using equation 3.6.5:

$$A(FFT_i) = 2 \sqrt{\text{Re}_i^2 + \text{Im}_i^2} / N_0$$

with  $i$  being the x- or y-direction,  $N_0$  being the amount of frames, and  $Re$  and  $Im$  being the real and imaginary part of the FFT. For the final analysis of the source and the detector movement, the total amplitude (equation 3.6.4)

$$A(FFT) = \sqrt{A(FFT_x)^2 + A(FFT_y)^2}$$

was used to achieve a better signal to noise ratio in the frequency spectra.

In this case, a helix was trapped with a power of  $P = 127 \text{ mW}$  and it rotated at a constant frequency in the optical trap. The amplitude-frequency spectrum of the screw can be seen in Figure 4.3.9 (a). The mean value of the rotation frequency was  $f_{mean} = 9.3 \text{ Hz}$ . A sensor particle was trapped in the second tweezer of equal laser power at a distance of  $1.5 \mu\text{m}$

from the source trap. The frequency spectrum of the detector can be seen in Figure 4.3.9 (b). For this experiment, the frequency spectrum of the detector bead did not show any distinguished frequency, only white noise. Power and distance variations between the two optical tweezers did not change this outcome.

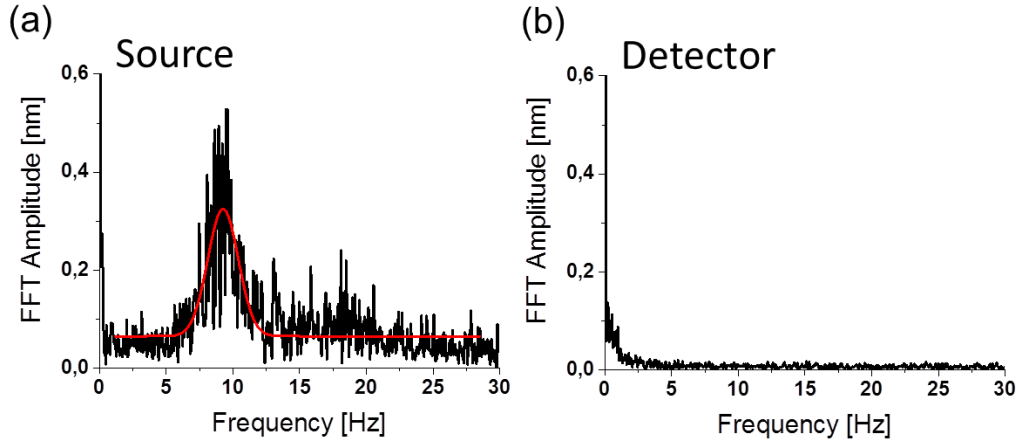


**Figure 4.3.9:** (a) Amplitude-frequency spectrum of a rotating microscREW trapped with a power of  $P = 127 \text{ mW}$ . The mean value of the rotation frequency was 9.3 Hz, evaluated from the Gaussian fit. (b) The frequency spectrum of the detecting microparticle trapped in the close vicinity of the screw did not show any distinguished frequency.

The reason why the sensor bead could not detect the frequency of the constantly rotating screw is that the source generated a smooth and steady velocity field. To study this field, we will first investigate the velocity field around a constantly rotating sphere (Figure 4.3.10). As described in Chapter 2.3, for a liquid with constant viscosity and constant density, the general Navier-Stokes equations can be simplified to the homogenous Stokes equations for steady laminar flow (equation 2.3.16). The flow velocity  $\mathbf{v}$  is then described by  $\nabla \mathbf{p} = \eta \nabla^2 \mathbf{v}$ , where  $\eta$  is the viscosity of the medium and  $\mathbf{p}$  represents the pressure. Taking into account no-slip boundary conditions, a particular solution for a rotating sphere in spherical coordinates is given by <sup>143</sup>:

$$\mathbf{v} = \omega \mathbf{e}_z \times r^3 \frac{\mathbf{x}}{|\mathbf{x}|^3} \quad (4.3.8)$$

with  $r$  being the sphere radius and  $\omega$  being the angular frequency. The velocity decay in the equatorial plane is inversely proportional to square of the radial distance  $x$  from the sphere center ( $\sim 1/x^2$ ). Most importantly, the velocity pattern of the flow is time-

independent. Inserting equation 4.3.8 into the Langevin equation for an optically confined particle (equation 2.2.15) leads to a fixed displacement of the detector bead within the harmonic potential<sup>15</sup> with an amplitude that depends on the angular rotation frequency  $\omega$  and on the radial distance  $x$  to the source.

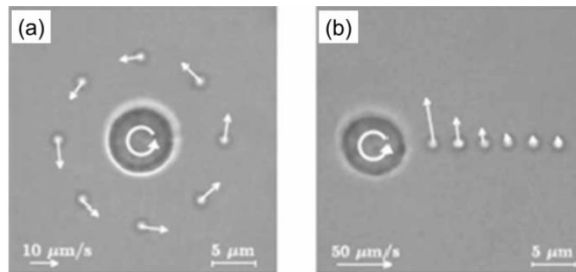


**Figure 4.3.10:** Visualization of the velocity field generated by a constantly rotating sphere. (a) Free particles orbit with a constant velocity at a fixed distance around the source. (b) Particles that orbit at distinct distances from the source illustrate the velocity decay in the equatorial plane. The velocity pattern of the flow is steady. (Taken from 145).

The example of a constantly rotating sphere can be transferred to the case of the rotating microscrew. The optically driven helix generates a smooth vortex around itself that leads to a fixed displacement of the detector bead from its equilibrium trapping position. As soon as the source stops to rotate, the flow sensor goes back to its equilibrium position. Thus, no oscillation will be detected and no amplitude in the frequency domain is obtained.

However, if the rotation frequency is modulated in a periodic time-dependent way, an alternating velocity field around the screw should be detectable (cp. Chapter: Microscale mapping of an oscillatory flow). For the experimental realization of this idea, a modulation of the power of the source trap was implemented. To do this, a glass cover slide was half sputtered with gold palladium (AuPd) and brought into the beam path of the trapping laser and rotated at a controlled frequency.

Without rotating the cover slip, we can investigate both cases. When the beam propagated through the glass side of the cover slide, the beam had a power of  $P_1 = 102 \text{ mW}$

<sup>15</sup> Thermal fluctuations neglected.

---

(Figure 4.3.11 (a)), while a propagation through the AuPd covered side resulted in an attenuated power of  $P_2 = 63 \text{ mW}$  (Figure 4.3.11 (c)).

A rotating screw, i.e. with the head pointing downwards was trapped with both powers. The time-dependent x-position of the center-of-mass of the screw was tracked and is shown for the first two seconds in Figure 4.3.11 (b, upper panel) for the higher laser power  $P_1$  and in (d, upper panel) for the lower trapping power  $P_2$ . FFT analysis of the time-dependent x- and y-position revealed the amplitude-frequency spectra of the helix for both directions. The total amplitude was calculated as described above. For the trapping laser power  $P_1$ , the mean screw rotation frequency was  $f_{max}(P_1) = 13.7 \text{ Hz}$  (Figure 4.3.11 (b), lower panel). When the substrate was turned azimuthally around  $180^\circ$ , the laser beam propagated through the AuPd side leading to a mean screw rotation frequency of  $f_{min}(P_2) = 6.3 \text{ Hz}$  (Figure 4.3.11 (d)). In the following experiment, the substrate was driven by a motor with a constant frequency  $f_{mod}$  up to  $60 \text{ Hz}$  (Figure 4.4.11 (e)). Since the glass substrate was half covered with AuPd, it was expected that a constant rotation of the substrate leads to an average screw rotation frequency of

$$\langle f_{av} \rangle_t = \frac{f_{max} + f_{min}}{2} \quad (4.3.9)$$

In this example, the driving frequency of the motor was  $f_{mod} = 20 \text{ Hz}$ . The time-dependent x-displacement of the center-of-mass of the screw can be seen in the upper panel of Figure 4.3.11 (f) and the amplitude-frequency plot for the screw rotation is shown in the lower panel. The amplitude-frequency plot for the microhelix motion revealed now two frequencies.

First, the average rotation frequency  $\langle f_{av} \rangle_t$  with a mean value of  $10.3 \text{ Hz}$ . This value fits very well with the expected one of

$$\langle f_{av} \rangle_t = \frac{f_{max} + f_{min}}{2} = \frac{13.7 \text{ Hz} + 6.3 \text{ Hz}}{2} = 10 \text{ Hz}. \quad (4.3.10)$$

Second, the frequency with which the power was modulated  $f_{mod} = 20 \text{ Hz}$ .

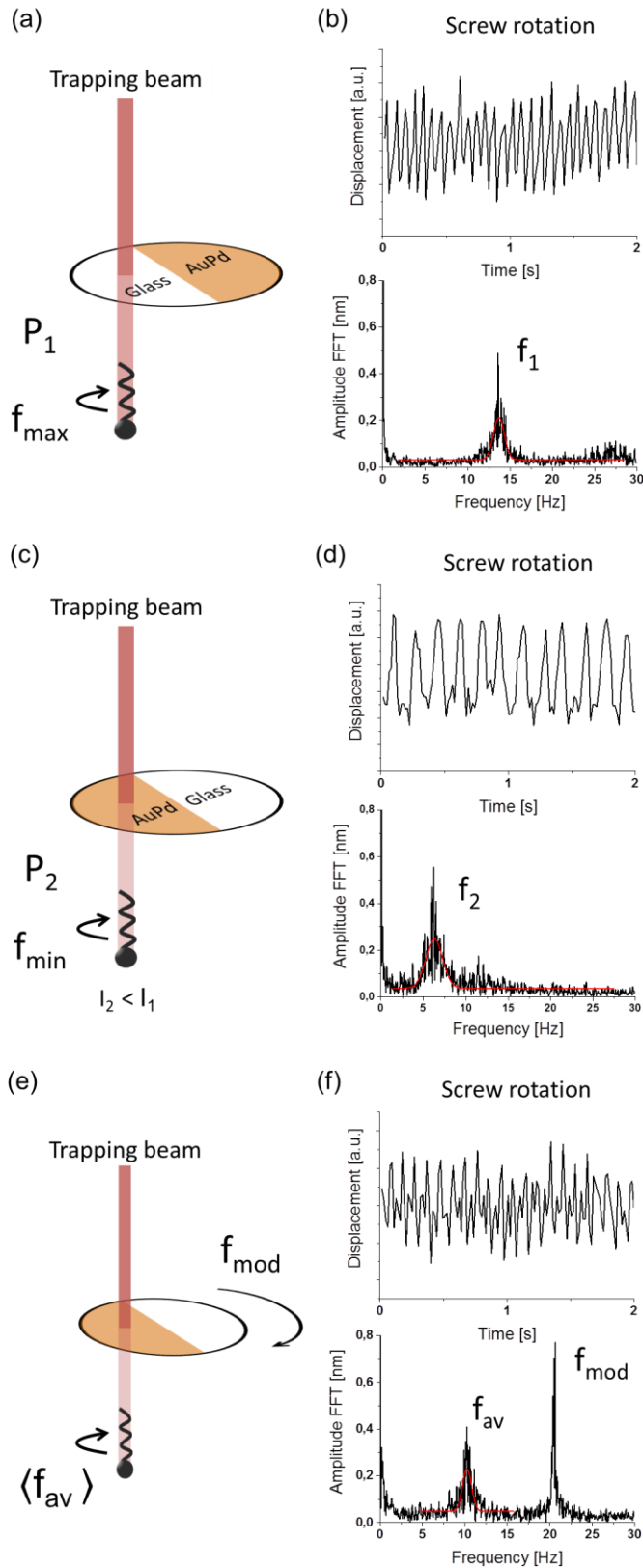


**Figure 4.3.11:** Sketch of the setup and analysis of the screw motion. (a) A glass cover slide was half spattered with AuPd and brought into the beam path of the trapping laser of the screw. The beam propagates through the glass side of the substrate and has a trapping power  $P_1$ . (b) Upper panel: Position versus time for the seconds 0 till 2 (x-direction). Lower panel: Amplitude-frequency plot of the screw motion with a mean screw rotation frequency of  $f_{\max}(P_1) = 13.7 \text{ Hz}$ . (c) The substrate is turned  $180^\circ$ . The beam passes the AuPd side. This leads to a lower trapping power for the source  $P_2$ . (d) x-position versus time for the screw motion (upper panel) and frequency spectrum of the source (lower panel) with a mean screw rotation frequency of  $f_{\min}(P_2) = 6.3 \text{ Hz}$ . (e) The substrate could be constantly driven by a rotor at a frequency  $f_{\text{mod}}$ . A constant rotation of the substrate leads to an average screw rotation frequency. (f) The time-dependent x-displacement of the center-of-mass of the screw can be seen in the upper panel and its frequency spectrum in the lower panel. The spectrum of the source revealed now two frequencies for the screw rotation. First, the average screw rotation frequency and second the frequency with which the intensity was modulated. In this case  $f_{\text{mod}} = 20 \text{ Hz}$ .

---

When the screw rotation is optically alternated with  $f_{mod}$ , the source, i.e. the screw, generates an oscillatory velocity field and the frequency of modulation  $f_{mod}$  is expected to be detectable with an optofluidic detector particle trapped in the close vicinity (Figure 4.3.12 (a)).

Thus, in the following, a detector particle was optically confined with a power of  $P = 26 \text{ mW}$  and brought close to an optically driven screw with a center-of-mass distance of  $2.3 \text{ }\mu\text{m}$  (Figure 4.3.12 (b)). The experimental parameters for the optically induced screw rotation were as described above, with

$$P_1 = 102 \text{ mW}, P_2 = 63 \text{ m}, f_{max}(P_1) = 6 \text{ Hz}, f_{min}(P_2) = 4.2 \text{ Hz}, f_{mod} = 20 \text{ Hz}.$$

The amplitude-frequency spectrum of the screw rotation, as described above and for reference can be seen in Figure 4.3.12 (c). As a next step the amplitude-frequency plot for the center-of-mass motion of the microfluidic detector has been determined (Figure 4.3.12 (d)). Notably, the motion of the optomechanical sensor was precisely following the modulation frequency  $f_{mod} = 20 \text{ Hz}$  with which the screw rotation was modulated.



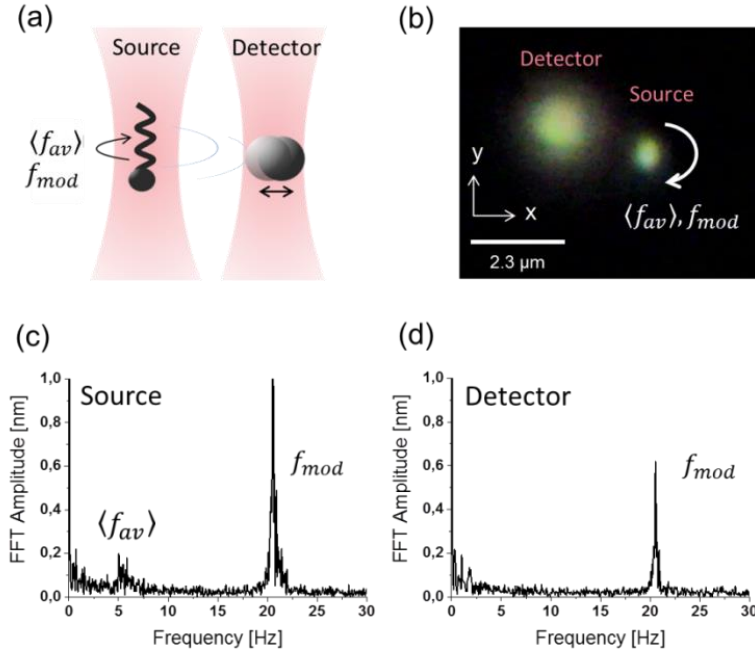


**Figure 4.3.12:** (a) Sketch and (b) dark-field image of a SiO<sub>2</sub> bead trapped next to an optically driven screw with a center-of-mass separation distance of 2.3 μm. The amplitude-frequency spectrum of the screw motion can be seen in Figure (c). The screw shows the expected average screw rotation frequency with a mean value of  $\langle f_{av} \rangle_t = 10.3$  Hz, along with the modulation frequency  $f_{mod} = 20$  Hz. The amplitude-frequency plot for the microfluidic detector is shown in Figure (d). As expected optomechanical sensor could pick up the modulation frequency at  $f_{mod} = 20$  Hz.

In the next step, the modulation frequency  $f_{mod}$  of the screw rotation was varied from 6 Hz to 20 Hz (with the same experimental parameters). The time-dependent x- and y-position of both, the detector and the screw were analyzed and the time series were Fast Fourier Transformed as described above (cp. Chapter 3.6). In Figure 4.3.13, the total amplitude  $A(f_{mod})$  is plotted versus the modulation frequency  $f_{mod}$  for a typical measurement. The black squares represent the amplitude obtained from a direct observation of the screw  $A(f_{mod})_{Source}$  and the red dots show the amplitude measured by the sensor particle  $A(f_{mod})_{Detector}$ . The detector had a center-of-mass distance of 2.3 μm to the source. It can be seen that with increasing modulation frequency  $f_{mod}$ , the amplitude  $A(f_{mod})$  in the Fourier spectrum of both, the source and the detector decreased. The slope of decrease for the source is more significant than for the detector and has a local minimum at  $f_{mod} = 13$  Hz. This amplitude-frequency dependence was seen in all measurements with the same experimental settings. The ratio between the amplitude measured by the detector  $A(f_{mod})_{Detector}$  and the amplitude obtained from the

direct investigation of the source  $A(f_{mod})_{Source}$  was found to be within the range of  $0.25 < \frac{A(f_{mod})_{Detector}}{A(f_{mod})_{Source}} < 0.6$ . This finding allows an estimation of the sensitivity of the detector bead and it is foreseen that the detector can follow higher modulation frequencies more efficiently.

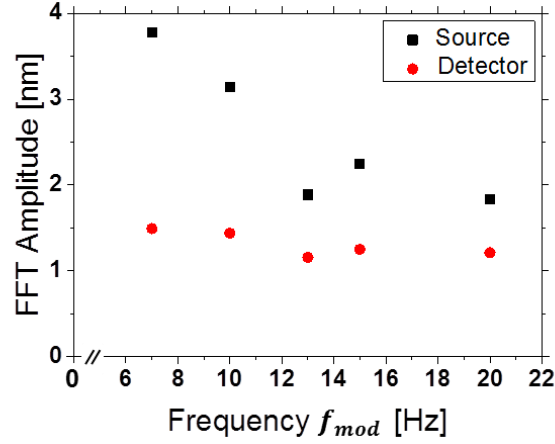


**Figure 4.3.13:** Amplitude  $A(f_{mod})$  versus modulation frequency  $f_{mod}$  for a single measurement. The modulation frequency  $f_{mod}$  was varied from 6 Hz to 20 Hz. With increasing  $f_{mod}$ , the amplitude in the Fourier spectrum of the source and the detector decreases, with a local minimum at  $f_{mod} = 13$  Hz.

Besides a variation of the modulation frequency, position-dependent measurements were also conducted. For that, a detector particle was trapped with a power of  $P = 127$  mW and positioned at four distinct center-of-mass distances to the source:  $D1 = 1.4$   $\mu\text{m}$ ,  $D2 = 2.8$   $\mu\text{m}$ ,  $D3 = 3.3$   $\mu\text{m}$  and  $D4 = 5.3$   $\mu\text{m}$  (Figure 4.3.14). The microhelices were driven optically with  $P_1 = 98$  mW and  $P_2 = 53$  mW. The average mean value of the maximum frequency of the screw rotation was  $f_{max}(P_1) = 10$  Hz and of the minimum frequency  $f_{min}(P_2) = 4$  Hz. This led to an average screw rotation frequency of  $\langle f_{av} \rangle_t = 7$  Hz. In a first experiment, the power of the source trap was modulated at  $f_{mod} = 5$  Hz.

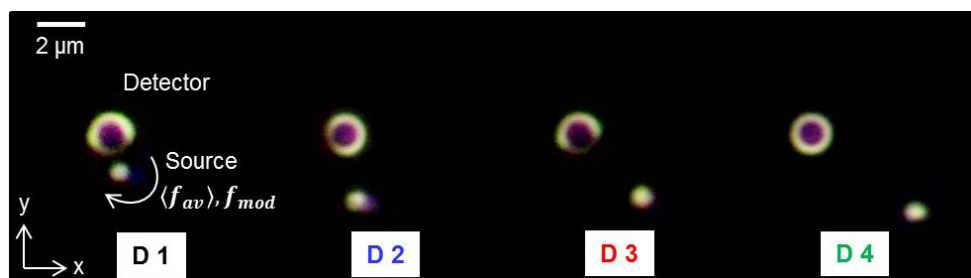


**Figure 4.3.14:** Dark-field image sequence of a position-dependent measurement of the flow around an optically driven microhelix (Source). A detector particle was positioned at four distinct distances to the source:  $D1 = 1.4 \mu\text{m}$ ,  $D2 = 2.8 \mu\text{m}$ ,  $D3 = 3.3 \mu\text{m}$  and  $D4 = 5.3 \mu\text{m}$ . The source followed the driving frequency  $f_{mod}$  and showed an average rotation frequency  $\langle f_{av} \rangle_t$ .

In figure 4.3.15 (a), the amplitude  $A(f_{mod} = 5 \text{ Hz})_{Detector}$  measured by the detecting particle is plotted versus the distances D1- D4. With increasing radial distance from the source, the magnitude of the time-dependent flow field decreased and finally vanished. At the distance D4, no signal was detected by the optofluidic sensor.

For the four distances D1- D4, the modulation frequency  $f_{mod}$  of the screw rotation was varied from 5 Hz to 10 Hz (figure 4.3.15 (b)). For the distances D1 and D2, the same tendency as described above occurred: with increasing modulation frequency  $f_{mod}$ , the amplitude  $A(f_{mod})_{Detector}$  decreased. A local minimum was present at  $f_{mod} = 6 \text{ Hz}$ . For the distance D3, the amplitude  $A(f_{mod})_{Detector}$  is already very low and it is difficult to draw conclusions about the behavior for increasing modulation frequencies.

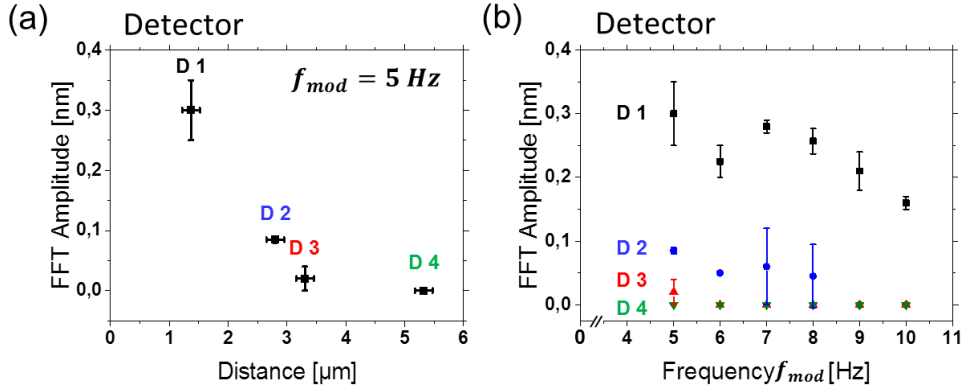


**Figure 4.4.15:** (a) The screw rotation was modulated with  $f_{mod} = 5 \text{ Hz}$ . The amplitude  $A(f_{mod} = 5 \text{ Hz})_{Detector}$  obtained from the frequency spectrum of the detecting particle is plotted versus its distance to the source (D1-D4). It can be seen that with increasing distance, the amplitude decreases. (b) The modulation frequency  $f_{mod}$  was varied from 5 Hz to 10 Hz for the four distances to the source. For the distances D1 and D2, the amplitude  $A(f_{mod})_{Detector}$  decreased with increasing modulation frequency and a local minimum was present at  $f_{mod} = 6 \text{ Hz}$ .

An explanation for the decrease of the amplitude in the frequency spectrum of the screw  $A(f_{mod})_{Source}$  and with this in the spectrum of the sensor particle  $A(f_{mod})_{Detector}$  with increasing modulation frequency  $f_{mod}$  could be that with increasing  $f_{mod}$ , the modulating excitation is not transferred instantaneously to the helix and thus a low efficiency of the flow field is obtained.

It can be expected that beyond a certain modulation frequency  $f_{mod,max}$ , the screw is not able to follow the modulation at all and the amplitude becomes zero, similar to a constantly rotating helix. Interesting is the observed local minimum that occurred at a certain modulation frequency (13 Hz or 6 Hz). For an in depths understanding of this finding, further power dependent experiments and simulations are performed that will help to identify this phenomenon.

### Chapter summary and outlook

This Chapter described the idea to use an optical tweezer to induce a light-driven rotation to microobjects with shape anisotropy in an aqueous environment. An optofluidic detection method has been established with an optically driven microhelix as source of flow. This colloidal, screw-like SiO<sub>2</sub> microstructure, with a diameter of 530 nm and a length of 2.35 μm, has been fabricated with the evaporation method *glancing angle deposition* (GLAD). A stable trapping in 3D of the microhelices could be obtained with their alignment parallel to the beam propagation direction. Once trapped in an optical tweezer, a rotation of a screw was observed in about 50 % of the experiments and occurred only, when the head was pointing downwards. The reason for the rotation is the radiation pressure exerted from the light on the helical structure. The non-isotropic azimuthal scattering of the photons at the chiral thread generates a torque on the body with the rotation direction of the microscrew being the same as the direction of its chirality.

The rotation frequency depends on the power of the trapping laser beam, and increases linearly with the laser power. Polarizability dependent measurements did not show any impact on the screw rotation frequency or direction in 3D.

The Reynolds numbers of the flow around a rotating microhelix were between 10<sup>-6</sup> and 10<sup>-4</sup> depending on the rotation frequency. In this low Reynolds numbers regime, the inertial forces are zero and a continuous torque must be transferred to the object to maintain its rotation. The optical torque on a microscrew trapped with a power  $P = 100 \text{ mW}$  at a wavelength  $\lambda = 1064 \text{ nm}$  is on the order of  $\tau_z \cong 1 \cdot 10^{-17} \text{ Nm}$ . The optically induced torque on the body is in equilibrium with the viscous drag torque acting on the rotating helix.

A constantly rotating screw generated a time-independent velocity field around itself, which led to a constant displacement of a trapped particle. A time-dependent modulation had to be induced to the rotation of the microhelix, creating an alternating velocity field around the helix. The frequency of modulation was detectable by an optofluidic sensor. The modulation frequency was varied and position-dependent measurements of the flow around the source were conducted. A decrease in the amplitude in the Fourier spectrum of

---

the helix as well as of the detector particle with increasing modulation frequency was observed.

As a future approach, it is of high interest to analyze the synchronization of multiple rotating microhelices which are trapped in line by means of holographic tweezers. Hydrodynamic coupling of parallel trapped microscrews has been already predicted theoretically<sup>83, 146</sup> and would be a straight forward experiment.

Since the fabrication method of the micropropellers is not restricted to a certain material, nanohelices could also be made out of gold. An investigation of their optical properties by spectroscopy and a simultaneous optical confinement would allow new fundamental insights to plasmonic nanostructures.

Moreover, the use of such microscrews as tiny drilling machines can be envisaged. The GLAD method allows a modulation of the surface character of the helices. A headless rotating screw with a lipid-favorable surface in an optical tweezer could be drilled into a cell membrane, paving path for a new approach for drug delivery and DNA transport into a living cell.

#### 4.4 Sensing the microfluidic flow generated by a single bacterial cell

The dynamic behavior of bacterial cells is of great interest for microbiology and nanomedicine. Research on the physical properties as well as locomotion strategies of living microorganisms began more than one hundred years ago. In his work „Über die Sichtbarmachung der Geisseln und die Geisselbewegung der Bakterien “ from 1909, the optician *Karl Reichert* reported the attempt to visualize bacterial appendages by means of dark-field microscopy<sup>63</sup>. However, a single filament has a diameter of just 20 nm (cp. Chapter: 2.4) and the flagella bundle is therefore hard to resolve under dark-field illumination (Figure 4.4.1). This hampers a detailed and direct investigation of the dynamic behavior of bacterial appendages<sup>64, 63</sup>. Experimental remedial measurements for this problem have been established. For example, reducing the speed of motion of the investigated bacterium<sup>101</sup> or labeling of the filaments with fluorescent dyes<sup>65, 66, 84</sup> or nanoparticles<sup>102</sup>. For the investigation of bacterial dynamics, either the swimming behavior of whole cells can be investigated<sup>69, 86</sup> or the rotation of individual flagella can be directly observed due to labeling<sup>65</sup>.

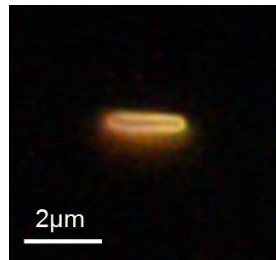


**Figure 4.4.1:** Dark-field image of a bacterial cell (*B. Subtilis*) taken through a 100x/NA=1.0 water dipping objective. The rod-shaped cell body can be seen precisely whereas the filaments cannot be resolved without fluorescent labeling or staining. The body had an average length of 2  $\mu\text{m}$  and an average width smaller than 1  $\mu\text{m}$ .

In 1987, *Arthur Ashkin* used optical tweezers for the manipulation of single cells<sup>67</sup>. Since then, optical trapping of individual microorganisms has become a powerful tool to spatially confine them<sup>66</sup>. One reason is that the method is less invasive than other approaches, for example, the mechanical immobilization of a cell on a solid support<sup>77</sup>. Optical trapping of a microorganism allows for the observation of bacterial chemotaxis and viability by directly investigating the movement of cell in the trap<sup>66, 147-150</sup>.

---

The focus of this Chapter is to find an alternative approach to the direct observation of a cell for the analysis of its bacterial motility. This would overcome the hindrance of fluorescent labeling or any other kind of cell modulation. The underlying idea is the measurement of the microfluidic flow generated by an optically confined bacterium by means of a sensor particle that is trapped in a second trap in the close vicinity (Figure 4.4.2). This approach is the extension to the work presented in the previous Chapter to a living organism.

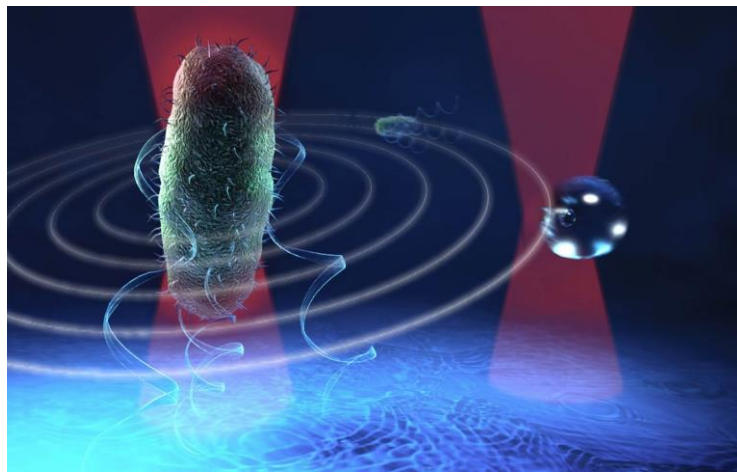


**Figure 4.4.2:** Sketch of the experimental concept for the measurement of the microfluidic flow generated by a trapped bacterium. A microparticle is optically confined in a second optical trap in the close vicinity and used as optofluidic sensor.

In this thesis, it has been demonstrated, for the first time, that the nanoeear approach can be extended and applied to study the microflow dynamics generated by a single bacterium at the nanoscale. In the first part of this Chapter, the dynamic properties of a bacterial cell in an optical tweezer are characterized. To this aim, two different strains of bacteria were optically confined and their motion behavior was investigated by direct observation. In the main part, the flow field around the living microorganism is analyzed by optical tracking of an optofluidic sensor. Finally, the Chapter is concluded and future perspectives as well as applications are discussed. This Chapter is based on my paper published in *Appl. Phys. Lett.* <sup>151</sup>.



### Characterization of a trapped bacterial cell by direct observation

A gram-positive, rod shaped bacterium (*Bacillus subtilis*) with a body length of approximately 2  $\mu\text{m}$  and a diameter of less than 1  $\mu\text{m}$  was kept in a chemotaxis medium and chosen as microbiological source of flow (see Figure 4.4.1). Once trapped in an optical tweezer, the bacterium was immobilized by the optical forces of the focused beam and the cell body aligned parallel with the beam propagation direction (Figure 4.4.3).

Two different strains of *B. subtilis* were tested<sup>16</sup>. The first strain was *BM77* (Figure 4.4.3 (a)), a strain that exhibited peritrichous flagellation and could perform chemotactic response (cp. Chapter: 2.4). This means that when the bidirectional motors of the filaments rotated in their default counter-clockwise (CCW) direction, the bacterial cell was in its “running” state. In this state, all filaments of the cell are synchronized in a helical bundle. It rotates CCW to push the bacterium in a certain direction<sup>72, 78</sup>. The bundle rotation has a certain frequency  $\omega$  and creates a strong torque that is balanced by viscous drag. The cell body counter-rotates with a certain frequency  $\Omega$ <sup>38</sup>. In the trap, the thrust generated by the flagellar rotation is balanced by the optical forces acting of the cell. High motility of the bacillus was essential for the measurements of the flow which was generated by the dynamics of the bacterium in its surrounding medium.

The second strain was *BD3458* (Figure 4.4.3 (b)), a non-flagellated bacterium<sup>92</sup>. Lacking flagella, this bacterium was solely subjected to diffusion in the chemotaxis medium and to directed diffusion within the optical trap. The *BD3458* strain was used for control measurements.

---

<sup>16</sup> The protocol for the bacterial cell preparation as well as a detailed description of the chemical composition of the chemotaxis medium can be found in Chapter 3.2.

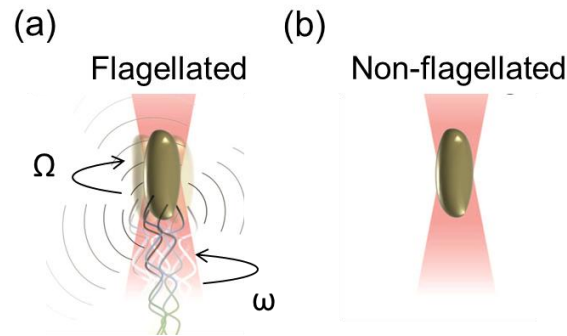


**Figure 4.4.3:** Schematic of a flagellated (a) and a non-flagellated (b) *B. subtilis* in an optical tweezer. (a) The bundle rotation with frequency  $\omega$  creates a strong torque that needs to be outbalanced by viscous drag due to counter rotation of the cell body ( $\Omega$ ). (b) The bacterium lacks appendages and is therefore solely subjected to directed diffusion within the harmonic potential.

An individual bacillus cell was trapped with laser powers between  $P_{min} = 25$  mW and  $P_{max} = 40$  mW at a trapping wavelength of  $\lambda = 1064$  nm. The beam was focused by a  $100\times/NA = 1.0$  water-immersion objective. Under dark-field illumination, the backscattered light of the vertically trapped cell body showed precisely its profile (Figure 4.4.4).

For the direct analysis of the body movement in the optical trap, a video file was captured with a high speed camera (PCO.dimax) at a frame rate of 500 Hz. Center-of-mass tracking of the body cross section in each frame of the video file revealed the time-dependent displacement of the cell body for the x- and y-direction (cp. Chapter: 3.6).

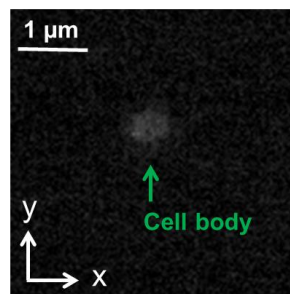


**Figure 4.4.4:** Under dark-field illumination, the backscattered light of the vertically trapped cell body showed precisely its profile. For the direct analysis of the body motion, a video of the optically confined cell was captured. Center-of-mass tracking of the body cross section in each frame of the video revealed the time-dependent displacement of the cell body for the x- and y-direction.

The  $x$ - and  $y$ -displacement of the cell body as a function of time are shown in Figure 4.4.5. The two bacterial strains showed a different behavior in the optical trap: A periodic precession of the long body axis around the tweezer axis with a frequency  $\Omega \sim 4$  Hz was observed for the flagellated strain BM77 (Figure 4.4.5 (a)). FFT of the time-dependent  $x$ - and  $y$ -displacement showed a mean value of the body rotation frequency at  $\Omega \sim 4$  Hz over a range of 120 Hz (not shown here). This implicates that from a direct observation of the cell body, only the body rotation frequency but not the flagella rotation frequency could be extracted.

The typical time series of the time-dependent position of a non-flagellated bacterial cell (BD3458) can be seen in Figure 4.4.5 (b). The cell body did not show any movement except for Brownian motion within the optical trap.

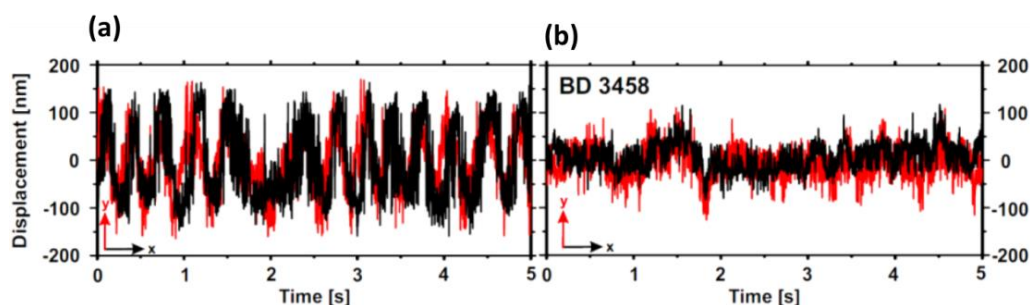


**Figure 4.4.5.** Direct analysis of a (a) flagellated (BM77) and a (b) non-flagellated (BD3458) bacillus in an optical trap (black: time-dependent displacement in  $x$ -direction, red: time-dependent displacement in  $y$ -direction). A periodic body rotation around the long axis of the bacterial cell with a frequency of  $\Omega \sim 4$  Hz was observed for the flagellated cell (a). No periodic motion of the cell body was observed for a non-flagellated bacterium, only Brownian motion (b).

It is reported in literature that for *Escherichia coli*, the bundle rotation frequency  $\omega$  is at the order 100 Hz and the subsequent cell body rotation frequency  $\Omega$  at the order of 10 Hz<sup>66</sup>. The average cell body rotation frequency of the flagellated bacilli investigated in this work was  $\Omega_{av} \sim 4$  Hz. For such a body rotation frequency a flagella rotation frequency of below 100 Hz can be expected. However, a direct observation is not possible. In the next Chapter, it will be shown how an optofluidic sensor can be utilized for a highly sensitive detection of the flagellar rotation frequency  $\omega$  of the bacillus.

---

### Microfluidic characterization of a trapped bacterial cell

The main goal of this work is the investigation of the dynamic properties of a single *B. subtilis* by its microfluidic characterization. This is experimentally realized by a microparticle (detector) that is trapped next to an optically confined bacterium (source). Therefore, a dual optical tweezers configuration at a wavelength of  $\lambda = 1064$  nm was set up in a dark-field microscope (cp. Chapter: 3.1.1.2). The two parallel beams were focused by a 100x/NA=1.0 water immersion objective and had a power of  $P = 30$  mW each. A single bacillus and a silicon dioxide ( $\text{SiO}_2$ ) particle with a diameter of  $D = 1.76$   $\mu\text{m}$  were trapped next to each other at a predefined distance of approximately 2  $\mu\text{m}$  (Figure 4.4.6 (a)). The body of the bacterium trapped with the first beam and the  $\text{SiO}_2$  bead in the second trap were aligned at approximately the same height, since the foci of the two trapping beams were on the same plane in z-direction.

The motion of the source and the detector were recorded via their white light Rayleigh scattering with a high-speed camera (PCO.dimax) at a frame rate of 500 Hz. Analyzing the time-dependent x- and y-position of the sensor particle inside the detector trap rendered it possible to detect the flow around the trapped bacterium. FFT of the detector time series resulted in amplitude-frequency plots in the x- and y-direction. The amplitude  $A(FFT_i)$ ,  $i = x, y$  was calculated using equation 3.6.5. For the final analysis of the detector movement, the total amplitude as described by equation 3.6.4 was used to achieve a better signal to noise ratio in the frequency spectrum.

The overall amplitude-frequency spectrum of a  $\text{SiO}_2$  bead trapped next to flagellated *B. Subtilis* can be seen in Figure 4.4.6 (b). It shows a distinguished frequency at 62 Hz. This frequency was present in all detector Fourier spectra when the sensor was trapped next to a bacillus that possessed appendages. A trapped bacterium generated an oscillatory microflow in its surrounding medium when it tried to swim out of the optical tweezer, which was then detected by the optofluidic sensor. Since the optical traps were aligned next to each other, a directionality of the hydrodynamic interaction between the trapped bacterium and the detector bead would be expected. A clear directionality, however, was not observed under given experimental conditions and a frequency at 62 Hz was almost always obtained in both the x- and y-direction.

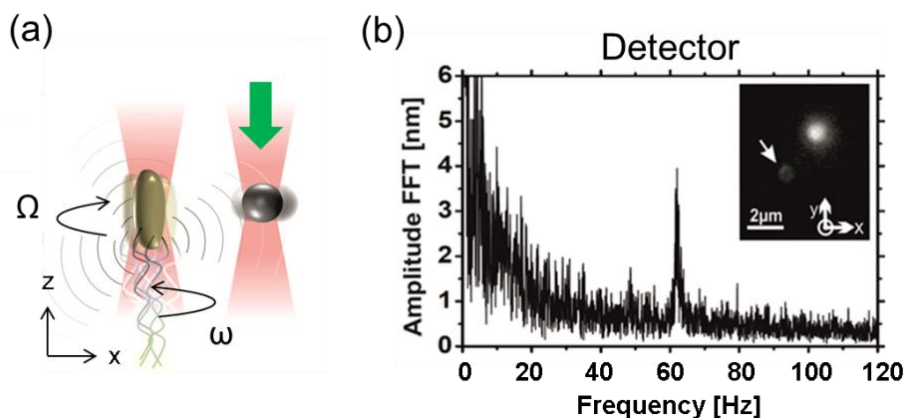


**Figure 4.4.6:** (a) Schematic of the experimental approach for the microfluidic characterization of a flagellated bacterium. A single bacillus and a sensor particle are trapped next to each other at a fixed distance. Microfluidic oscillations are generated as the bacterium tries to swim out of the optical tweezer and propagate into the surrounding medium. The waves are then detected by the silica particle optically confined in the close vicinity. (b) Amplitude-frequency spectrum of a detector particle trapped next to a single, flagellated *B. Subtilis*. A clear peak at 62 Hz was observed. Inset: Dark-field image of a trapped bacillus (white arrow) next to an optically confined detector particle.

Next, control measurements with non-flagellated bacilli were performed to verify that the detected frequency resulted from the movement of the flagella (Figure 4.4.7 (a)). A typical amplitude-frequency plot of a detector bead obtained when the sensor was trapped next to a non-flagellated bacterium is shown in Figure 4.4.7 (b). Only white noise could be observed over a range of 120 Hz. Thermal noise in the frequency spectrum of the detector was also seen when the bacterium was replaced by a second  $\text{SiO}_2$  particle. Without any external oscillatory source, the movement of the detector particle in the trap was solely subject to directed Brownian motion (see Chapter: 2.2)<sup>152, 153</sup>. This affirms that the amplitude at 62 Hz in the frequency spectrum of the sensor was indeed specific from the flagellated bacillus and did not result from background vibrations or false signals induced by the environment or the experimental setup. The experiment was repeated and the results confirmed for over 30 (flagellated/non-flagellated) bacterial cells.

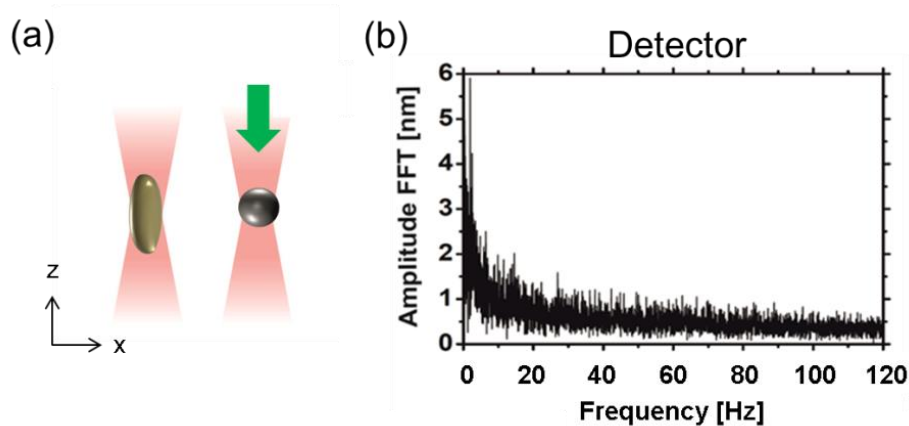


**Figure 4.4.7:** (a) Sketch of the control measurement with a bacillus that does not possess filaments. (b) The Fourier spectrum of the detector bead obtained when the sensor was trapped next to a non-flagellated cell showed only white noise over a range of 120 Hz.

The movement of a bacterium was analyzed directly by measuring the time-dependent position of the body center in the optical trap (Figure 4.4.8 (a)). Importantly, our measurement setup allows a simultaneous detection of the motion of the cell body (through the direct observation of its time-dependent x- and y-displacement) and of the rotation of the flagella (through the flow field detection by the optofluidic sensor). This allowed a careful analysis of the activity of the bacillus over different periods of time.

The direct measurement of the cell body movement of a trapped bacillus was compared to the measurement of its microfluidic flow by the detector particle. At the beginning of the measurement, the cell body rotated periodically with a frequency of  $\Omega = 4$  Hz. After 8 s, the bacterium stopped rotating and exhibited only random movement within the optical tweezer.

The corresponding amplitude-frequency spectrum of the detector particle in the second trap was analyzed for different time intervals starting at  $t = 4$  s to investigate how the amplitude at 62 Hz (flagella motion) is affected by changes in bacterial activity (Figure 4.4.8 (b)). The amplitude-frequency spectrum of the sensor between 4 s and 8 s showed a clear peak at 62 Hz which is attributed to the flagella bundle rotation. The filament rotation creates a torque causing a counter rotation of the cell body due to momentum conservation with  $\Omega \sim 4$  Hz (4 s - 8 s in Figure 4.4.8 (a))<sup>77</sup>. After 8 s, the

amplitude at 62 Hz dropped and even vanished at a later time interval (12 s – 16 s, Figure 4.4.8 (b)), which coincides with the visible change of the overall movement of the bacterium in Figure 4.4.8 (a).

Intriguingly, the signal at 62 Hz recovered between 12 s and 16 s although the cell body did not rotate during that time (Figure 4.4.8 (a)). This is a very important finding and correlates directly with the typical motion of a bacterium, as explained in the following.

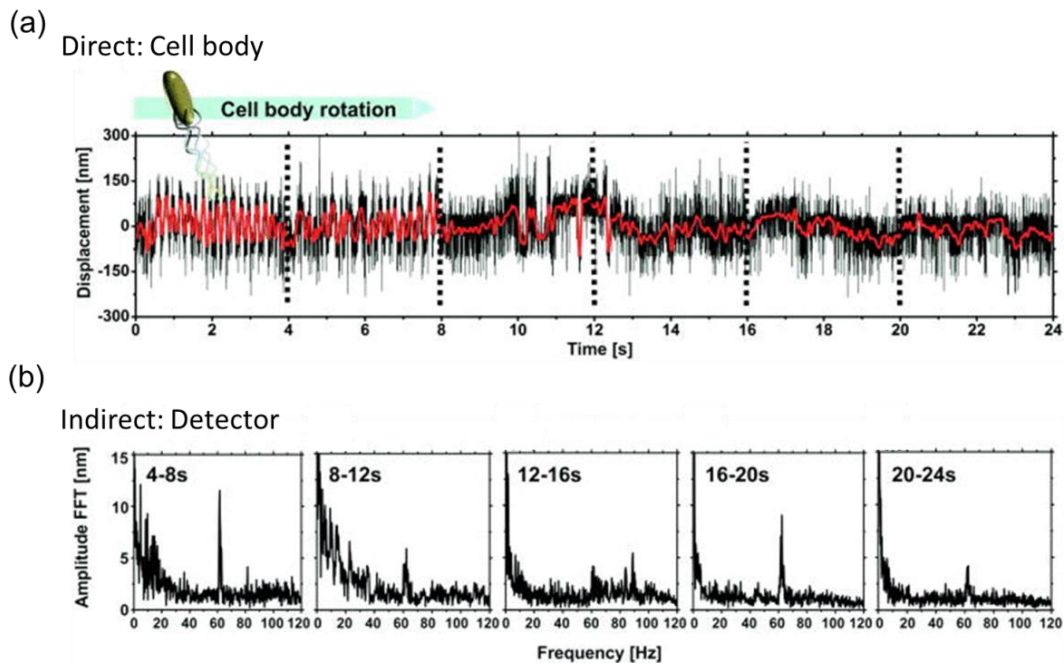


**Figure 4.4.8:** Comparison between the direct measurement of the cell body (a) and the corresponding frequency spectrum measured by the detector bead for different time intervals (b). (a) Observation of the time-dependent y-displacement of the flagellated bacterium in an optical trap for 24 s (black: measured data, red: fitted curve to guide the eye. The data was smoothed by a Savitzky-Golay filter of second polynomial order with 50 window points). A homogeneous rotation of the cell body of  $\Omega \sim 4$  Hz is observed during the first 8 s of the measurement. After 8 s the cell stopped rotating and started to move randomly in the optical trap. (b) Corresponding amplitude-frequency plots of the detector bead plotted for five different time intervals. A high peak at 62 Hz can be seen between 4s and 8s while the cell body rotates. Between 8 s and 12 s the amplitude was lower and correlates to a visible change of the cell movement. The peak intensity vanishes (12 s – 16 s) and recovers (16 s – 20 s) for different time intervals during the experiment. This hints at changes of the bacterial cell activity.

The “running” state of the bacillus corresponds to an active, forward directed movement of the cell where all flagella are bundled and the rotation of the bundle is synchronized in one direction. Between the first 8 s of the experiment (Figure 4.4.8 (a)), the rotation of the cell body indicated that the cell was likely in a running state. On the contrary, bacteria

---

can also undergo a tumbling motion if the flagella are not bundled together. In this case, the cell moves randomly, which allows them to reorient and change their swimming direction during chemotaxis (cp. Chapter **Error! Reference source not found.**). The flagella can still be active and rotate but no strong torque is created that would lead to a counter-rotation of the cell body. This would correspond to the observation of random motion in the direct experiment while there is still rotation of the flagella (8 s – 12 s).

“Tumbling” of bacteria is typically observed in the range of milliseconds which is clearly much shorter than the duration of the measurement shown in Figure 4.4.8. For *B. subtilis* it has been shown, however, that the tumbling behavior can be significantly altered and prolonged over a wide range between different bacteria strains to the extreme of chemotaxis mutants which are exclusively tumbling<sup>154, 155</sup>. At the same time, stress and possibly photodamage caused by the infrared trapping laser could also have an impact on the cell activity which could thereby cause a tumbling-like situation that is likely observed for the bacterium in Figure 4.4.8 (a) after 8 s<sup>149, 156-158</sup>. U. Mirsaidov et al. analyzed the effects of optical trapping on the viability of *E. Coli* exposed to near infrared laser beams. They found a decreasing viability of the cells with increasing laser power and exposure time<sup>157</sup>. Rasmussen et al. also reported that *B. subtilis* shows signs of physiological damage after a few minutes while being trapped with a  $\lambda = 1064$  nm laser at a laser power of only  $P = 6$  mW<sup>158</sup>. In the experiment shown here, a cell was trapped with a laser power of  $P = 30$  mW at the same wavelength. Under this condition, the bacillus motility and vitality could be altered due to photodamage, even after a few seconds, which could in turn manifest in a change of the cell movement. As a consequence, the flagella are not bundled anymore and some of the flagella might even stop rotating completely.

Taken together, our experimental approach allows a tracking of the cell body and flagella motion individually which enables an identification of different points of activity. An investigation of the cell body alone would not give any evidence to the cell vitality. A cell could be dead, and thus prone to Brownian motion, or in a tumbling state. The changes of the amplitude height corresponding to the flagellar rotation at  $\omega = 62$  Hz, and a recovery of the signal intensity illustrate the capability of this method to focus on different states of bacterial activity and to access otherwise hidden information.



The experimentally measured amplitude  $A$  ( $f = 62 \text{ Hz}$ ) of the detector bead inside the trap is directly related to the velocity of the surrounding water molecules  $v$ : The frictional drag coefficient  $\gamma$  for a spherical object is given by  $\gamma_{sphere} = 6 \pi \eta r$  (equation 2.2.11) with  $\eta$  being the dynamic viscosity of the medium and  $r$  being the particle radius. An insertion of this expression into the equation of motion for a particle confined in a trapping potential with trap stiffness  $\kappa$ :  $v_{particle} \gamma_{sphere} + \kappa A(f) = F(f)_{thermal}$  (equation 2.2.15) reveals the relation between flow velocity and maximal detector displacement at the frequency  $f = 62 \text{ Hz}$ :  $\kappa A = 6 \pi r \eta v$  (equation 4.2.9). Numerical simulations of the velocity field around a trapped bacillus were performed to find the regions with maximum flow velocity. Bacterial motion happens at very low Reynolds numbers due to their size in the micro- and nanometer range<sup>54, 159, 59, 60</sup> (cp. Chapter: 2.3). The Reynolds number of a bacterium with a characteristic length  $a$  at the microscale swimming with velocity  $V = 30 \text{ }\mu\text{m/s}$  through water with dynamic viscosity  $\eta = 10^{-3} \text{ Ns/m}^2$  is about  $10^{-4}$  to  $10^{-5}$ . The hydrodynamics are dominated by viscous drag<sup>59</sup>, and hydrodynamic interactions between individual filaments become substantial<sup>146</sup>, which is also considered as one of the physical causes for the formation of a flagella bundle<sup>160, 59</sup>. Therefore, in the simulations laminar flow of an incompressible fluid was assumed.

A simple model of a bacterial cell shown in Figure 4.4.9 (a) was used to qualitatively retrieve the main features of more complex models. The body of the bacterium was estimated as an ellipsoid with two semi-axis  $a_1 = 1.5 \text{ }\mu\text{m}$  and  $a_2 = 0.5 \text{ }\mu\text{m}$  rotating clockwise at either  $f_1 = 4 \text{ Hz}$  or  $f_1 = 0 \text{ Hz}$ . The counter-clockwise rotating filament bundle was assumed to be a cylinder with a height of  $h = 8 \text{ }\mu\text{m}$  and a radius of  $r = 0.1 \text{ }\mu\text{m}$  rotating at  $f_2 = 62 \text{ Hz}$ .

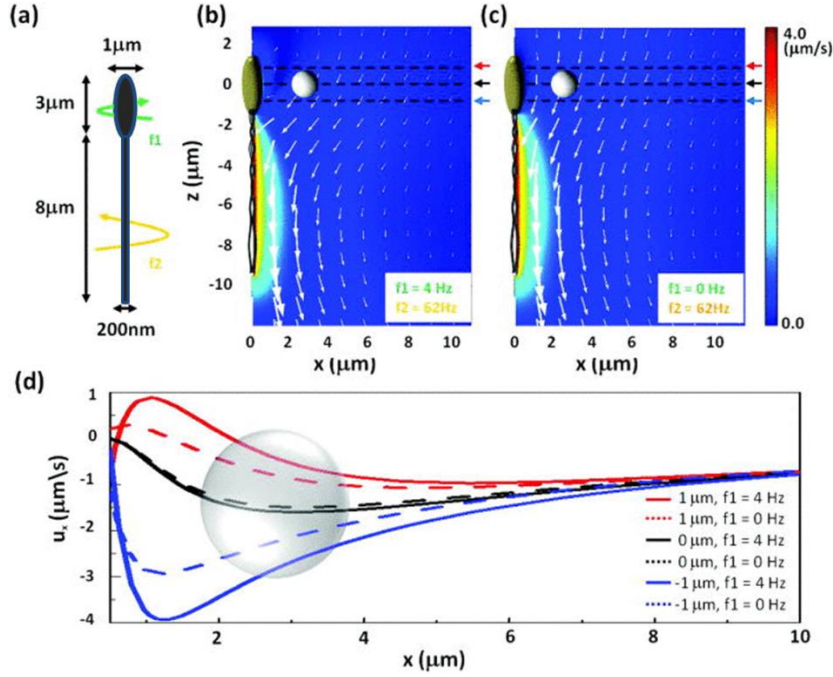


**Figure 4.4.9:** Finite elements simulation of the flow generated by a flagellated bacterium in an optical trap. (a) Schematic depiction of the bacterial cell model used for the simulations. (b) The color map depicts the velocity magnitude and the white arrows depict the direction of the velocity field for a body rotation frequency  $f_1 = 4$  Hz (clock-wise) and the frequency of the flagella bundle  $f_2 = 62$  Hz (counter-clockwise). The detector bead is sketched in a distance of  $2\mu\text{m}$  from the bacterium. (c) Color map of the velocity field of the flow generated by the bacterium for a body rotation frequency of  $f_1 = 0$  Hz and the frequency of the flagella bundle of  $f_2 = 62$  Hz. (d) x-component of the velocity field ( $u_x$ ) as a function of the distance ( $x$ ), for 3 different  $z$ -values. The solid lines represent the case  $f_1 = 4$  Hz (b panel) and dashed lines represent the case  $f_1 = 0$  Hz (c panel). The color code correspond to the arrows in panel (b) and (c). A schematic of a detector particle ( $D = 1.76 \mu\text{m}$ ) is shown at a distance of  $2 \mu\text{m}$ .

As a first approach, a stationary and axis-symmetric laminar flow was presumed to find regions with maximum velocity amplitudes around a trapped bacillus. The numerical simulations were performed with *COMSOL* solving the Navier-Stokes equations for laminar flow according to (cp. Chapter: 2.3.1.3):

$$\nabla \cdot \mathbf{v} = 0 \quad (\text{equation 2.3.6}) \quad \text{and}$$

$$\rho \left( \frac{\delta \mathbf{v}}{\delta t} + \mathbf{v} \cdot \nabla \mathbf{v} \right) = \mathbf{B} - \frac{\nabla p}{\rho} + \nu \nabla^2 \mathbf{v} \quad (\text{equation 2.3.15})$$

where  $\mathbf{v}$  denotes the velocity [m/s],  $\eta$  the dynamic viscosity of water ( $\eta_{\text{water}} = 0,001 \text{ Pa} \cdot \text{s}$ ) and  $p$  the pressure [Pa]. In the computation, the body force per unit mass  $\mathbf{B}$  was set to be zero.

The result of the simulation of the velocity field generated for both cases with and without cell body rotation is shown in Figure 4.4.9 (b) and Figure 4.4.9 (c), respectively. The velocity magnitude is illustrated by the heat map and the white arrows display the direction of the microfluidic flow generated by the whole cell as well as the magnitude according to the relative arrow thickness and length. As shown in Figure 4.4.9 (b), the field generated by the rotating bacterial body and the rotating bundle causes the fluid to flow inwards at the neck region (where the tail is connected to the body) and pushed outwards along the swimming direction of the bacterium. A detector particle is therefore likely to be sufficient to sense the flow of the flagella when the cell body and the particle are both aligned at approximately the same height. Although in reality the forward propulsion comes from the bundle acting as a rotating spiral, in the simulations we calculate the velocity field for the stationary flow around a bacterium simply modelled as two rotating cylinders with an imposed laminar flow<sup>82</sup>. The direction of the field obtained agrees with the observation that flagellated bacteria cells behave as hydrodynamic pushers<sup>59</sup>. These results were compared to numerical calculations of the field generated by the rotation of the flagella bundle only ( $f_l = 0$  Hz) in Figure 4.4.9 (c). In this case, the resulting field pointed mainly along the length of the cell body, while the net side-flow directed inwards became smaller. This corresponds to no movement of the cell. The velocity field in the x- and y-direction is also weaker which explains the drop in the amplitude height at 62 Hz for the measurement displayed in Figure 4.4.8 (b) (8 s – 24 s). The x-component of the velocity as a function of the particle position at the head region is shown in Figure 4.4.9 (d). Three different regions were compared: 0  $\mu\text{m}$ , which corresponds to the center of the bacterium body and the particle (black line, indicated by the black arrow in Figure 4.4.9 (b), (c)), 1  $\mu\text{m}$  which is above the center line (red line, indicated by the red arrow in Figure 4.4.9 (b), (c)), and -1  $\mu\text{m}$  which is below (blue line, indicated by the blue arrow in Figure 4.4.9 (b), (c)). As shown in Figure 4.4.9 (d), the strongest field is observed around 1.2  $\mu\text{m}$  away from the bacterium. Although the velocity pattern was, as a first approach, assumed to be steady, this is in good accordance with experimental observations. It was found that the flow field around the cell was still detectable when the detector particle was located 2  $\mu\text{m}$  away from the source. However, the amplitude at 62 Hz in the frequency spectrum of the sensor vanished at larger distances.

---

## Chapter summary and outlook

In this work, I have shown for the first time how the optical trapping of a bacterial cell (source) next to an optofluidic sensor enables to draw conclusions on the motion and activity of the bacterium with its own dynamics at the nanoscale.

A direct observation of the cell body displayed a rotational movement of the body in the active state, which goes hand in hand with the flagella rotation as revealed by the amplitude-frequency plot of the sensor bead. A tumbling state was characterized by Brownian motion of the directly observed cell body while flagella motion was still ongoing, as the flagella rotation was present in the frequency-amplitude map of the detector. A comparison with typical characteristics of the different cell states showed a great agreement with the experiment and demonstrates the applicability of our approach. A tumbling-like state of the bacterium could be confused with a dead cell when analyzing the cell body movement only. The capability of the optofluidic detection to focus on different states of bacterial activity and to access otherwise hidden information is a crucial finding of this work. Numerical simulations of the velocity field around a trapped bacillus were performed to find the regions with maximum flow velocity. Although the model for the simulation was simple, it supported the experimentally measured data well.

For the detection of a frequency within a microfluidic flow field by an optically confined sensor, the field has to have a periodic, time-dependent component. As a future approach it will be very interesting to investigate the physical origin of the oscillation of the velocity field around a bacterial cell. Direct analysis of the cell body movement indicated a precession of the body long axis around the tweezer axis. This oscillation of the body orientation in the optical trap could lead to a periodic alternation of the microfluidic field at the body rotation frequency which is in turn a consequence of the flagella bundle rotation. It is foreseen that the filament bundle itself undergoes a precession around the tweezer axis and therefore generates a time-dependent velocity field at 62 Hz. While the amplitude at 62 Hz could be seen clearly in the frequency spectrum of the sensor particle, an amplitude arising from the body rotation in the lower frequency range was hard to resolve due to  $1/f$ -noise. The steady flow field simulation showed a dependence of the flow direction around the bacterium on the body rotation. We envisage that the superposition of the flow field generated by the body rotation and the flow field generated by the filament bundle also lead to a time-dependent flow oscillation. A comparison of

fluorescence measurements of the flagellar rotation and the experimental approach presented here will give some information on the mentioned assumptions and paths the way for a final characterization of the microfluidic dynamics of individual bacterial cells.

The method, to detect the flagella rotation of bacterial cells by tracking the position of a particle in an optical trap, renders it possible to analyze the activity of a microorganism on a single cell level. Splitting the laser beam into multiple beams by the use of diffractive optics or a liquid crystal device can be furthermore employed to generate an array of detector particles <sup>161, 162</sup>.

The approach presented here can likely be extended to map and image the microfluidic oscillations generated by single prokaryotic or eukaryotic cells with high resolution by moving the detector bead around the cell or using multiple sensor particles at once.

Furthermore, it is of high interest to use holographic tweezers and trap an array of microscrews together with bacterial cells. The focus of investigation can then be the effect of hydrodynamic interaction between artificial and biological helical microobjects.



## 5. Conclusion and Outlook

Within this work, the successful implementation of an optofluidic sensor for the investigation of oscillatory flows generated by artificial or biological microobjects was demonstrated. Different methods for an optimal and highly sensitive characterization of microfluidic dynamics at a very small scale were established through the employment of multi-tweezers configurations. Thus, artificially created flow fields arising from a dipolar oscillating bead moving between two alternately chopped traps and from a rotating microhelix have been characterized and extended to analyze the motion behavior of living microorganisms such as a bacterial cell.

As a first approach, it has been shown for the first time how a single gold sphere can be used as an optofluidic nanosensor for the detection of microbiological dynamics. A freely swimming larva of Copepods served as living source of microfluidic oscillations. The extracted frequencies from the motion of the gold nanoparticle in the optical trap were in a very good agreement with those obtained through a direct observation of the larva motion. Thus, this approach delivered a tool to detect microfluidic dynamics produced by a living animal in the vicinity of the optical trap and enabled a non-invasive analysis of its motility. However, even if the trapping laser wavelength is off-resonant to the plasmon resonance of the gold nanoparticle, a finite heating of the nanoparticle occurs. This leads to an unwanted enhancement of thermal fluctuations in the system.

To increase the sensitivity of optofluidic detection, the idea to use a non-absorbing, dielectric microparticle as optofluidic sensor of oscillatory flows was introduced. For a precise description of a focused single beam gradient trap acting on a silicon dioxide microsensors, the Generalized Lorenz Mie theory was employed and the *T-matrix* method allowed a computation of the optical forces on the optofluidic detector. The vectorial velocity field around a silicon dioxide microparticle oscillating in a dipole-like mode in a home built, chopper based dual tweezers configuration was mapped by optical tracking of a twin sensor positioned at different points around the source. This sophisticated experiment was realized by setting up a multiple tweezers configuration at different

---

wavelengths allowing position-dependent measurements. Deviations between theory and experiment in particular in close distances between the detector and the source delivered an understanding to the effect that not only incompressible flow, but also acoustic waves contribute to the measured flow in the near-field. This is an important finding for optofluidic location and recognition experiments and might trigger further investigations in this direction, as conditions are reached which in normal circumstances are difficult to achieve. At small scales and low Reynolds numbers, laminar flow is dominant. Viscous forces that arise from shearing between velocity-isosurfaces dominate inertial forces, the main transport mechanism for mass is diffusion, and a mixing in the low Reynolds number regime is not easy to realize. Thus, an oscillatory microflow is a very useful approach to mix liquids in laminar systems. The introduced optofluidic method paves the way for in-situ characterization of fast mixing microscale devices and for new detection methods able to provide location and recognition of moving sources that can be applied to both artificial and living microobjects with own dynamics at the nanoscale.

A great part of this work was the development of a detection method for microfluidic flow fields generated by a trapped bacterial cell in its surrounding medium by means of an optomechanical sensor. For this aim and as a first approach, an optically confined and rotating microhelix was used to model the mechanical and dynamical properties of a living microorganism, e.g. a bacterium. An optical tweezer was used for initiating a light-driven rotation of chiral microobjects in an aqueous environment. The non-isotropic azimuthal scattering of the incident photons at the chiral thread created a torque on the body with a rotation direction of the microscrew being the same as the direction of its chirality. The Reynolds numbers of the flow around a rotating microhelix were between  $10^{-6}$  and  $10^{-4}$  depending on the rotation frequency. In this low Reynolds numbers regime, the inertial forces are zero and a continuous torque must be transferred to the object to maintain its rotation. The focus of investigation was the establishment of the optofluidic detection method with an optically driven microhelix as source of flow. A constantly rotating screw generated a time-independent velocity field around itself, which led to a constant displacement of a trapped dielectric microparticle. Therefore, a time-dependent modulation was induced to the rotation of the microhelix, creating an alternating velocity field around the helix, whose frequency of modulation was successfully detectable by an optofluidic sensor. The modulation frequency was varied and position-dependent measurements were conducted. The amplitude in the Fourier



spectrum of the detector particle decreased with increasing modulation frequency. For an in depths understanding of this finding further frequency-dependent experiments and simulations are performed. They will help to gain insight into the dependence of optofluidic sensing on the detected frequency.

Finally, in this work, I have shown for the first time how the optical trapping of a bacterial cell (source of oscillations) next to a dielectric microparticle (optofluidic sensor) enables to draw conclusions on the motion and activity of the bacterium with its own dynamics at the nanoscale. A direct observation of the cell body displayed a rotational movement of the body in the running state, which goes hand in hand with the flagella rotation as revealed by the amplitude-frequency plot of the optofluidic sensor bead. A tumbling state was characterized by Brownian motion of the directly observed cell body while flagella motion was still ongoing, detected in the frequency-amplitude map of the sensor. A comparison with typical characteristics of the two different cell states showed a great agreement with the experiment and demonstrates the applicability of our approach to living organisms. Moreover, in an analysis of the cell body movement alone, a tumbling-like state of the bacterium might be confused with a dead cell. The unique combination of direct observation of the bacterial cell motion with the optofluidic detection method addressing the flagella rotation was solely responsible for a successful identification of the two given states. The capability of the optofluidic detection to focus on different states of bacterial activity and to access otherwise hidden information is a crucial finding of this work. Numerical simulations of the velocity field around a trapped bacillus were performed to identify the regions with maximum flow velocity. As a first approach, in the simulations a stationary and axis-symmetric laminar flow was presumed. Although the model for the simulations was simple, it supported the experimentally measured data well. For the detection of a frequency within a microfluidic flow field by an optically confined sensor, the field has to have a periodic, time-dependent component.

As a future approach, the recognition of the physical cause of the time-dependent oscillation of the velocity field around a bacterial cell is planned to be experimentally addressed. From our measurements, the direct analysis of the cell body movement indicated a precession of the body long axis around the tweezer axis. This oscillation of the body orientation in the optical trap could lead to a periodic alternation of the microfluidic field at the body rotation frequency which is in turn a consequence of the

---

flagella bundle rotation. It is foreseen that the filament bundle itself undergoes a precession around the tweezer axis and therefore generates a time-dependent velocity field at 62 Hz. A comparison of fluorescence measurements of the flagellar rotation and the experimental approach presented here will allow conclusions and paves the way for a final characterization of the microfluidic dynamics of individual bacterial cells.

In summary, the experimental technique, presented in this thesis, breaks ground for an in depths understanding of the fundamentals of oscillatory microflows generated by an artificial or biological microobject and provides an alternative and sensitive method for the characterization of nanoscale dynamics. The approach to detect the flagella rotation of a bacterial cell by tracking the position of a particle in an optical trap renders it possible to analyze the activity of a microorganism on a single cell level without the necessity of observing the source directly.

A splitting of the laser beam into multiple beams by the use of diffractive optics or a liquid crystal device can be furthermore employed to generate an array of detector particles<sup>161, 162</sup>. We foresee the extension of the optofluidic detection method to map and image the microfluidic oscillations generated by single prokaryotic or eukaryotic cells with high resolution by moving the detector bead around the cell or using multiple sensor particles at once.

Furthermore, the use of holographic tweezers for the trapping of an array of microscrews and bacterial cells allows the investigation of the hydrodynamic interaction between the artificial and living objects on a very small scale. This experimental approach will deliver a more sophisticated understanding of hydrodynamic coupling between helical microbiological systems.

Taken together, this work gives a fundamental understanding on optofluidic detection possibilities based on multi-tweezers configurations and delivers a novel experimental approach for sensing the nanoscale dynamics of microorganisms.





## Appendix

The interested reader can find a more detailed description of the flow field measurement and the flow field simulations with a comparison between measured data and theory mentioned in the publication of S. Nedev et al. <sup>122</sup>.

To obtain the associated velocity field of the oscillatory flow from equation 4.2.9, the optical tweezer holding the detector was calibrated by the power spectral density procedure <sup>124, 125</sup> (cp. Chapters: Displacement of an optically trapped particle, Power spectrum of an optically trapped particle). For the x- and y-direction, the corner frequencies were

$$f_{c,x} = (603.6 \pm 7.9) \text{ Hz and}$$

$$f_{c,y} = (532.3 \pm 6.7) \text{ Hz.}$$

With  $f_c = \kappa/2\pi\gamma$  (equation 2.2.18), the corner frequencies yielded a trap stiffness  $\kappa$  for the corresponding directions with

$$\kappa_x = (6.73 \pm 0.25) \times 10^{-5} \text{ N/m and}$$

$$\kappa_y = (6.00 \pm 0.23) \times 10^{-5} \text{ N/m.}$$

They are consistent with reported values <sup>125</sup>.

Figure A I shows the velocity field of the measured signal (black arrows) with magnitude  $\|\mathbf{v}_{exp}\| = \sqrt{v_x^2 + v_y^2}$  and the direction defined by the angle  $\tan(\theta_{exp}) = A_y / A_x$  in the upper right quadrant with respect to the source. Corresponding error bars (of ~9%) calculated through the propagation of error are shown in grey. No phase lag was found between the source and the detecting bead. The maximum velocity fields correspond to ~250  $\mu\text{m/s}$ , a value of the same order of magnitude as the maximum velocity of the source bead e.g., ~500  $\mu\text{m/s}$ . Moreover, a strong signal was still detected when the detector bead was placed at  $(x,y) \approx (16,16) \mu\text{m}$ . The accuracy for the direction and magnitude of the velocity vectors was estimated to be ~3° and 3.5%, respectively

(from repeated measurements with the same detecting particle). The remaining quadrants (below and to the left) exhibited the same signal in a symmetric fashion within the experimental accuracy.

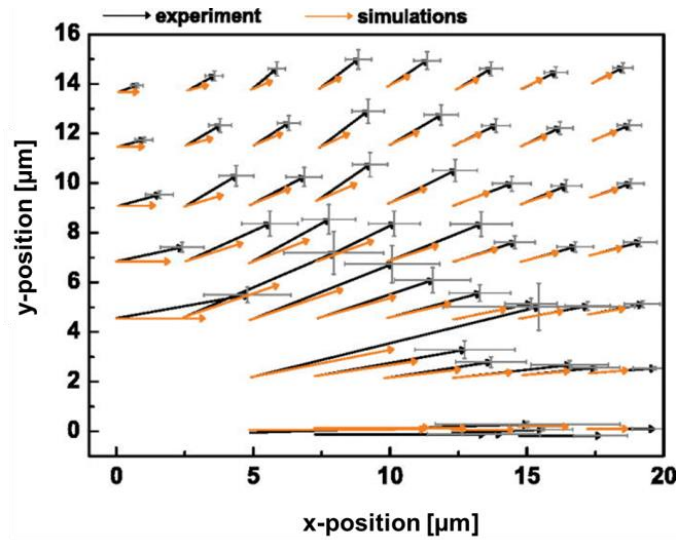


**Figure A I:** Velocity field of the measured signal (black arrows) in the upper right quadrant with respect to the source. The arrows contain information of both, the direction and the magnitude of the flow field. The corresponding error bars (of  $\sim 9\%$ ) calculated through the propagation of error are shown in grey. The experimentally obtained fluidic field is compared to the simulated field (orange arrows). (Taken from 122).

Simulations of the flow field surrounding the source were performed for a better understanding of the measurements and its main results. For frequencies  $100 \text{ Hz} < f < 200 \text{ Hz}$  and length scales as considered here, the hydrodynamic near-field around a vibrating source is primarily governed by incompressible flow<sup>163, 164</sup>. Therefore, the simulations of the velocity field around an oscillating microsphere were performed by solving the Navier-Stokes equations for an incompressible fluid.

In the simulations, the model of a rigid sphere oscillating along the  $x$ -axis according to  $x = A \sin(\omega t)$  was used. The radius  $r$  of the sphere, the amplitude  $A$ , and the frequency  $f$ , were set to the experimental values, and the velocity of the liquid surrounding the bead  $\mathbf{v}$  was evaluated at the same 60 experimental points, as shown in Figure 4.2.4. The detector bead was not included in the simulations. The numerical simulations were performed with *COMSOL* solving the Navier-Stokes equations for laminar flow according to (cp. Chapter: 2.3.1.3):

$\nabla \mathbf{v} = 0$  (equation 2.3.6) and

$$\rho \left( \frac{\delta \mathbf{v}}{\delta t} + \mathbf{v} \nabla \mathbf{v} \right) = \mathbf{B} - \frac{\nabla \mathbf{p}}{\rho} + \nu \nabla^2 \mathbf{v} \quad (\text{equation 2.3.15})$$

where  $\mathbf{v}$  denotes the velocity [m/s],  $\eta$  the dynamic viscosity of water ( $\eta_{water} = 0,001 \text{ Pa} \cdot \text{s}$ ) and  $\mathbf{p}$  the pressure [Pa]. In the computation, the body force per unit mass  $\mathbf{B}$  was set to be zero. In the 2D axisymmetric model a moving mesh based on the arbitrary Lagrangian-Eulerian (ALE) application mode was used. The ALE mode enabled the representation of a free surface boundary with a domain boundary on the moving mesh. To simulate the water droplet, the system was embedded in a simulation sphere of radius 1 mm. To solve the fluid motion equations, no-slip boundary conditions were applied (cp. Chapter: 2.3.1.3). The maximum velocity at  $\cos(\omega t) = 1$  was evaluated exactly at the same positions where the detector bead was placed experimentally.

The computed fluidic field (orange arrows) is shown together with the experimental results (black arrows) in Figure 4.2.6. Maximum experimental deviations of the nominal parameters of the bead radius ( $r = 0.90 \text{ } \mu\text{m}$ ) and source amplitude ( $A = 411 \text{ nm}$ ) provided variations of 2% in the simulated velocity fields. It should be mentioned that the velocity of two closely spaced beads is intrinsically different from single ones due to the influence of the flow field of one bead to the other. The optically trapped detector particle shows a resistivity to the flow which is therefore slightly disturbed. The source could experience this disturbance as an increased viscosity. To try to account for the effect of ignoring the detecting bead in the simulations, the source and the detector bead were tracked in the experiment at the same time, attenuating the previous effect by looking at the amplitude of the source at each data point and normalizing the FFT detector amplitudes.

The comparison between numerical simulations and the measured data (Figure A I) showed a good agreement of the field pattern around the oscillating microsource when the detecting particle was located along the dipole axis (at  $\theta \approx 0^\circ$ ), and at intermediate positions far from the source (at  $\theta < 90^\circ$ ). At these positions, the revealed velocity field pattern resembles that of a dipole-type source in an incompressible flow. On the other hand, the magnitude of the measured signal was slightly larger than the numerical results at all positions. The largest differences between theory and experiments were found at the nearest points to the source ( $\sim 5 \text{ } \mu\text{m}$ ), and at positions perpendicular to the dipole axis

---

(at  $\theta \approx 90^\circ$ ), where numerical results presented a strong signal parallel to the dipole axis but the experimental field pointed perpendicular to it. These differences could be attributed to the finite compressibility of water (acoustic wave) which is not included in the simulations. The addition of the velocity field of an acoustic dipole could compensate for the difference in magnitude and angles which are always smaller in the numerical simulations compared to the experiment. Taken together, the optimal agreement between theory and experiment clearly demonstrate the feasibility of our experimental multi-tweezers configuration for the detection of flow fields. Moreover, our simulations unraveled differences in the model when approaching small distances between source and detector, where maybe acoustic effects need to be taken into account to qualitatively and quantitatively determine the field contributions also in this distances form the source.



## Abbreviations

BLZ: blaze wavelength;

cat: chloramphenicol resistance;

CCW: Counter-clockwise;

comK: competence transcription factor of *B. subtilis*;

comS: releases comK for autostimulation;

CW: clockwise;

erm: erythromycin resistance;

FFT: Fast Fourier Transformation;

GLAD: Glancing angle deposition;

GLMT: Generalized Lorenz Mie theory;

hag: flagellin protein, ~20,000 subunits create one flagellum;

his leu met: histidine, leucine and methionine resistance respectively;

kan: kanamycin resistance;

MSD: Mean square displacement;

rok: repressor protein;

spc: spectinomycin resistance;



## Bibliography

- [1] A. Ashkin, Acceleration and trapping of particles by radiation pressure, *Physical review letters*, 24 (1970) 156-159.
- [2] A. Ashkin, J. Dziedzic, J. Bjorkholm and S. Chu, Observation of a single-beam gradient force optical trap for dielectric particles, *Optics letters*, 11 (1986) 288-290.
- [3] H. Misawa, M. Koshioka, K. Sasaki, N. Kitamura and H. Masuhara, Spatial pattern formation, size selection, and directional flow of polymer latex particles by laser trapping technique, *Chemistry Letters*, 20 (1991) 469-472.
- [4] K. Svoboda and S. M. Block, Biological applications of optical forces, *Annual review of biophysics and biomolecular structure*, 23 (1994) 247-285.
- [5] M. Friese, J. Enger, H. Rubinsztein-Dunlop and N. R. Heckenberg, Optical angular-momentum transfer to trapped absorbing particles, *Physical Review A*, 54 (1996) 1593.
- [6] J. Prikulis, F. Svedberg, M. Käll, J. Enger, K. Ramser, M. Goksör and D. Hanstorp, Optical spectroscopy of single trapped metal nanoparticles in solution, *Nano Lett.*, 4 (2004) 115-118.
- [7] P. M. Hansen, V. K. Bhatia, N. Harrit and L. Oddershede, Expanding the optical trapping range of gold nanoparticles, *Nano Lett.*, 5 (2005) 1937-1942.
- [8] A. Jonáš and P. Zemánek, Light at work: the use of optical forces for particle manipulation, sorting, and analysis, *Electrophoresis*, 29 (2008) 4813-4851.
- [9] S. Ito, H. Yoshikawa and H. Masuhara, Laser manipulation and fixation of single gold nanoparticles in solution at room temperature, *Applied physics letters*, 80 (2002) 482-484.
- [10] A. S. Urban, A. A. Lutich, F. D. Stefani and J. Feldmann, Laser printing single gold nanoparticles, *Nano Lett.*, 10 (2010) 4794-4798.
- [11] P. J. Pauzauskie, A. Radenovic, E. Trepagnier, H. Shroff, P. Yang and J. Liphardt, Optical trapping and integration of semiconductor nanowire assemblies in water, *Nature materials*, 5 (2006) 97-101.
- [12] R. Agarwal, K. Ladavac, Y. Roichman, G. Yu, C. Lieber and D. Grier, Manipulation and assembly of nanowires with holographic optical traps, *Optics Express*, 13 (2005) 8906-8912.
- [13] A. Ohlinger, A. Deak, A. A. Lutich and J. Feldmann, Optically trapped gold nanoparticle enables listening at the microscale, *Physical review letters*, 108 (2012) 018101.
- [14] Y. Tian, P. Navarro and M. Orrit, Single Molecule as a Local Acoustic Detector for Mechanical Oscillators, *Physical Review Letters*, 113 (2014) 135505.

- 
- [15] G. M. Whitesides, The origins and the future of microfluidics, *Nature*, 442 (2006) 368-373.
- [16] H. Craighead, Future lab-on-a-chip technologies for interrogating individual molecules, *Nature*, 442 (2006) 387-393.
- [17] A. Ashkin, *Optical Trapping and Manipulation of Neutral Particles Using Lasers*, World Scientific Publishing Co. Pte. Ltd., Singapore, 2006.
- [18] C. Liberale, P. Minzioni, F. Bragheri, F. De Angelis, E. Di Fabrizio and I. Cristiani, Miniaturized all-fibre probe for three-dimensional optical trapping and manipulation, *Nature photonics*, 1 (2007) 723-727.
- [19] A. Rohrbach and E. H. Stelzer, Optical trapping of dielectric particles in arbitrary fields, *JOSA A*, 18 (2001) 839-853.
- [20] N. Malagnino, G. Pesce, A. Sasso and E. Arimondo, Measurements of trapping efficiency and stiffness in optical tweezers, *Optics Communications*, 214 (2002) 15-24.
- [21] G. Gouesbet, Generalized lorenz-mie theory and applications, *Particle & particle systems characterization*, 11 (1994) 22-34.
- [22] D. R. H. Craig F. Bohren, *Absorption and Scattering of Light by Small Particles*, John Wiley & Sons, INC., 1998.
- [23] S. A. Maier, *Plasmonics: Fundamentals and Applications*, Springer Science+Business Media LLC, New York, 2007.
- [24] U. Kreibig and M. Vollmer, *Optical properties of metal clusters*, (1995).
- [25] S. A. Maier, *Plasmonics: Fundamentals and Applications: Fundamentals and Applications*, Springer, 2007.
- [26] P. B. Johnson and R.-W. Christy, Optical constants of the noble metals, *Physical Review B*, 6 (1972) 4370.
- [27] H. Kuwata, H. Tamaru, K. Esumi and K. Miyano, Resonant light scattering from metal nanoparticles: Practical analysis beyond Rayleigh approximation, *Applied Physics Letters*, 83 (2003) 4625-4627.
- [28] R. Kitamura, L. Pilon and M. Jonasz, Optical constants of silica glass from extreme ultraviolet to far infrared at near room temperature, *Applied optics*, 46 (2007) 8118-8133.
- [29] B. T. Draine and P. J. Flatau, Discrete-dipole approximation for scattering calculations, *JOSA A*, 11 (1994) 1491-1499.
- [30] C. Kittel, *Einführung in die Festkörperphysik*, Oldenbourg Verlag München Wien, 2005.
- [31] R. R. Agayan, F. Gittes, R. Kopelman and C. F. Schmidt, Optical trapping near resonance absorption, *Applied optics*, 41 (2002) 2318-2327.

- [32] R. Brown, The miscellaneous botanical works of Robert Brown, Ray society, 1866.
- [33] M. R. Reichl and D. Braun, Thermophoretic Manipulation of Molecules Inside Living Cells, *Journal of the American Chemical Society*, (2014).
- [34] M. Wolff, D. Braun and M. A. Nash, Detection of Thermoresponsive Polymer Phase Transition in Dilute Low-Volume Format by Microscale Thermophoretic Depletion, *Analytical chemistry*, (2014).
- [35] A.-K. Marel, M. Zorn, C. Klingner, R. Wedlich-Söldner, E. Frey and J. O. Rädler, Flow and Diffusion in Channel-Guided Cell Migration, *Biophysical journal*, 107 (2014) 1054-1064.
- [36] H. Engelke, I. Dorn and J. O. Rädler, Diffusion and molecular binding in crowded vesicle solutions measured by fluorescence correlation spectroscopy, *Soft Matter*, 5 (2009) 4283-4289.
- [37] L. Rusu, D. Lumma and J. O. Rädler, Charge and size dependence of liposome diffusion in semidilute biopolymer solutions, *Macromolecular bioscience*, 10 (2010) 1465-1472.
- [38] H. C. Berg, *Random Walks in Biology*, Princeton University Press, New Jersey, 1983.
- [39] A. Einstein, Über die von der molekularkinetischen Theorie der Wärme geforderte Bewegung von in ruhenden Flüssigkeiten suspendierten Teilchen, *Annalen der physik*, 322 (1905) 549-560.
- [40] B. Lukić, S. Jeney, C. Tischer, A. Kulik, L. Forró and E.-L. Florin, Direct observation of nondiffusive motion of a Brownian particle, *Physical review letters*, 95 (2005) 160601.
- [41] T. Fließbach, *Statistische Physik*, München, 2007.
- [42] B. Maier and J. O. Rädler, Conformation and self-diffusion of single DNA molecules confined to two dimensions, *Physical review letters*, 82 (1999) 1911.
- [43] A. Urban, M. Fedoruk, M. Horton, J. Radler, F. Stefani and J. Feldmann, Controlled nanometric phase transitions of phospholipid membranes by plasmonic heating of single gold nanoparticles, *Nano Lett.*, 9 (2009) 2903-2908.
- [44] C. Tischer, A. Pralle and E.-L. Florin, Determination and correction of position detection nonlinearity in single particle tracking and three-dimensional scanning probe microscopy, *Microscopy and Microanalysis*, 10 (2004) 425-434.
- [45] F. G. a. C. F. Schmidt, *Methods in Cell Biology*; Chapter 8: Signals and Noise in Micromechanical Measurements, Academic Press, 1998.
- [46] F. Gittes and C. F. Schmidt, Thermal noise limitations on micromechanical experiments, *European biophysics journal*, 27 (1998) 75-81.
- [47] B. S. Schmidt, A. H. Yang, D. Erickson and M. Lipson, Optofluidic trapping and transport on solid core waveguides within a microfluidic device, *Optics Express*, 15 (2007) 14322-14334.

- 
- [48] G. Boer, R. Johann, J. Rohner, F. Merenda, G. Delacrétaz, P. Renaud and R.-P. Salathé, Combining multiple optical trapping with microflow manipulation for the rapid bioanalytics on microparticles in a chip, *Review of Scientific Instruments*, 78 (2007) 116101-116101-116103.
- [49] P. D. M. a. L. Crane, *Physical Fluid Dynamics*, Academic Press, London.
- [50] J. Friend and L. Y. Yeo, Microscale acoustofluidics: Microfluidics driven via acoustics and ultrasonics, *Reviews of Modern Physics*, 83 (2011) 647.
- [51] H. B. John Happel, Low Reynolds number hydrodynamics, in, *Martinus Nijhoff Publishers*, 1983.
- [52] O. Reynolds, An experimental investigation of the circumstances which determine whether the motion of water shall be direct or sinuous, and of the law of resistance in parallel channels, *Proceedings of the royal society of London*, 35 (1883) 84-99.
- [53] O. Reynolds, On the Sub-Mechanics of the Universe, *Proceedings of the Royal Society of London*, 69 (1901) 425-433.
- [54] E. M. Purcell, Life at low Reynolds number, in: *AIP Conference Proceedings*, 1976, pp. 49.
- [55] N. Darnton, L. Turner, K. Breuer and H. C. Berg, Moving fluid with bacterial carpets, *Biophysical Journal*, 86 (2004) 1863-1870.
- [56] G. Taylor, Analysis of the swimming of microscopic organisms, *Proceedings of the Royal Society of London. Series A. Mathematical and Physical Sciences*, 209 (1951) 447-461.
- [57] N. Uchida and R. Golestanian, Synchronization and collective dynamics in a carpet of microfluidic rotors, *Physical review letters*, 104 (2010) 178103.
- [58] H. C. Berg, Bacterial behaviour, *Nature*, 254 (1975) 389-392.
- [59] E. Lauga and T. R. Powers, The hydrodynamics of swimming microorganisms, *Reports on Progress in Physics*, 72 (2009) 096601.
- [60] N. Cohen and J. H. Boyle, Swimming at low Reynolds number: a beginners guide to undulatory locomotion, *Contemporary Physics*, 51 (2010) 103-123.
- [61] H. Stark, Immer in Bewegung bleiben, *Physik Journal*, 6 (2007) 31.
- [62] C. G. Ehrenberg, C. G. Ehrenberg, N. Microbiologist, C. G. Ehrenberg and N. Microbiologiste, *Die Infusionsthierchen als vollkommene Organismen: ein Blick in das tiefere organische Leben der Natur*, Verlag von Leopold Voss, 1838.
- [63] K. B. Reichert, Über die Sichtbarmachung der Geisseln und die Geisselbewegung der Bakterien, in, 1909.
- [64] R. M. Macnab, Examination of bacterial flagellation by dark-field microscopy, *Journal of clinical microbiology*, 4 (1976) 258-265.
- [65] L. Turner, W. S. Ryu and H. C. Berg, Real-time imaging of fluorescent flagellar filaments, *Journal of Bacteriology*, 182 (2000) 2793-2801.

- [66] T. L. Min, P. J. Mears, L. M. Chubiz, C. V. Rao, I. Golding and Y. R. Chemla, High-resolution, long-term characterization of bacterial motility using optical tweezers, *Nature methods*, 6 (2009) 831-835.
- [67] A. Ashkin, J. Dziedzic and T. Yamane, Optical trapping and manipulation of single cells using infrared laser beams, *Nature*, 330 (1987) 769-771.
- [68] H. C. Berg, The rotary motor of bacterial flagella, *Biochemistry*, 72 (2003) 19.
- [69] H. C. Berg and R. A. Anderson, Bacteria swim by rotating their flagellar filaments, (1973).
- [70] R. M. Macnab, How bacteria assemble flagella, *Annual Reviews in Microbiology*, 57 (2003) 77-100.
- [71] R. M. Macnab, Genetics and biogenesis of bacterial flagella, *Annual review of genetics*, 26 (1992) 131-158.
- [72] R. M. Macnab, Bacterial flagella rotating in bundles: a study in helical geometry, *Proceedings of the National Academy of Sciences*, 74 (1977) 221-225.
- [73] J. Shioi, S. Matsuura and Y. Imae, Quantitative measurements of proton motive force and motility in *Bacillus subtilis*, *Journal of bacteriology*, 144 (1980) 891-897.
- [74] R. M. Macnab, The bacterial flagellum: reversible rotary propellor and type III export apparatus, *Journal of bacteriology*, 181 (1999) 7149-7153.
- [75] S. D. Reid, R. K. Selander and T. S. Whittam, Sequence diversity of flagellin (fliC) alleles in pathogenic *Escherichia coli*, *Journal of bacteriology*, 181 (1999) 153-160.
- [76] M. D. Manson, Dynamic motors for bacterial flagella, *Proceedings of the National Academy of Sciences*, 107 (2010) 11151-11152.
- [77] H. C. Berg, Torque generation by the flagellar rotary motor, *Biophysical journal*, 68 (1995) 163S.
- [78] N. C. Darnton, L. Turner, S. Rojevsky and H. C. Berg, On torque and tumbling in swimming *Escherichia coli*, *Journal of bacteriology*, 189 (2007) 1756-1764.
- [79] M. Kim, J. C. Bird, A. J. Van Parys, K. S. Breuer and T. R. Powers, A macroscopic scale model of bacterial flagellar bundling, *Proceedings of the National Academy of Sciences*, 100 (2003) 15481-15485.
- [80] M. J. Kim, M. J. Kim, J. C. Bird, J. Park, T. R. Powers and K. S. Breuer, Particle image velocimetry experiments on a macro-scale model for bacterial flagellar bundling, *Experiments in fluids*, 37 (2004) 782-788.
- [81] N. Uchida and R. Golestanian, Generic conditions for hydrodynamic synchronization, *Physical Review Letters*, 106 (2011) 058104.
- [82] T. R. Powers, Role of body rotation in bacterial flagellar bundling, *Physical Review E*, 65 (2002) 040903.

- 
- [83] M. Reichert and H. Stark, Synchronization of rotating helices by hydrodynamic interactions, *The European Physical Journal E*, 17 (2005) 493-500.
- [84] L. Turner, R. Zhang, N. C. Darnton and H. C. Berg, Visualization of flagella during bacterial swarming, *Journal of bacteriology*, 192 (2010) 3259-3267.
- [85] R. M. Macnab and D. Koshland, The gradient-sensing mechanism in bacterial chemotaxis, *Proceedings of the National Academy of Sciences*, 69 (1972) 2509-2512.
- [86] D. L. Englert, M. D. Manson and A. Jayaraman, Investigation of bacterial chemotaxis in flow-based microfluidic devices, *Nature protocols*, 5 (2010) 864-872.
- [87] T. Klar, M. Perner, S. Grosse, G. Von Plessen, W. Spirkel and J. Feldmann, Surface-plasmon resonances in single metallic nanoparticles, *Physical Review Letters*, 80 (1998) 4249.
- [88] C. Sönnichsen, T. Franzl, T. Wilk, G. von Plessen, J. Feldmann, O. Wilson and P. Mulvaney, Drastic reduction of plasmon damping in gold nanorods, *Physical Review Letters*, 88 (2002) 077402.
- [89] L. Osinkina, S. Carretero-Palacios, J. Stehr, A. A. Lutich, F. Jäckel and J. Feldmann, Tuning DNA binding kinetics in an optical trap by plasmonic nanoparticle heating, *Nano Lett.*, 13 (2013) 3140-3144.
- [90] A. Ohlinger, S. Nedev, A. A. Lutich and J. Feldmann, Optothermal escape of plasmonically coupled silver nanoparticles from a three-dimensional optical trap, *Nano Lett.*, 11 (2011) 1770-1774.
- [91] M. Leisner, K. Stingl, J. O. Radler and B. Maier, Basal expression rate of comK sets a 'switching-window' into the K-state of *Bacillus subtilis*, *Molecular Microbiology*, 63 (2007) 1806-1816.
- [92] T. T. Hoa, P. Tortosa, M. Albano and D. Dubnau, Rok (YkuW) regulates genetic competence in *Bacillus subtilis* by directly repressing comK, *Molecular microbiology*, 43 (2002) 15-26.
- [93] K. Turgay, J. Hahn, J. Burghoorn and D. Dubnau, Competence in *Bacillus subtilis* is controlled by regulated proteolysis of a transcription factor, *The EMBO journal*, 17 (1998) 6730-6738.
- [94] T. McKenzie, T. Hoshino, T. Tanaka and N. Sueoka, The nucleotide sequence of pUB110: some salient features in relation to replication and its regulation, *Plasmid*, 15 (1986) 93-103.
- [95] H. Maamar and D. Dubnau, Bistability in the *Bacillus subtilis* K-state (competence) system requires a positive feedback loop, *Molecular microbiology*, 56 (2005) 615-624.
- [96] G. W. Ordal, Calcium ion regulates chemotactic behaviour in bacteria, *Nature*, 270 (1977) 66-67.



- [97] G. W. Ordal and D. J. Goldman, Chemotaxis away from uncouplers of oxidative-phosphorylation in bacillus-subtilis, *Science*, 189 (1975) 802-805.
- [98] F. Hoffman, An introduction to Fourier theory, *Extra* 2 (2004).
- [99] B. Lathi, Linear systems and signals, ISBN13, 554625343 (2006).
- [100] J. W. Cooley and J. W. Tukey, An algorithm for the machine calculation of complex Fourier series, *Math. comput*, 19 (1965) 297-301.
- [101] S. Block, K. Fahrner and H. Berg, Visualization of bacterial flagella by video-enhanced light microscopy, *Journal of bacteriology*, 173 (1991) 933-936.
- [102] Y. Sowa, B. C. Steel and R. M. Berry, A simple backscattering microscope for fast tracking of biological molecules, *Review of Scientific Instruments*, 81 (2010) 113704-113704-113706.
- [103] K. Svoboda and S. M. Block, Optical trapping of metallic Rayleigh particles, *Optics letters*, 19 (1994) 930-932.
- [104] S. R. Kirchner, M. Fedoruk, T. Lohmüller and J. Feldmann, Analyzing the Movement of the Nauplius' *Artemia salina*' by Optical Tracking of Plasmonic Nanoparticles, *JoVE (Journal of Visualized Experiments)*, (2014) e51502-e51502.
- [105] A. Urban, M. Fedoruk, S. Nedev, A. Lutich, T. Lohmueller and J. Feldmann, Shrink-to-fit Plasmonic Nanostructures, *Advanced Optical Materials*, (2013).
- [106] A. S. Urban, S. Carretero-Palacios, A. A. Lutich, T. Lohmüller, J. Feldmann and F. Jäckel, Optical trapping and manipulation of plasmonic nanoparticles: fundamentals, applications, and perspectives, *Nanoscale*, 6 (2014) 4458-4474.
- [107] C. M. A. Borg, E. Bruno and T. Kiørboe, The kinematics of swimming and relocation jumps in copepod nauplii, *PLoS one*, 7 (2012) e47486.
- [108] P. Croghan, The mechanism of osmotic regulation in *Artemia salina* (L.): the physiology of the branchiae, *Journal of Experimental Biology*, 35 (1958) 234-242.
- [109] B. M. Gilchrist, Growth and form of the brine shrimp *Artemia salina* (L.), in: *Proceedings of the zoological society of London*, Wiley Online Library, 1960, pp. 221-235.
- [110] E. Boone and L. Baas-Becking, Salt effects on eggs and nauplii of *Artemia salina* L, *The Journal of General Physiology*, 14 (1931) 753-763.
- [111] Z. Ferdous and A. Muktedir, A review: potentiality of zooplankton as bioindicator, *American journal of applied sciences*, 6 (2009) 1815.
- [112] G. A. Boxshall and D. Defaye, Global diversity of copepods (Crustacea: Copepoda) in freshwater, *Hydrobiologia*, 595 (2008) 195-207.
- [113] J. A. Lock and G. Gouesbet, Generalized Lorenz-Mie theory and applications, *Journal of Quantitative Spectroscopy and Radiative Transfer*, 110 (2009) 800-807.

- 
- [114] G. Gouesbet, B. Maheu and G. Gréhan, Light scattering from a sphere arbitrarily located in a Gaussian beam, using a Bromwich formulation, *JOSA A*, 5 (1988) 1427-1443.
- [115] G. Gouesbet, G. Gréhan and B. Maheu, Expressions to compute the coefficients  $g_{mn}$  in the generalized Lorenz-Mie theory using finite series, *Journal of optics*, 19 (1988) 35.
- [116] J. A. Lock, Calculation of the radiation trapping force for laser tweezers by use of generalized Lorenz-Mie theory. I. Localized model description of an on-axis tightly focused laser beam with spherical aberration, *Applied optics*, 43 (2004) 2532-2544.
- [117] J. A. Lock, Calculation of the radiation trapping force for laser tweezers by use of generalized Lorenz-Mie theory. II. On-axis trapping force, *Applied optics*, 43 (2004) 2545-2554.
- [118] J. A. Lock and S. Y. Wrbanek, Scattering of a tightly focused beam by an optically trapped particle, *Applied optics*, 45 (2006) 3634-3645.
- [119] T. A. Nieminen, N. du Preez-Wilkinson, A. B. Stilgoe, V. L. Loke, A. A. Bui and H. Rubinsztein-Dunlop, Optical tweezers: Theory and modelling, *Journal of Quantitative Spectroscopy and Radiative Transfer*, (2014).
- [120] T. A. Nieminen, V. L. Loke, A. B. Stilgoe, G. Knöner, A. M. Brańczyk, N. R. Heckenberg and H. Rubinsztein-Dunlop, Optical tweezers computational toolbox, *Journal of Optics A: Pure and Applied Optics*, 9 (2007) S196.
- [121] B. Maheu, G. Gouesbet and G. Gréhan, A concise presentation of the generalized Lorenz-Mie theory for arbitrary location of the scatterer in an arbitrary incident profile, *Journal of optics*, 19 (1988) 59.
- [122] S. Nedev, S. Carretero-Palacios, S. Kirchner, F. Jäckel and J. Feldmann, Microscale mapping of oscillatory flows, *Applied Physics Letters*, 105 (2014) 161113.
- [123] A. I. Bishop, T. A. Nieminen, N. R. Heckenberg and H. Rubinsztein-Dunlop, Optical microrheology using rotating laser-trapped particles, *Physical Review Letters*, 92 (2004) 198104.
- [124] I. M. Tolić-Nørrelykke, K. Berg-Sørensen and H. Flyvbjerg, MatLab program for precision calibration of optical tweezers, *Computer physics communications*, 159 (2004) 225-240.
- [125] K. C. Vermeulen, G. J. Wuite, G. J. Stienen and C. F. Schmidt, Optical trap stiffness in the presence and absence of spherical aberrations, *Applied optics*, 45 (2006) 1812-1819.
- [126] P. Fischer and A. Ghosh, Magnetically actuated propulsion at low Reynolds numbers: towards nanoscale control, *Nanoscale*, 3 (2011) 557-563.
- [127] S. J. Ebbens and J. R. Howse, In pursuit of propulsion at the nanoscale, *Soft Matter*, 6 (2010) 726-738.

- [128] A. Ghosh and P. Fischer, Controlled propulsion of artificial magnetic nanostructured propellers, *Nano Lett.*, 9 (2009) 2243-2245.
- [129] S. Tottori, L. Zhang, F. Qiu, K. K. Krawczyk, A. Franco-Obregón and B. J. Nelson, Magnetic helical micromachines: fabrication, controlled swimming, and cargo transport, *Advanced materials*, 24 (2012) 811-816.
- [130] W. Gao, S. Sattayasamitsathit, K. M. Manesh, D. Weihs and J. Wang, Magnetically powered flexible metal nanowire motors, *Journal of the American Chemical Society*, 132 (2010) 14403-14405.
- [131] P. Tierno, R. Golestanian, I. Pagonabarraga and F. Sagués, Controlled swimming in confined fluids of magnetically actuated colloidal rotors, *Physical review letters*, 101 (2008) 218304.
- [132] A. Ghosh, D. Paria, H. J. Singh, P. L. Venugopalan and A. Ghosh, Dynamical configurations and bistability of helical nanostructures under external torque, *Physical Review E*, 86 (2012) 031401.
- [133] L. Zhang, T. Petit, Y. Lu, B. E. Kratochvil, K. E. Peyer, R. Pei, J. Lou and B. J. Nelson, Controlled propulsion and cargo transport of rotating nickel nanowires near a patterned solid surface, *ACS nano*, 4 (2010) 6228-6234.
- [134] L. Zhang, J. J. Abbott, L. Dong, K. E. Peyer, B. E. Kratochvil, H. Zhang, C. Bergeles and B. J. Nelson, Characterizing the swimming properties of artificial bacterial flagella, *Nano Lett.*, 9 (2009) 3663-3667.
- [135] L. Paterson, M. MacDonald, J. Arlt, W. Sibbett, P. Bryant and K. Dholakia, Controlled rotation of optically trapped microscopic particles, *Science*, 292 (2001) 912-914.
- [136] S. Franke-Arnold, L. Allen and M. Padgett, Advances in optical angular momentum, *Laser & Photonics Reviews*, 2 (2008) 299-313.
- [137] S. J. Parkin, G. Knöner, T. A. Nieminen, N. R. Heckenberg and H. Rubinsztein-Dunlop, Picoliter viscometry using optically rotated particles, *Physical Review E*, 76 (2007) 041507.
- [138] A. I. Bishop, T. A. Nieminen, N. R. Heckenberg and H. Rubinsztein-Dunlop, Optical microrheology using rotating laser-trapped particles, *arXiv preprint physics/0402021*, (2004).
- [139] L. Tong, V. D. Miljkovic and M. Käll, Alignment, rotation, and spinning of single plasmonic nanoparticles and nanowires using polarization dependent optical forces, *Nano Lett.*, 10 (2009) 268-273.
- [140] J. Do, M. Fedoruk, F. Jäckel and J. Feldmann, Two-color laser printing of individual gold nanorods, *Nano Lett.*, 13 (2013) 4164-4168.
- [141] R. C. Gauthier, Ray optics model and numerical computations for the radiation pressure micromotor, *Applied physics letters*, 67 (1995) 2269-2271.
- [142] P. Galajda and P. Ormos, Complex micromachines produced and driven by light, *Applied Physics Letters*, 78 (2001) 249-251.

- 
- [143] G. Knöner, S. Parkin, N. R. Heckenberg and H. Rubinsztein-Dunlop, Characterization of optically driven fluid stress fields with optical tweezers, *Physical Review E*, 72 (2005) 031507.
- [144] E. Hecht, *Optik*, Oldenbourg Wissenschaftsverlag GmbH, München, 2001.
- [145] H. Mushfique, J. Leach, R. Di Leonardo, M. Padgett and J. Cooper, Optically driven pumps and flow sensors for microfluidic systems, *Proceedings of the Institution of Mechanical Engineers, Part C: Journal of Mechanical Engineering Science*, 222 (2008) 829-837.
- [146] M. Kim and T. R. Powers, Hydrodynamic interactions between rotating helices, *Physical review E*, 69 (2004) 061910.
- [147] A. Ashkin and J. Dziedzic, Optical trapping and manipulation of viruses and bacteria, *Science*, 235 (1987) 1517-1520.
- [148] S. M. Block, D. F. Blair and H. C. Berg, Compliance of bacterial flagella measured with optical tweezers, (1989).
- [149] M. Ericsson, D. Hanstorp, P. Hagberg, J. Enger and T. Nyström, Sorting out bacterial viability with optical tweezers, *Journal of bacteriology*, 182 (2000) 5551-5555.
- [150] S. Chattopadhyay, R. Moldovan, C. Yeung and X. Wu, Swimming efficiency of bacterium *Escherichiacoli*, *Proceedings of the National Academy of Sciences*, 103 (2006) 13712-13717.
- [151] S. R. Kirchner, S. Nedev, S. Carretero-Palacios, A. Mader, M. Opitz, T. Lohmüller and J. Feldmann, Direct optical monitoring of flow generated by bacterial flagellar rotation, *Applied Physics Letters*, 104 (2014) 093701.
- [152] G. E. Uhlenbeck and L. S. Ornstein, On the theory of the Brownian motion, *Physical review*, 36 (1930) 823.
- [153] M. C. Wang and G. E. Uhlenbeck, On the theory of the Brownian motion II, *Reviews of Modern Physics*, 17 (1945) 323-342.
- [154] D. B. Kearns and R. Losick, Swarming motility in undomesticated *Bacillus subtilis*, *Molecular microbiology*, 49 (2003) 581-590.
- [155] D. S. Bischoff, R. B. Bourret, M. L. Kirsch and G. W. Ordal, Purification and characterization of *Bacillus subtilis* CheY, *Biochemistry*, 32 (1993) 9256-9261.
- [156] K. C. Neuman, E. H. Chadd, G. F. Liou, K. Bergman and S. M. Block, Characterization of Photodamage to *Escherichia coli* in Optical Traps, *Biophysical Journal*, 77 (1999) 2856-2863.
- [157] U. Mirsaidov, W. Timp, K. Timp, M. Mir, P. Matsudaira and G. Timp, Optimal optical trap for bacterial viability, *Physical Review E*, 78 (2008) 021910.

- 
- [158] M. B. Rasmussen, L. B. Oddershede and H. Siegumfeldt, Optical tweezers cause physiological damage to *Escherichia coli* and *Listeria* bacteria, *Applied and environmental microbiology*, 74 (2008) 2441-2446.
- [159] E. M. Purcell, The efficiency of propulsion by a rotating flagellum, *Proceedings of the National Academy of Sciences*, 94 (1997) 11307-11311.
- [160] H. Flores, E. Lobaton, S. Méndez-Diez, S. Tlupova and R. Cortez, A study of bacterial flagellar bundling, *Bulletin of mathematical biology*, 67 (2005) 137-168.
- [161] E. R. Dufresne and D. G. Grier, Optical tweezer arrays and optical substrates created with diffractive optics, *Review of scientific instruments*, 69 (1998) 1974-1977.
- [162] S. Nedev, A. S. Urban, A. A. Lutich and J. Feldmann, Optical Force Stamping Lithography, *Nano Lett.*, 11 (2011) 5066-5070.
- [163] P. M. Morse, P. M. Morse and P. M. Morse, *Vibration and sound*, McGraw-Hill New York, 1948.
- [164] G. G. Harris and W. A. van Bergeijk, Evidence that the Lateral-Line Organ Responds to Near-Field Displacements of Sound Sources in Water, *The Journal of the Acoustical Society of America*, 34 (1962) 1831.



## Acknowledgements

The time at the Chair for Photonics and Optoelectronics has been wonderful in a scientific and personal way. I would like to thank everyone who contributed to it and I am very grateful for your advice, help and friendship.

I am especially appreciative for the support and guidance by my doctoral thesis supervisor **Prof. Dr. Jochen Feldmann**. I am very thankful that I was allowed to conduct my research at such an excellent chair. His chair combines high-level physics with physical diversity. I have greatly benefited from the highly productive discussions we had and I owe him enormous gratitude for helping me to become an independent scientist. His support was not only related to disciplinary topics. He gave me the chance to present my work at many different conferences and enabled a fantastic research stay at the California NanoSystems Institute, University of California Los Angeles. The time at his chair helped me significantly not only for my scientific but also personal development.

I would like to thank **Prof. Dr. Joachim Rädler** for the opportunity to collaborate on very interesting and interdisciplinary topics. I benefited from productive discussions and advice that led to the realization of great projects.

Many, many thanks to my advisor **Dr. Theobald Lohmüller** for the excellent support I received during my time here. His enthusiasm for new experiments, his creativity and knowledge of diverse scientific fields all helped me a lot to conduct my research. I owe him special thanks for his highly professional editing of manuscripts and application forms. Thank you, Theo!

I am thankful to **Dr. Andrey Lutich** who guided me during my first stages of my work here and helped me significantly to gain my skills in microscopy and biophysics.

**Dr. Sol Carretero-Palacios** and **Spas Nedev** have a special place in this work for their great support during my time here.

**Dr. Madeleine Opitz** and **Andreas Mader** are gratefully acknowledged for their excellent experimental and theoretical support on biological microsystems.

I am thankful to **Prof. Dr. Peer Fischer** and **Debora Schamel** for great discussions and the preparation of diverse microhelical objects.

Express thanks go to **Dr. Ilka Kriegel, Dr. Lindsey Anderson, Dr. Michael Fedoruk, Carla Zensen, Felix Winterer, Patrick Urban** for their marvelous help on my experimental and written work.

**Dr. Ilka Kriegel** deserves special thanks for being a unique friend to me.

Thanks to my great roommates **Verena Hintermayr** and **Patrick Urban**. I will miss the pleasant atmosphere in our office a lot and I wish you all the best for your future.

I am very grateful for the support during my time at the chair to **Dr. Aleksander Vaneski, Dr. Maximilian Berr, Dr. Alexander Urban, Dr. Cordula Urban, Dr. Christian Mauser, Dr. Jaekwon Do, Spas Nedev, Paul Kühler, Lidiya Osinkina, Dr. Calin Herlescu, Dr. Raphael Tautz, Dr. Alexander Ohlinger** and **Franziska Kriegel**.

I would like to thank **Gerlinde Adam** for her enormous warm-heartedness which made a sunny day a little sunnier and even helped me through hungry days.

**Stefan Niedermaier** and **Christian Holopirek** always helped me with technical questions with their high expertise in designing and realization of many diverse devices.

The greatest *thank you* of all deserves my family. I am especially grateful for the endless support and believe in me to **Anita Pritschkat-Kirchner, Wolfgang Kirchner, Rita Kirchner** and **Marie Langer**. Without you, this thesis would not have been possible. I will always be very thankful to **Hermann Pritschkat**.

Finally, I want to thank **Markus Kirchner**. I wish you all the best - as you deserve it.



# Curriculum Vitae

## EDUCATION

**Chair for Photonics and Optoelectronics, Prof. Dr. Jochen Feldmann,  
Physics Department,  
Ludwig-Maximilians-Universität, Munich,  
Germany**

PhD student, research projects:

- Monitoring bacteria activity with optically trapped microparticles;
- Optical sensing and driving of helical microbiological objects;
- Investigation of thermosensitive transmembrane proteins by optothermal manipulation with plasmonically heated gold nanoparticles;
- Raman spectroscopy on lipid membranes;

since November 2010

Science degree/Diploma in physics, Title of diploma thesis:

“Microfluidic generation of phospholipid vesicles and their optical investigation”

August 2010

**Nikolaus-Kopernikus-Gymnasium,  
Weißenhorn,  
Germany**

Abitur, June 2003

---

## TALKS AND CONTRIBUTIONS TO CONFERENCES

Talk “Concepts for sensing and driving helical microbiological objects” at the *Workshop on Photonics and Optoelectronics*, Hirschegg-Kleinwalsertal, Austria, September/October 2014

Talk “Novel nano-optical concepts for sensing and driving helical microbiological objects” at the *SPIE Optics + Photonics symposium 2014*, Convention Center San Diego, United States, August 2014

Poster presentation at the *NIM<sup>17</sup> Workshop: “Young Ideas in Nanoscience”*, München, Germany, November 2013 (honored with a **Poster Award**)

Invited Talk “Research at LMU on Raman Spectroscopy, Optothermal Manipulation and Optical Tweezers” at the *Chair for Chemistry and Biochemistry*, Prof. Paul Weiss, California NanoSystems Institute, University of California Los Angeles, America, October 2013

Invited talk “Monitoring Bacteria Activity with Optically Trapped Microparticles” at the *Chair for Experimental Physics: Soft Matter Physics and Biophysics*, Prof. Dr. Joachim Rädler, Ludwig-Maximilians-Universität München, Germany, April 2013

Poster presentation at the *NIM/iNano Winterschool 2013*, Kirchberg (Tyrol), Austria, March 2013 (honored with a **Poster Award**)

Poster presentation at the *NIM-Graduate Program Summer Retreat 2012*, Garmisch-Partenkirchen, Germany, June 2012

Poster presentation at the *Seoul NanoHealth 2011, 5<sup>th</sup> Annual Symposium on Nanobiotechnology*, Seoul, South Korea, November 2011

Participant of the *42nd IFF Spring School 2011, Macromolecular Systems in Soft and Living Matter*, Jülich, Germany, February 2011

Talk “Diffusion in a lipid bilayer” at the workshop *From Biophotonics to Optoelectronics*, Riezlern, Austria, September 2011

Poster presentation at the *Sonder-Forschungs-Bereich 449 International Meeting, From Protein Structure to Membrane Dynamics*, Berlin, Germany, December 2010

Talk “Microfluidic generation of phospholipid vesicles” at the *Deutsche Physikalische Gesellschaft Frühjahrstagung*, Regensburg, Germany, March 2010

---

<sup>17</sup> NIM: Nanosystems Initiative Munich;

PUBLICATIONS AND AWARDS

S. R. Kirchner et al., Membrane composition of jetted lipid vesicles: a Raman spectroscopy study. *J. Biophotonics* **5**, No. 1, 40-46 (2012).

S. R. Kirchner, S. Nedev, S. Carretero-Palacios, A. Mader, M. Opitz, T. Lohmüller, and J. Feldmann, Direct optical monitoring of flow generated by bacterial flagellar rotation. *Appl. Phys. Lett.* **104**, 093701 (2014).

S. R. Kirchner, M. Fedoruk, T. Lohmüller, and J. Feldmann, Analyzing the Movement of the Nauplius 'Artemia salina' by Optical Tracking of Plasmonic Nanoparticles. *J. Vis. Exp.* **89**, e51502 (2014).

S. Nedev, S. Carretero-Palacios, S. R. Kirchner, F. Jäckel and J. Feldmann, Microscale mapping of oscillatory flows. *Appl. Phys. Lett.* **105**, 161113 (2014).

S. R. Kirchner, L. J. Anderson, D. Schamel, C. Zensen, P. Fischer, T. Lohmüller, and J. Feldmann, Focused optical beams for Microfluidic Characterization of Chiral Microobjects, in preparation.

P. Urban, S. R. Kirchner, T. Lohmüller and J. Feldmann, Switching membrane permeability by plasmonic heating of gold nanoparticles, in preparation.

**Awards:**

**Erwin Schrödinger Society Poster Award**, *BioNanoMed* 2014, Erwin Schrödinger Society for Nanosciences, Poster title: Monitoring of flagellar rotation of bacterial cells with optical tweezers.

**NIM<sup>18</sup> Poster Award 2013**, Poster title: Ultrasensitive Detection of Bacteria Mobility with Optical Tweezers.

**Award for best Poster**, *NIM workshop "Young Ideas in Nanoscience"* 2013, Poster title: Ultrasensitive Detection of Bacteria Mobility with Optical Tweezers.

---

<sup>18</sup> NIM: Nanosystems Initiative Munich;

---

## FURTHER QUALIFICATIONS

Programming: C/C++, Comsol, Mathematica

Applications: MS Office (Excel, Word, Power Point), Adobe Photoshop,  
Adobe Illustrator, Corel Draw

Languages: German (mother tongue), English (fluently), French, Latin

## PROFESSIONAL AND VOLUNTEER ORGANIZATIONS

Poster exposition at the *NIM<sup>19</sup> NanoDay*, Deutsches Museum (Zentrum für Neue Technologien), Munich, Germany, November 2014

Organizer of the *Workshop on Photonics and Optoelectronics*, Hirschegg-Kleinwalsertal, Austria, September/October 2014

Visiting Scholar at the *Chair for Chemistry and Biochemistry*, Prof. Paul Weiss, California NanoSystems Institute, University of California Los Angeles, United States, August 2013 – November 2013

Supervision of Master thesis entitled: Control of ionic flows through membranes by optothermal manipulation, November 2012 - October 2013

Student board member of the excellence cluster *NIM*, March 2012 - February 2013

Poster exposition at the *NIM NanoDay*, Deutsches Museum (Zentrum für Neue Technologien), Munich, Germany, September 2012

Member of the NIM Mentoring Program (e.g. Girls Day, April 2013)

---

<sup>19</sup> NIM: Nanosystems Initiative Munich;